Summer 2004

Dynamical Studies of Model Membrane and Cellular Response to Nanosecond, High-Intensity Pulsed Electric Fields

Qin Hu
Old Dominion University

Dynamical Studies of Model Membrane and Cellular Response to Nanosecond, High-intensity Pulsed Electric Fields

by

Qin Hu

B. S. University of Electronic Science & Technology of China (UESTC)
M. S. University of Electronic Science & Technology of China (UESTC)

A Dissertation Submitted to the Faculty of
Old Dominion University in Partial Fulfillment of the
Requirement for the Degree of

DOCTOR OF PHILOSOPHY

ELECTRICAL ENGINEERING

OLD DOMINION UNIVERSITY

August 2004

Approved by:

Ravindra P. Joshi (Director)

Stephen J. Beebe (Member)

Linda L. Vahala (Member)

Karl H. Schoenbach (Member)

Stephen A. Zahorian (Member)

ABSTRACT

DYNAMICAL STUDIES OF MODEL MEMBRANE AND CELLULAR RESPONSE TO NANOSECOND, HIGH-INTENSITY PULSED ELECTRIC FIELDS

Qin Hu
Old Dominion University, 2004
Director: Dr. Ravindra P. Joshi

The dynamics of electroporation of biological cells subjected to nanosecond, high intensity pulses are studied based on a coupled scheme involving the current continuity and Smoluchowski equations. The improved pore formation energy model includes a dependence on pore population and density. It also allows for variable surface tension and incorporates the effects of finite conductivity on the electrostatic correction term, which was not considered by the simple energy models in the literature. It is shown that E(r) becomes self-adjusting with variations in its magnitude and profile. The whole scheme is self-consistent and dynamic.

An electromechanical analysis based on thin-shell theory is presented to analyze cell shape changes in response to external electric fields. The calculations demonstrate that at large fields, the spherical cell geometry can be modified, and even ellipsoidal forms may not be appropriate to account for the resulting shape. It is shown that, in keeping with reports in the literature, the final shape depends on membrane thickness. This has direct implications for tissues in which significant molecular restructuring can occur.

This study is also focused on obtaining qualitative predictions of pulse width dependence to apoptotic cell irreversibility that has been observed experimentally. The analysis couples a distributed electrical model for current flow with the Smoluchowski equation to provide self-consistent, time-dependent transmembrane voltages. The model

captures the essence of the experimentally observed pulse-width dependence, and provides a possible physical picture that depends only on the electrical trigger. Different cell responses of normal and malignant (Farage) tonsillar B-cell are also compared and discussed. It is shown that subjecting a cell to an ultrashort, high-intensity electric pulse is the optimum way for reversible intracellular manipulation.

Finally, a simple but physical atomistic model is presented for molecular motion within biological membranes subjected to electric fields. The dynamical, stochastic aspects are treated at the molecular level, without including each and every atom of the complex molecular system. The membrane lipid molecules are represented by a ball-spring model, with pair-wise Lennard-Jones interacting potentials. Predictions include pore formation times of around 1 ns, relatively low ionic throughput in keeping with recent observations, and currents of about 5 nA (at 500 kV/cm). It is also shown that ions facilitate pore formation and that membrane poration may be the principle route for phosphatidylserine externalization.

ACKNOWLEDGMENTS

I am immensely grateful to my advisor, Dr. R. P. Joshi, for his valuable academic guidance and encouragement throughout the course of this study. His insight and wisdom greatly inspired me. To a great extent, my work ethic has been shaped by his professionalism, which has been an invaluable example to me. I would also like to thank my research committee members, Dr. Linda L. Vahala, Stephen J. Beebe and Stephen A. Zahorian for their review and valuable comments.

Great thanks to Dr. Karl Schoenbach at the Center for Bioelectronics for his concern and ever-available support, which made it possible to finish the dissertation.

I am indebted to my parents and would like to thank them for their courage and supports.

Special thank goes to my husband, Fansheng Meng for his understanding and valuable supports when I stayed glued to my computer.

Special thank also goes to my friends: Shangping Guo, Jun Qian and Feng Wu. Their intelligence always lights me up.

To my dear parents, Ma Daiyu and Hu Daocheng

my lovely daughter, Jennifer (Xiaojing)

and my dear husband Fansheng

TABLE OF CONTENTS

LIST OF FIGURES

Figure Page

LIST OF TABLES

CHAPTER I

INTRODUCTION

1.1 Motivation for This Research

Tremendous advances in computer memory and speed have made large scale, complex simulations of biological system possible. In order to simulate a biological process, a system of ordinary differential equations involving control mechanisms that have nonlinear components always needs to be solved. For instance, the Smoluchowski equation is used to obtain information for field-assisted pore formation in a bilayer lipid membrane. Details (spatial and temporal) of the electric fields, are in turn, governed by Maxwell's equations, and need to be coupled. Advances in numerical analysis have made the solution of complicated systems of ordinary differential equation faster, more precise, and relatively easier. However, for simple linear differential equations, it is easy to get an analytical solution by implementing traditional mathematical methods. Nonlinearities in the biological process often make it difficult or impossible to obtain an exact solution. Fairly good estimates, using numerical methods implemented on computers, can be obtained through reasonable simulation models. Spatial variation is a key feature in cellular mechanisms, which require us to analyze and solve spatially explicit partial differential equations.

In order to offer predictions or explanations of observed mechanisms, it is important to first construct mathematical models that can be used to yield quantitative data. The

---

The journal model for this work is the *Physical Review*.

output of the mathematical models, obtained through numerical simulations, can be used to mimic experimental conditions, or test scenarios that may be impossible to attain experimentally in a laboratory, and also to predict parameters or phenomena that might be ignored by experimentalists. Also, with simulation models one can test specific hypotheses concerning the role of individual mechanistic components, or make predictions that can be tested in the laboratory. Finally, simulations are not as costly as experimental work, and normally take much less time. Hence, they can be a very useful tool for testing, design and quantitative understanding.

1.2 Background of Electroporation

Electroporation or electropermeation has been widely interested and applied in the areas of molecular biology, biotechnology and medicine during the last two decades [1,2]. Important applications include clinical electroporation therapy (ETP) for treating various tumors and cancers [3-4], and gene therapy for gene delivery [5]. Under strong electrical pulse conditions, it is useful for killing bacteria and appears to be useful for decontamination [6].

Membranes are largely composed of amphiphilic lipids, which normally assemble into bilayer structures. This highly insulating configuration produces a large energy barrier to transmembrane ionic transport. Thus, the membrane of living cells has the capability for selective absorption. However, the integrity of membranes can be destroyed when a strong external electric field presents and aqueous pores start to be formed in the membrane. These will lead to an increase in transmembrane conductivity and diffusive permeability. These effects will also alter the electrical potential across the membrane [7]. This process is collectively called electropermeabilization or

electroporation. These electrical induced pores are commonly called "electropores." Their presence allows molecules, ions, and water to pass from one side of the membrane to the other without the limitation of selectivity. After the external electrical pulse is ceased, the pores close automatically in minutes [9] or may not close forever [10] leading to irreversibility and potential cell death. These effects are critically dependent on the duration and magnitude of the applied pulse. The reversible process of electroporation can be used to inject big size molecules such as DNA or some suitable drugs [11], which would otherwise not go into the cell due to the selectivity of the membrane and the small size of the embedded ionic channels. The irreversible process can be used to destroy cells such as bacteria and tumor cells in a localized manner [12].

1.3 Objectives and Scope of This Research

The exact mechanism for electroporation is still not fully understood, and the mathematical models are inexact and incomplete. Litster [12] and Taupin et al. [61] were the first to suggest the role of thermal fluctuations in pore formation, and the existence of threshold pore-formation energy. The basic model was subsequently extended to include electrostatic effects [14]. The biophysical description was translated into numerical models [15-17] based on the Smoluchowski equation [18] to predict the evolutionary pore dynamics. Since the pore dynamics are influenced by the trans-membrane potential, the voltage calculations need to be included for self-consistency and a comprehensive treatment. Variable surface tension due to pore formation should also be included, as it affects changes in cell surface area and influences the pore opening and closing process. It has also been shown that very interestingly that high-intensity, ultra-short pulsed electric fields can produce several outcomes that long and low intensity pulses cannot. A

good simulation model and theoretical explanation for the various effects observed are required. And the cellular manipulation by this kind of nanopulses is being highly interested.

The electrical properties of cell membranes are controlled by the existence and distribution of the pores in terms of their size and number. This occurs because the microscopic capacitance and conductance depends on the charging and ionic throughput across such pores. Pore distribution in the presence of an external electric field can be described by Smoluchowski's equation [13], which is implicitly voltage dependent. In order to estimate the changes in pore distribution, membrane potential, and the electrical properties have to be obtained self-consistently by solving the requisite partial differential equation subject to appropriate boundary conditions.

Changes in pore radius are affected by surface tension forces on the pore wall, diffusion of water molecules into and out of the pore, and an electric field induced force of expansion. This can lead to cell deformation, and is another interesting aspect worthy of study. Very simply, the Maxwell stress tensor [15] induced by polarization on the membrane and the imbalance of osmosis pressure induced by ionic flow through pores would lead to cellular deformation.

Based on the dynamic pore model and cell deformation model, time dependent transmembrane potential calculations have been developed in this research study. The primary aim is to understand cellular electroporation in response to an ultrashort (about nanosecond), high-intensity (~ 100 kV/cm) pulse, and to develop a quantitative model. In addition, microscopic approaches to the problem of pore-formation are also presented for

a model lipid bilayer membrane within an aqueous environment. Simulations are carried out dynamically at the molecular level based on Brownian motion.

Chapter 2 of this dissertation provides a literature review of the historical research on electroporation. Descriptions of simulation models such as a self-consistent model and time dependent transmembrane voltage-current calculation model for a single cell are given in Chapter 3. Various simulation methods are also described in detail in this chapter. Details of the various simulation results obtained and related problem discussions are dealt with in Chapter 4. Finally, conclusions and comments on future trends are included in chapter 5.

CHAPTER II

LITERATURE REVIEW AND BACKGROUND

2.1 Introduction

A quick review of ultra-short, high-intensive pulse electroporation is given in this chapter. The use of very high electric fields (~ 100kV/cm or higher) with pulse durations in the nanosecond range [19-21] has been a very recent development in bioelectrics. Traditionally, most electroporation studies have focused on relatively low external electric fields (less than a kilovolt per centimeter), applied over time periods ranging from several tens of microseconds to milliseconds [22]. From a practical standpoint, traditional electroporation and also the shorter electrical pulses could be useful for various applications ranging from cellular electroporation [23-25], production of hybridomas [26,27] the injection of xenomolecules such as hormones, proteins, RNA, DNA and chromosomes [28-34], the electrofusion of dielectrophoretically aligned cells [35,36], and the non-thermal destruction of micro-organisms [37-39]. In addition, *ex vivo* applications of electroporation have involved the treatment of white blood cells [40] and platelets [41] outside the body.

In *ex vivo* studies, electroporation was used to load drugs, and the cells were subsequently reintroduced for therapy. Manipulation of the oxygen binding capability [42] and the electro-insertion of proteins [43] has also been carried out. *In vivo* applications have included the delivery of potent anticancer drugs into solid tumors [44], [45].

There appear to be inherent advantages in using short electric pulses, and these include: (i) Negligible thermal heating, (ii) the ability to develop large electric fields and

peak powers, with a lower energy input, (iii) the possibility of selecting the desired time scales through pulse width manipulation, and (iv) the ability to penetrate the outer (plasma) membrane, and create large trans-membrane potentials across sub-cellular organelles. This can effectively open the way to intra-cellular electro-manipulation, without destroying the outer membrane [46].

2.2 Overview of High-intensity Pulses In Electroporation of Membranes

The application of high-intensity, pulsed electric-field work in recent years, has led to the following important observations:

(i) It is possible to maintain the integrity of the outer cell membrane despite the high (~ 200 kV/cm) electric fields. Experimentally, this has been gauged based on an absence of immediate Propidium Iodide (PI) uptake through the plasma membrane following an electrical pulse [47,51]. This result suggests that either the outer cell membrane remains relatively unporated, or the pore radii are relatively very small, or that transport of PI is being largely inhibited. We shall demonstrate that the pores are relatively small in size, and that water clustering impedes PI transport through the bio-membrane.

(ii) Multiple pulses have been observed to do more irreversible damage than single-shot electric shocks;

(iii) Irreversible cell damage is seen to occur at the intracellular organelles (e.g. mitochondria), while the outer membranes remain intact [46];

(iv) Calcium is released from the intracellular endoplasmic reticulum in response to external voltage pulses [46, 47];

(v) Cell apoptosis has been observed [46, 48] for cells subjected to short electrical pulses. In particular, apoptosis has been seen to be mitochondrial-dependent and completely

unrelated to plasma membrane electroporation. It may be mentioned here, that in the context of such *in vitro* experiments, apoptosis is defined by the presence of several well-defined markers, such as Annexin-V binding, caspase activation, a decrease in forward light-scattering during flow cytometry and of cytochrome *c* release into the cytoplasm.

(vi) Finally, the observed apoptotic behavior appears to depend on the pulse duration. Thus, for cells subjected to external electric fields *at a constant energy level*, much stronger apoptosis markers were observed only for the longer (~ 300 ns) pulses, less at the shorter (~ 60 ns) durations, and almost negligible effects for a short 10 ns pulse of the same input energy.

2.3 Introduction of Experimental Observations

Recently concrete experimental data were presented showing a pulse-width dependence on the cell apoptotic behavior [46]. For example, Figures 1(a) and 1(b) show the Annexin-VFITC fluorescence signal in Jurkat cells exposed to single electric pulses of 60 kV/cm and 150 kV/cm field intensities [46]. The durations were adjusted to 60 ns and 10 ns, respectively, to maintain a fixed net energy input. The cells were incubated with annexin-VFITC [as described in Ref. [46], and analyzed by flow cytometry. Nearly identical results were observed in 4–5 experiments, and HL60 cells (not shown) responded similarly. The central result is that a strong shift of the fluorescence signal to the right relative to the control (no pulse), indicative of annexin binding (an apoptosis marker), only occurs for the longer 60 ns pulse, and is quite negligible at the shorter 10 ns duration. Results of *in* vivo studies showing ultrashort pulse induced caspase activation (an apoptotic marker) through FITC-VAD-fmk fluorescence are shown in Fig.2. Pulse

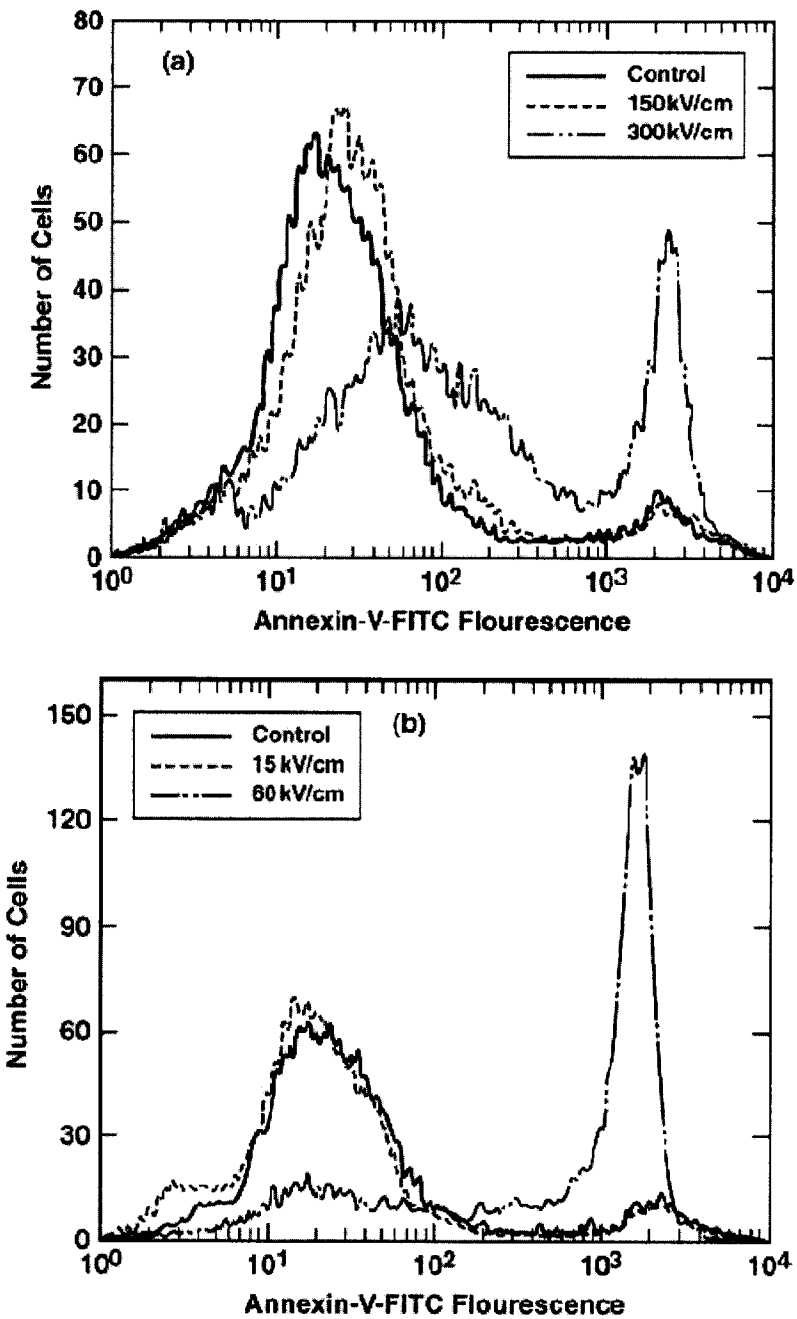

Fig. 1Experimental results showing Annexin-V-FITC fluorescence in Jurkat cells subjected to an electric pulse of different magnitudes and fixed input energy [28]. (a) Data for a 10 ns pulse, and (b) Data for a 60 ns pulse.

durations of 10 ns and 60 ns were used, with a fixed total energy input of 1.7 J/cc from the external field. The activation was seen to be stronger for the longer 60 ns pulse, as compared to the 10 ns duration. Similarly, Fig. 3 shows data on caspase activity in Jurkat cells subjected to a single pulse of variable duration, but fixed total energy of 1.7 J/cc. Three pulse durations of 10 ns, 60 ns and 300 ns were used. Longer duration pulses are again seen to produce stronger apoptotic behavior, with a clear monotonic trend.

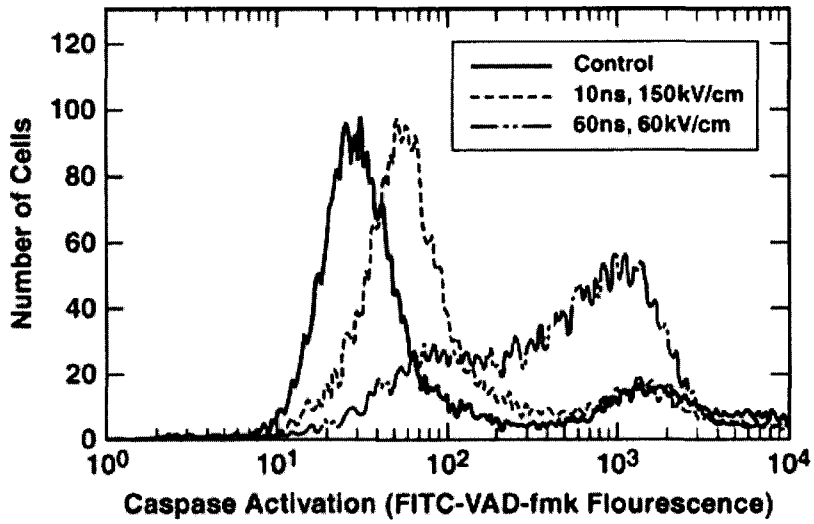

Fig. 2 *In* vivo studies showing ultrashort pulse induced caspase activation (an apoptotic marker) through FITC-VAD-fmk fluorescence. Pulse durations of 10 ns and 60 ns were used, with a fixed total energy input of 1.7 J/cc from the external field [28].

The ability of the short, high-intensity pulses to bring about intracellular damage and apoptotic behavior is not well understood. However, there is now mounting evidence that apoptosis is controlled and regulated by mitochondria in cells [49-53]. This suggests that mitochondria should perhaps be a focal point for the study of cell death and irreversibility brought about by the application of ultrashort electrical pulses. Mitochondria are the cellular power plants assigned to ATP production and maintain a

transmembrane proton gradient to drive a variety of tasks [54]. Observations of apoptosis have been indicative of a possible three-step mitochondrial model: (i) of a possible three-

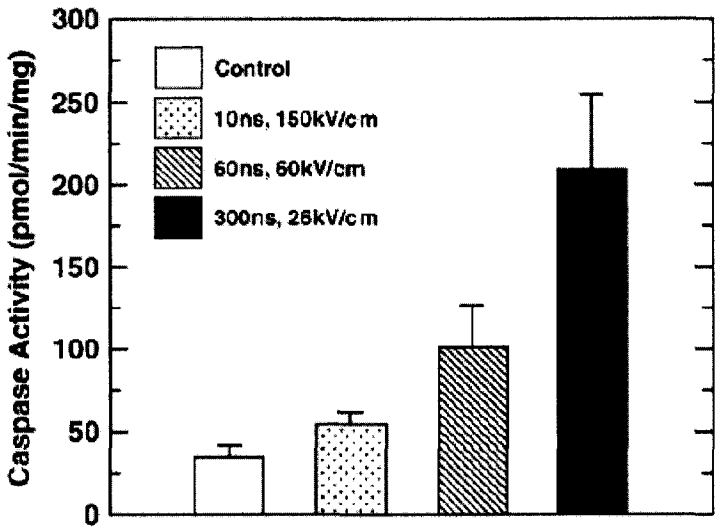

Fig. 3 Data showing caspase activity in Jurkat cells subjected to a single pulse of variable duration, but fixed total energy of 1.7 J/cc. Longer duration pulses are seen to produce stronger apoptotic response [28].

step mitochondria model: (i) an initial phase during which signal transduction cascades or damage pathways are activated, (ii) a mitochondrial phase during which the mitochondrial membrane function is lost, and (iii) a final phase involving protein releases causing the activation of catabolic proteases and nucleases. It has also been established that the release of cytochrome *c* from mitochondria into the cytosol is able to activate procaspases that amplify the cell death process [55]. Cytochrome c is a six-coordinate, low-spin heme iron species, and is primarily located at the outer face of the inner mitochondrial membrane [56]. This release of cytochrome *c* and other pro-apoptotic molecules has been shown [50-53] to be facilitated by a transient opening of the mitochondrial permeability transition pore (MPTP). This mitochondrial permeability

transition (MPT) appears to be driven by several factors including calcium overload, oxidative stress, and mitochondrial membrane depolarization. The MPT operates at the crossroads of two distinct physiological pathways, i.e, the Ca^{2+} signaling network during the life of cells, and the effector of apoptotic cascade during Ca^{2+} dependent cell death [57]. The role of transmembrane potential (along with the pH) on MPT regulation and programmed cell death has now been recognized as well [58]. Since voltage changes are associated with the MPTP that in turn is linked to apoptosis, it is natural to seek a possible link between cell death and transmembrane voltage changes induced by the application of an external voltage pulse.

2.4 Summary

High-intensity, pulsed electric fields have been widely applied in membrane electroporation, and the membranes of a cell can be selectively targeted for loading big sized molecules for therapy purpose or non-thermal destruction. Transmembrane voltage changes attributed to membrane lipids rearrangements are significant signs of cellular physiology changes. Computer simulations provide a feasible way to better understanding the mechanisms, and predict useful parameters what are difficult to be obtained from experiments.

CHAPTER III

MODELING AND SIMULATION DETAILS

3.1 Introduction to Simulation Approaches

The principal goal of lipid membrane and biological cell simulations conducted in this study is to determine the behavior of biomembranes and cellular responses to an externally applied electrical field. The biomembrane simulations discussed in this chapter are primarily electrical in nature, and concentrate on the transmembrane current and voltage response to an applied electrical pulse or pulses. Section 3.2 focuses on a self-consistent current model based on the time-dependent Smoluchowski equation. Section 3.3 provides an improved energy model with inclusion of dynamical surface tension. Electromechanical deformation in cells associated with the Maxwell stress tensor arising from the applied electric field is also discussed in section 3.4. A three-dimensional (3-D), time-dependent current-voltage solver for the electrical membrane response is described in section 3.5. The simulation schemes discussed in sections 3.2-3.5 use fixed parameter values to quantify some of the physical processes and effects. However, due to the complexity and dynamical nature of the biological system, the parameters are often unknown and likely to change from cell type and physical condition of the cells. This makes the biological response somewhat harder to gauge, and influences the accuracy of numerical predictions. A more satisfying and accurate solution would be to minimize the parameter set, and use approaches based on first-principles to obtain an accurate, dynamic, many-body model. This has been done in section 3.6, where molecular dynamic

simulation of biomembrane behavior at the atomic level are discussed and implemented. The details of our "ball-spring model" can be found in section 3.6.

3.2 A Self-consistent Current Model

3.2.1 Introduction

In our time-dependent simulation model of cell bio-electric response, the internal electric fields (i.e., though set up within the simulated cell volume) arising from an external step voltage are computed based on a self-consistent solution of the current continuity and Laplace equations. Details of the electric field calculations for a spherically symmetric cell are provided later in this section. In practice, cells can be elliptical (more specifically, prolate/oblate spheroids) either due to their naturally occurring shape, or due to field related deformations. However, the creation of strong polarization at regions of sharp curvature effectively shields the electric fields, and works to minimize the disparity resulting from geometric asymmetries. Besides, in a solution, individual cells are expected to retain a nearly spherical shape due to forces arising from osmosis and the cytoplasmic fluids. Hence, the spherical geometry assumed is expected to be roughly correct, and has been used in our simulation work. The model implicitly assumes that the time delay for cellular reorientation and alignment with the external field is negligible compared to the times scales for the poration process. Hence, the reorientation process has been ignored. This is based on an extrapolation of the characteristic delay times from the experimental data of Eynard *et al.* [59] to the high electrical fields of interest here. Current flows are computed at each time step from a continuum Nernst-Planck-type model that includes diffusion corresponding to the local electric fields. The current flow is either due to the physical transport of ions in the cell

cytoplasm and intra-cellular fluid, or due to displacement currents. Displacement currents, which correspond to the charging of capacitors, typically arise across regions of minimal conductivity such as membranes. The creation of large membrane voltage can lead to localized breakdown and pore formation. This aspect has to be considered in any modeling scheme. Under such porated conditions, transport can additionally occur through the transient aqueous pathways (pores). The magnitude is dictated by the time-dependent pore distribution. Hence, the requisite details regarding pore size and areal densities need to be computed in a time-dependent fashion. These tasks have been implemented in this research on the basis of the Smoluchowski equation. Details of this equation and overall numerical model are discussed next.

3.2.2 Pore Formation Energy Function and the Smoluchowski Equation

In keeping with the literature [60], it is assumed here that two types of pores exist. The hydrophilic pores have their walls lined with water-attracting heads of lipid molecules, and are conducting. Hydrophobic pores are non-conducting, and simply represent gaps in the lipid bilayer of the membrane. Each of the two pore types is characterized by energy of formation E(r) that is a function of the pore radius r. In the present analysis, we have chosen to use the following pore energy function in keeping with the published and accepted model [60, 62, 10, 65]:

$$E(r,t) = 2\pi hr\sigma(\infty)[I_1(r/r_0)/I_0(r/r_0)] - \pi\alpha_p V^2 r^2 \quad , \qquad (3.2.1a)$$

$$E(r,t) = 2\pi\gamma r - [\int_0^r 2\pi\Gamma(r^*)r^* dr^*] + (C/r)^2 - \pi\alpha_p V^2 r^2 \quad , \qquad (3.2.1b)$$

for hydrophobic and hydrophilic pores, respectively. In the above, I_1 and I_0 are the modified Bessel functions of the zeroth and first order, respectively, h is the membrane

thickness, $\sigma(\infty)$ is a constant equal to 5×10^{-2} Nm^{-1}, while r_0 represents a characteristic length scale over which the properties of water change between the interface and the bulk. The value of r_0 is taken to equal 1 nm. The trans-membrane potential "V" is included in the last term. Also, γ is the energy per unit length of the pore perimeter, while Γ is the energy per unit area of the intact membrane. In practice, the Γ value in a finite biological membrane changes with osmotic pressure, the pH value, and/or with perforations upon stretching. For example, a simple heuristic model has recently been used to describe such changes [67] with $\Gamma(r) = \Gamma_0[1 - r^2 / r_\infty^2]$. This is based on the idea that tension is proportional to the membrane area, at least to first order. Hence, it follows that pore formation and growth will lead to reduction in the Γ parameter. The primary effect of such variations in Γ would be the creation of an additional local minimum in the pore energy function. From the standpoint of electroporation, this means that instead of expanding indefinitely beyond the unstable maxima, the pores become quite large, but ultimately stabilize at this high radial value. The variable tension concept had been proposed by Winterhalter and Helfrich [68] as well. Typical values for the various parameters are given in Table 1 and were taken from various sources in the published literature. Surface tension of the membrane, the line tension of the pore edge, and the membrane capacitance contribute to E(r). The third term in Eq. (3.2.1b) represents the steric repulsion between lipid heads lining the pores [59, 66], and is responsible for the increase in pore free energy with shrinking radius. The value of C in Eq. (3.2.1b) was chosen to be 9.67×10^{-15} $J^{1/4}$ m in keeping with the reports by Neu and Krassowska [66] as it yields values close to those measured by Glaser *et al.* The last term in Eq. (3.2.1b) represents the capacitive contribution to the energy in the presence of a transmembrane

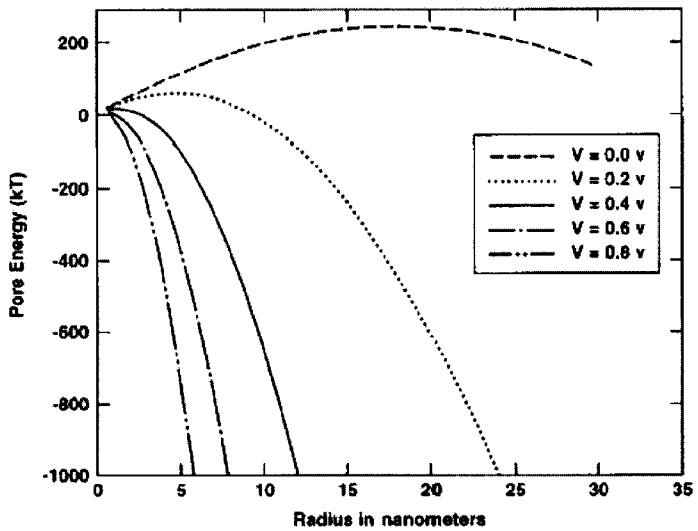

Fig. 4 The pore formation energy $E(r)$ of hydrophilic pores for various membrane voltages.

potential V. The coefficient a_p is a property of the membrane and its aqueous environment. In the simplest continuum approximation, it is expressed in terms of the membrane thickness h and the permittivities ε_w and ε_m of water and the membrane, respectively, as: $a_p = (\varepsilon_w - \varepsilon_m)/[2h]$. It might be mentioned that other models have been proposed as well that take into account different factors in the pore energy calculation. For instance, formulations based on the role of osmotic pressure [61], electro-compression of the lipid bilayer [69], interaction with membrane cytoskeleton [70], and cellular deformation [68] exist. While the expression for E(r) would change somewhat on the basis of the alternative theories, the basic trends and qualitative physical behavior would remain unaltered.

The energy function E(r) determines the "drift flux" for pores in r space and therefore, governs the growth or contraction of pores at any given radius r. In general, the presence

of a membrane voltage reduces the maxima, and can even quell the energy barrier completely beyond a critical voltage value. For transient voltage pulses, stability would

Table 1 Parameters used for the theoretical model

Parameters	Value	Source
D (m^2s^{-1})	5×10^{-14}	[86]
γ (Jm^{-1})	1.8×10^{-11}	[86]
Γ_0 (Jm^{-2})	10^{-3}	[86]
C ($J^{1/4}m$)	9.67×10^{-15}	[10]
K_w (Fm^{-1})	$80\times8.85\times10^{-12}$	[86]
K_m (Fm^{-1})	$2\times8.85\times10^{-12}$	[86]
h (m)	5×10^{-9}	[10]
α_p(Fm^{-2})	6.9×10^{-2}	[10]
v_c ($m^{-3}s^{-1}$)	2×10^{38}	[62]
v_d (s^{-1})	10^{11}	[63]
r_0 (m)	1×10^{-9}	[63]
σ_0 (Nm^{-1})	5×10^{-2}	[63]
σ_{in} (Sm^{-1})	0.455	[91]
σ_{out} (Sm^{-1})	5.0	[91]
σ (Sm^{-1})	1.3	[91]
A (V)	2.5	[63]
$n = h_l/h$	0.15	[91]
r (m)	65×10^{-9}	[66]

depend on the ability of pores to drift past the barrier maximas within the duration of the applied voltage pulse. As in previous treatments, it is assumed here that the formation of pores is a two-step process. All pores, are initially created as hydrophobic/nonconducting at a rate S(r) per unit area of the membrane, during every time interval dt. This rate is given as:

$$S(r) = \{(v_c h)/(k_B T)\}[dE(r)/dr]\exp[-E(r)/(k_B T)]drdt \quad , \qquad (3.2.2)$$

where v_c is an attempt rate density, E(r) the energy for hydrophobic pores, T the operating temperature, and k_B the Boltzmann constant. This assumes that the use of a kinetic collisional theory remains valid for nongaseous phases as well. If a nonconducting pore is

created with a radius r > r* (= 0.5 nm), it spontaneously changes its configuration and transforms into a conducting, hydrophilic pore. All conducting pores then survive as long as their radii remains larger than r*. Destruction of a conducting pore occurs only if it drifts or diffuses in r space to a value below r*. Due to the exponential term in Eq. (3.2.2), most pores are created with very small radii. The Smoluchowski equation (SE) governs the pore dynamics, and is given in terms of the pore density distribution function n(r, t) as:

$$\frac{\partial n(r,t)}{\partial t}+\frac{D}{k_B T}[\frac{\partial\{E(r)n(r,t)\}}{\partial r}]-D\frac{\partial^2 n(r,t)}{\partial r^2}=S(r) \quad , \qquad (3.2.3)$$

where S(r) is the source term as given in Eq. (3.2.2), while D is the pore diffusion constant given in Table 1. Thus, the SE is a continuum model for the drift and diffusion of pores. The process of diffusion represents a "random walk" of the pore radius in r space. Physically, this is brought about by fluctuations in the radius in response to water molecules and other species constantly entering and leaving the pores. Numerical simulations of the dynamic pore distribution were carried out based on a time-domain, finite-difference discretization of the governing Smoluchowski equation. An upperbound r_{max} of 2000 Å was set on the pore radius, and this entire r space was uniformly divided into 5000 segments to yield a constant grid spacing dr of 0.4 Å. This ensured that the set limit was much larger than the critical radius r_c at which the energy function E(r) has a local maxima. Two suitable boundary conditions were imposed for the second-order partial differential equation. A reflecting boundary was assigned at r = r_{max}, which was implemented by setting the pore flux to zero at r = r_{max}. Mathematically, this amounts to a Neumenn condition: $\left|dn(r,t)/dr\right|_{r=r_{max}} = -[dE(r,t)/dt][n/(k_B T)]_{r=r_{max}}$. At the other end, absorbing boundary conditions were implemented by setting n(0, t)=0. The time step dt,

in these simulations was chosen to be much smaller than the fluctuation rate v_d that represents the fastest time constant in the system[10]. Specifically, dt = 10^{-11} s was used. As an initial condition prior to the application of an external voltage, the pore density was taken to be zero at all the grid points.

3.2.3 Legendre Polynomial Current Model

The pore formation and growth is controlled by the energy function E(r) that depends, among other factors, on the trans-membrane potential V as given in Eq. (3.2.1a and 3.2.1b). Thus, the time-dependent value of V provides the driving force and dictates the pore dynamics. It therefore, becomes important to evaluate this potential for a given cell size and external voltage pulse characteristic. This section discusses the trans-membrane potential calculation.

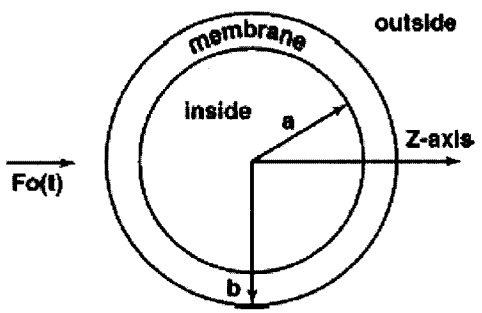

Fig. 5 Schematic of the model used to represent a cell in a suspension for potential calculations.

Here, the external electric field F(t) was taken to have the exact time-dependent shape corresponding to the external pulsed wave form. For purposes of calculating the transmembrane potential, the coupled Laplace and current-continuity equations were solved at each time step. The schematic shown in Fig. 5 was used to represent a cell

suspended in a medium, and the relevant equations applied to this geometry. The geometric model is similar to that used by Grosse and Schwan [71] for analyzing membrane potentials induced by alternating fields. The inner region was assumed to be spherical in shape with a radius of a, homogeneous and characterized by a conductivity σ_{in}. The applied electric field F_0 (t) was taken to be along the *z-axis*. The cellular membrane was assigned a thickness *b-a*, while the outer region denoting the suspension was assigned conductivity σ_{out}. Due to spherical symmetry, the potentials that must satisfy the Laplace equation, can be expressed as:

$$U_{in}(r,t) = A_0(t)P_0 + A_1(t)rP_1 + A_2(t)r^2P_2 + \ldots = \sum_{j=0,\infty} A_j(t)r^jP_j \quad , \tag{3.2.4a}$$

$$U_{in}(r,t) = A_0(t)P_0 + A_1(t)rP_1 + A_2(t)r^2P_2 + \ldots = \sum_{j=0,\infty} [B_j(t)r^jP_j + C_j(t)P_j / r^{j+1}] \, , \tag{3.2.4b}$$

$$U_{out}(r,t) = -F_0(t)rP_1 + \sum_{j=0,\infty} D_j(t)P_j / r^{j+1} \, , \tag{3.2.4c}$$

where $U_{in}(r,t)$, $U_{mem}(r,t)$ and $U_{out}(r,t)$ are the potentials at the inner, the membrane, and outer regions, P_j is the j th order Legendre polynomial, and F_0 (t) the externally applied electric field. Also, A_j (t), B_j (t), C_j (t), and D_j (t) are the coefficients of the Legendre series expansions that can be determined by applying matching boundary conditions at the interfaces of the three regions. Here, the Laplace instead of Poisson's equation has been used on the assumption that charge inequalities arising from ionic transport during the electroporation process can be ignored on the short time scales. As will be shown later, the current flows are not very large and so charge transfer during the

ultrashort time scales of interest here, are indeed minimal. Invoking continuity in the potential and current density then leads to the following boundary conditions:

$$U_{in}(r=a,t) = U_{mem}(r=a,t) \quad , \tag{3.2.5a}$$

$$U_{mem}(r=b,t) = U_{out}(r=b,t) \quad , \tag{3.2.5b}$$

$$\sigma_{in}\frac{\partial U_{in}(r,t)}{\partial r}|_{r=a} = \sigma_{out}\frac{\partial U_{out}(r,t)}{\partial r}|_{r=b} \quad , \tag{3.2.5c}$$

$$-\sigma_{in}\frac{\partial U_{in}(r,t)}{\partial r}|_{r=a} = C_M\frac{\partial V_{mem}(r,t)}{\partial t}|_{r=b} + J_{mem}(t) \quad , \tag{3.2.5d}$$

where C_M is the membrane capacitance, $V_{mem}(t)$=[U_{mem}(r=b,t)-U_{mem}(r=a,t)] is the membrane potential, and $J_{\text{mem}}(t)$ is the conduction current density across the membrane through the pores. Values of the conductivity parameters and the membrane capacitance have been reported in the literature [73], and are used here as given in Table 1. Straightforward, but tedious manipulation of Eq. (3.2.5) yields the following expression for the time-dependent membrane potential $V_{mem}(t)$:

$$V_{mem}(t) = A(t)\cos(\theta)[(b-\frac{b^3}{a^2})(1+2\sigma_{out}/\sigma_{in})/(b^3/a^3+2\sigma_{out}/\sigma_{in})-(b-1)]+ \\ 3\cos(\theta)F_0(t)(\sigma_{out}/\sigma_{in})/(b^3/a^3+2\sigma_{out}/\sigma_{in}) \quad , \tag{3.2.6a}$$

where θ is the angle with respect to the z axis (and hence, the applied electric field direction), and A(t) satisfied the following ordinary differential equations:

$$C_M\frac{dA(t)}{dt}[(b-\frac{b^3}{a^2})(1+2\frac{\sigma_{ut}}{\sigma_{in}})/(\frac{b^3}{a^3}+2\frac{\sigma_{ut}}{\sigma_{in}})-(b-a)] = -J_{mem}(t)- \\ \sigma_{in}[2\frac{\sigma_{ut}}{\sigma_{in}}(\frac{b^3}{a^3}-1)A(t)-3\frac{\sigma_{ut}}{\sigma_{in}}F_0(t)\frac{b^3}{a^3}]/(\frac{b^3}{a^3}+2\frac{\sigma_{ut}}{\sigma_{in}}) \quad . \tag{3.2.6b}$$

Since steady-state results of the transmembrane potential have been derived in the literature, an indirect validation of the above equation can easily be obtained by

evaluating V_{mem} (t) in the long time limit. Setting the time derivative term to zero yields an expression for A($t \to \infty$). Using this expression in equation (3.2.6a), provides the steady-state transmembrane potential: V_{mem} = -1.5aE cos(θ) for b~a. This steady-state result is in accordance with the expression reported and experimentally verified in the literature [73, 74]. It is worth mentioning that the time-varying field of equation (3.2.4) would produce a force at the membrane in accordance with the Maxwell stress tensor [75]. It is conceivable that such stress will lead to changes in the volume and shape of the cells. Experimental scattering data on cells subjected to high-voltage pulses confirms such dynamical variations in size. Cell shrinkage in the context of apoptosis following high-voltage pulses is also possible. Such aspects can be analyzed based on the theory presented here.

3.2.4 Current-Voltage Relation

The conduction current density J_{mem} (t) needs to be specified in order to solve for the potentials in Eq. (3.2.6). A one-dimensional approximation of the Nernst-Planck expression for ionic flow has often been used in the literature [76]. This gives to the following current-voltage relation:

$$I(t) = \pi\sigma R^2(t)N(t)\{\exp[qV_{mem}(t)/(k_BT)]-1\}/(\int_0^h \exp[qV_{mem}(t)(1-x/h)/(k_BT)+w(x)]dx)\,, \tag{3.2.7}$$

where R(t) is the pore radius, σ the conductivity of the aqueous solution that fills the pore, w(x) the energy barrier to ionic flow through the pores, h is the membrane thickness, and N(t) the pore density. A simple trapezoidal form for w(x) as given by:

$$w(x)=qA/(k_BT)(x/h_1) \text{ for } 0 \le x \le h_1 \tag{3.2.8a}$$

$$w(x)=qA/(k_BT) \text{ for } h_1 \leq x \leq h-h_1 \quad , \qquad (3.2.8b)$$

$$w(x)=qA/(k_BT)[(h-x)/h_1] \quad , \qquad (3.2.8c)$$

which has been used for the barrier energy, and will be applied here. In the above, A represents the peak barrier height under zero bias. Values of s and A are known to be roughly 1.3 S/m [72] and 2.5 V[10], respectively. The parameter h_1 is the length of the entrance region of the pore over which the barrier profile would be changing linearly for an unbiased cell. Its value is roughly 0.15 times the membrane thickness. In addition, an ionic component, I ion, which is orders of magnitude lower in strength, has to be included. This ionic current density is [72]:

$$I_{ion} = 1.9\,(V_{mem} + 0.083) \quad . \qquad (3.2.9)$$

The 83 mV in the equation above represents the reversal potential.

3.2.5 Summary of the Simple Electrical Approach

A simple numerical model for calculations of the currents and voltages within a volume containing a cell subjected to an external voltage pulse has been discussed. The model includes pore formation, and hence, a conductivity modulation across the cell membrane. It is based on the continuum Smoluchowski approach, and is somewhat simplified since equations (3.2.7) and (3.2.8) are somewhat inaccurate for the following reasons.

(i) First, the barrier peak A is assumed to be independent of the pore radius. This is physically inaccurate. As shown by Parsegian [74], for example, the barrier is a monotonically decreasing function of the radius r implying that it is easier for ions to get through wider pores. An approximate form, which is correct for an infinitely long

cylindrical pore geometry, for w(r) has been derived to be [74]: $w(r) = 5\times10^{-9}$ /r. In our calculations, this w(r) function was explicitly used in Eq. (3.2.8).

(ii) Next, Eq. (3.2.7) treats the pore radius to be a constant that is incorrect for two reasons. Not only would the radius of the pores change under transient conditions upon the application of an external voltage waveform, but also the pores would not all be identical in size. The distribution n(r, t) as predicted by the Smoluchowski equation, would impart a heterogeneous spread in the *R* parameter.

(iii) Finally, N(t) that is an integral quantity needs to be obtained through a suitable integration of n(r, t) over *r* space. Treating N(t) as a fundamental independent variable is incorrect.

The 83 mV in the equation above represents the reversal potential. To redress the above shortcomings of equation (3.2.7), a somewhat modified current-voltage *(*I-V) characteristics were used in this study. The I-*V* relation was taken to be which includes integration in r space over the time-dependent distribution n(r, t). In the process, the role of intercellular variations and the size distribution of pores are both taken into account. A distribution of barrier energies was used allowing for fluctuation. It, therefore, represented a more physical model of an actual cellular colony.

As a final comment, it may be pointed out that the present model is non-Markovian in nature, and hence, includes memory effects. The kinetic rates depend on the membrane voltage, and hence, vary with time. Consequently, the model describing the evolution of the biological system, not only depends on the initial starting state, but also on the details of the time-dependent voltage sequence. This formulation, therefore, goes beyond the Markovian treatments based on Poisson models [77,78].

3.3 An Improved Energy Model

3.3.1 Introduction

The most direct evidence of an inadequacy of the independent pore, constant tension model described above, with its energy maxima at around 18 nm comes from experimental measurements. For instance, pores with stable diameters up to micrometers in size have been reported [79, 80]. This observation is clearly contrary to the theoretical prediction of either complete pore closure or unbounded expansion leading to rupture.

Similarly, stabilization of pore radii within the 20–60-nm range has been reported by Chang and Reese [81] in their studies of red blood cells. The resolution of their experiments allowed the pores to be seen 3 ms after an applied voltage pulse, when their radii were 10–20 nm. The pores continued to grow, but then stabilized at around 20–60 nm after 40 ms. Given such time-resolved experimental data, it becomes clear that the simple electroporative-energy model needs to be modified to yield better predictions and more accurate, physical results. An attempt towards this goal is discussed in this section. The model developed here allows for a variable surface tension, incorporates the effects of finite conductivity on the electrostatic correction term, and is dynamic in nature through a dependence on both the cell voltage and pore density. These changes make $E(r)$ self-adjusting in response to pore formation, without causing uncontrolled growth and expansion. It may also be pointed out that though a few recent studies have presented an inclusion of a coupling between membrane tension and pore area [80, 82, 83], these analyses were either limited to one giant pore or to a population of pores with identical radii. Also, changes associated with finite conductivity and the dynamic nature had been ignored.

3.3.2 Electro-Static Contribution $E_{ES}(r)$ of the Pore Energy Function

Equation (3.2.1b) is modified here to include a dynamical aspect and a dependence on the pore population density into $E(r)$. Furthermore, voltage-dependent Born energy corrections arising from the presence of ions in water near pores, as suggested by Pastushenko and Chhizmadzhev [84] and Barnett and Weaver [85], have been incorporated. The electro-static contribution $E_{ES}(r)$ to the formation energy then becomes:

$$E_{ES}(r) = -\pi \frac{\varepsilon_w - \varepsilon_m}{2h} V^2 \int_0^r \alpha^2(r'') r'' d'', \tag{3.3.1}$$

where $\alpha(r) = (1 + \frac{\pi r k_P(r)}{2hk_B})^{-1}$, k_B is the bulk electrolyte conductivity, $k_P(r)$ the bulk electrolyte conductivity, $k_P(r)$ the conductivity in a pore of radius "r." The bulk conductivity k_B is given in terms of the electronic charge q(=1.6×10^{-19} C), concentration Ci , mobility μ of the ith ion, and its charged state Zi as $k_B = \sum_i (qZ_i)^2 \mu_i c_i$. Similarly, the conductivity $k_P(r)$ is roughly given as [84, 86]:

$$k_B(r) \sim \sum_i (qZ_i)^2 \mu_i c_i H_i(r) \times \exp(\frac{P\{\varepsilon_m \varepsilon_w\}(qZ_i)^2}{4k_B T \pi r \varepsilon_m}), \tag{3.3.2a}$$

wherer k_B = 1.38×10^{-23} J/K is the Boltzmann constant, $H_i(r)$ the steric hinderance factor, and with $P(\varepsilon_m / \varepsilon_w)$ being the function described by Parsegian [87]. The factor $Hi(r)$ has been given by Renkin [88] in terms of r_i , the radius of the ith ion, as :

$$H_i(r) = \{1-(r_i/r)^2\}[1-2.1(r_i/r)+2.09(r_i/r)^3-0.95(r_i/r)^5] \ . \tag{3.3.2b}$$

Hence, when the pores are all small, the α term in Eq. (3.3.1) goes to unity (i.e., in the r → 0 limit), while α >0 in the opposite limit of large pore radius r. Physically, this implies that the usual electrostatic energy factor is valid for small pore populations when the radii are also small. However, as the pores begin to grow, the contribution to the energy $E(r)$

begin to decrease in magnitude. In terms of Fig. 4, this translates into a flattening of the $E(r)$ curve beyond the potential barrier in the presence of externally applied voltages.

3.3.3 Dynamic Surface Tension

Next, a pore-density-dependent correction to the surface tension parameter Γ is discussed. Considering a lipid bilayer of total area "A" consisting of $2M$ lipid molecules, the total interfacial energy "W" in the absence of any pores is given as[89]:

$$W = 2M\eta = 2M[\sigma' a + K/a] \cong 2[A\sigma' + KM^2/A], \tag{3.3.3}$$

where σ' is the interfacial energy per area of the hydrocarbon-water interface (~2×10^{-2} Jm^{-2}), "a" is the area per lipid head, and "K" a constant [89]. Equilibrium is determined by the minima of the energy W, and hence, is given by the condition $\partial W/\partial A = 0$. This yields a minimum value $W_0 = 4\sigma' A_0$ and $K = \sigma'[A_0/M]^2$, where A_0 is the equilibrium area for corresponding to W_0. In general, however, for a total area A different from the equilibrium level A_0, the energy W can be expressed as $W(A) = 2\sigma'[A + A_0^2/A]$. The surface tension Γ_{eff} can effectively be defined in terms of the energy differential since the energy is given as:

$$4\sigma' A_0 + \int_{A_0}^{A} \Gamma_{eff}(A')dA' = W(A) \quad . \tag{3.3.4}$$

Hence, $\partial W/\partial A = \Gamma_{eff}(A) = 2\sigma'[1-(A_0/A)^2]$ and the effective tension is zero when the lipid bilayer area exactly equals the equilibrium value of A_0. Usually, the area A slightly exceeds the equilibrium level A_0. Roughly A/A_0~1.0125 since this ratio yields a tension of 10^{-3} Jm^{-2}, a value that has been used in the literature.

Upon the formation of pores of total area Ap, the total area A remains the same. However, the effective membrane area sections reduces to A_M where A_M=A-A_P. Consequently, the expressions of the energy $W(A_M)$ and the tension Γ_{eff} change according to

$$W(A_M) = 4\sigma' A_0 + \int \Gamma_{eff}(A')dA' = 2\sigma'[A - A_P + A_0^2/(A - A_P)], \quad (3.3.5a)$$

$$\text{and } \Gamma_{eff}(A_M) = \frac{\partial[2\sigma'\{A - A_P + A_0^2/(A - A_P)\}]}{\partial A} = 2\sigma'[1 - \{A_0/(A - A_P)\}^2] \ . \quad (3.3.5b)$$

The effective tension in the presence of pores can, therefore, be expressed in terms of the value without pores as :

$$\Gamma_{eff}(A_P) = \Gamma_{eff}(A_P = 0) \times [1 - \{A_0/(A - A_P)\}^2]/[1 - \{A_0/A\}^2]. \quad (3.3.5c)$$

It follows from Eq. (3.3.5c) that the effective tension can be positive, zero or even negative. The zero level corresponds to a situation where the pore area A_P=A-A_0. For higher pore areas (i.e., larger average pores), the Γ_{eff} value can be negative as the membrane is under compression. Finally, the pore area in the above analysis represents the average value and hence, is given in terms of the actual pore density distribution function $n(r,t)$ as :

$$A_P(r,t) \sim A_0[\int_0^r 2\pi r^* n(r^*,t)dr^*], \quad (3.3.5d)$$

provided mutual pore coupling and pore-pore interactions are negligible.

3.3.4 Summary of the Improved Model

The simpler model for pore formation presented earlier in section 3.2 can be improved for a more physical and accurate representation of the inherent physics. Basically, the dynamic nature of the parameters, for example the surface tension, needs to

be taken into account. Obviously, as the pore density function $n(r,t)$ changes with time in accordance with the Smoluchowski equation, the cell size, membrane density and elasticity is expected to change. In this section, some of the dynamic corrections have been discussed. It is shown that pore area $A_P(r,t)$-dependent variable surface tension can become quite important for situations involving transient voltage pulses. In such cases, the voltage could fall to zero quickly, thereby, canceling out the electrostatic contribution to $E(r)$. However, the $A_P(r,t)$ term would continue to affect dynamical evolution over much longer periods.

Putting all of the above factors together, the pore formation energy $E(r,t)$ can comprehensively be expressed in terms of the following equation:

$$E(r) = 2\pi\gamma r - \{\int_0^r 2\pi\Gamma_{eff}(A_P[r^*,t])r^* dr^*\} + (C/r)^4 - \pi\frac{\varepsilon_w - \varepsilon_m}{2h}V^2\int_0^r \alpha^2(r'')r''d'' \quad , \quad (3.3.6)$$

with $A_P[r^*,t]$ changing dynamically as dictated by Eqs. (3.1.3) and (3.3.5d).

3.4 Electromechanical Deformation

3.4.1 Stress and Tensions

When cells are subjected to external fields, electric stresses arising from the Maxwell tensor can be expected to become operative. These stresses can then, in principle, deform the cell and alter the shape. In this section, some attention is given to such field-assisted deformations of a generic, spherical cell. Our basic stress model is based on the classical small deformation theory of thin, elastic shells [90]. Since the thickness of cell membranes is on the order of 5 μm, compared to their radii of ~1 μm, the shell theory is quite appropriate. The forces and moments acting on a typical shell element are given in Fig. 6. Two meridians and two parallel circles, each indefinitely

close together, have been shown. Following the notation of Flugge [90], ϕ is the angle between a normal to the shell and its axis of revolution, while θ is the meridional angle.

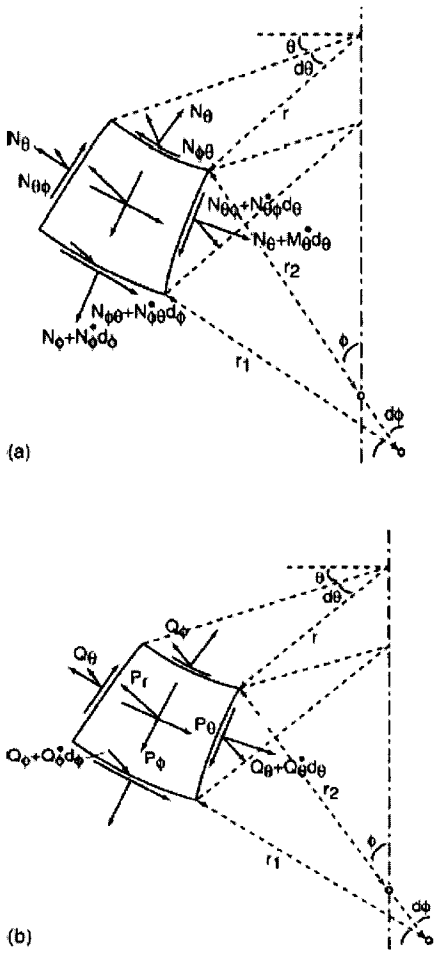

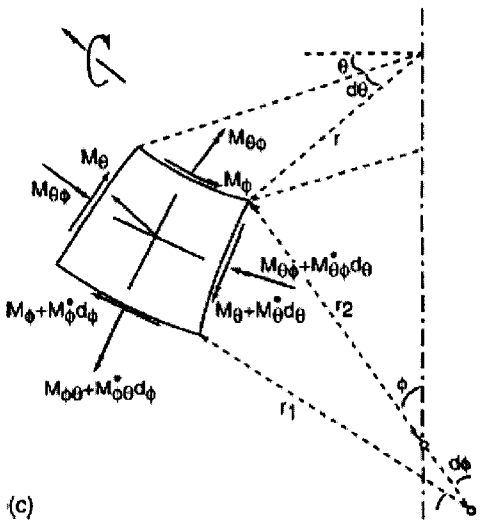

Fig. 6 Schematic of a typical thin shell element and the associated forces and moments. (a) The forces $N_{\theta\phi}$, N_θ, N_ϕ; (b) Q_θ, Q_ϕ, Pr, P_θ, P_ϕ; and (c) the moments $M_{\theta\phi}$, M_ϕ, and M_θ.

Also, N_ϕ denotes the meridional force per length, N_θ the hoop force per length, and $N_{\phi\theta}$ the shear. Furthermore in Fig. 6, p_r, p_ϕ and p_θ are the externally imposed stresses (which could include internal osmotic pressure), while r is the distance from the axis of rotation, r_1 the radius of curvature, and r_2 the distance of intersection of the radius of curvature and the axis of revolution. In the present context, p_r, p_ϕ and p_θ will be non-zero due to the presence of the Maxwell stress tensor associated with the external field. It is assumed that the osmotic pressure contributions to p_r, p_ϕ and p_θ are negligible compared to the Maxwell stress produced by the high electric fields. From the geometry, $r = r_2 \sin(\phi)$, while the elemental distance "ds" along the meridian is given by: $ds = r_1 d\phi$. Finally, M_ϕ, M_θ and $M_{\phi\theta}$ are the bending moments (dimensions of force), while Q_θ and Q_ϕ transverse

forces per length that arise from bending theory. At equilibrium, the balance of all forces and moments yields the following six equations:

$$d\{r N_\phi\}/d\phi + r_1 d\{N_{\theta\phi}\}/d\theta - r_1 N_\theta \cos(\phi) - r Q_\phi = - r r_1 p_\phi , \quad (3.4.1a)$$

$$d\{r N_{\phi\theta}\}/d\phi + r_1 d\{N_\theta\}/d\theta + r_1 N_{\theta\phi} \cos(\phi) - r_1 Q_\theta \sin(\phi) = - r r_1 p_\theta , \quad (3.4.1b)$$

$$r_1 N_\theta \sin(\phi) + r N_\phi + r_1 dQ_\theta/d\theta + d\{r Q_\phi\}/d\phi = r r_1 p_r , \quad (3.4.1c)$$

$$d\{r M_\phi\}/d\phi + r_1 d\{M_{\theta\phi}\}/d\theta - r_1 M_\theta \cos(\phi) = r r_1 Q_\phi , \quad (3.4.1d)$$

$$d\{r M_{\phi\theta}\}/d\phi + r_1 d\{M_\theta\}/d\theta + r_1 M_{\theta\phi} \cos(\phi) = r r_1 Q_\theta , \quad (3.4.1e)$$

$$M_{\phi\theta} / r_1 - M_{\theta\phi} / r_2 = N_{\phi\theta} - N_{\theta\phi}. \quad (3.4.1f)$$

The current problem of interest, involves a determination of the equilibrium stresses and moments on cells subjected to external electric, and the final deformed geometry under steady-state conditions. Here, there is an inherent axial symmetry along the direction of the applied electric field, and the behavior along the two axes transverse to the applied electric field direction, will be identical. Such axial symmetry will hold for spherical cells at all times, and ellipsoidal (and other) shapes in the steady state after the cells have had the time to re-orient themselves in response to the external field [91]. A sketch of the applied field and the geometric cell model is shown in Fig. 5. There is an inner region, the cell membrane shell, and the outer region. Though a spherical geometry is shown for simplicity, the shapes could be different, in general, with the asymmetry perpendicular to the field direction. For such axisymmetric cases, the derivatives with respect to the angle θ drop out, while the shearing forces $N_{\phi\theta}$ and $N_{\theta\phi}$, the twisting moments $M_{\theta\phi}$ and $M_{\phi\theta}$, and the transverse shear Q_θ all vanish. Also, the load component p_θ is zero. Consequently, the following simpler set of equations result:

$$d\{r N_\phi\}/d\phi - r_1 N_\theta \cos(\phi) - r Q_\phi = - r r_1 p_\phi , \quad (3.4.2a)$$

$$r_1 N_\theta \sin(\phi) + r N_\phi + d\{r Q_\phi\}/d\phi = r r_1 p_r \,, \qquad (3.4.2b)$$

$$d\{r M_\phi\}/d\phi - r_1 M_\theta \cos(\phi) = r r_1 Q_\phi \,. \qquad (3.4.2c)$$

The above three equations contain five unknowns, and need to be supplemented by the stress-strain relationships. In the elastic regime, the stresses can be related to the displacements v (transverse) and w (normal) in the following manner [90]:

$$N_\phi = (12\,K/t^2)\,[\{dv/d\phi + w\}/r_1 + \nu\{v\cos(\phi) + w\sin(\phi)\}/r\,] \,, \qquad (3.4.3a)$$

$$N_\theta = (12\,K/t^2)\,[\{v\cos(\phi) + w\sin(\phi)\}/r + \nu\{dv/d\phi + w\}/r_1\,] \,, \qquad (3.4.3b)$$

$$M_\phi = (K/r_1)\,[d(\{dw/d\phi\}/r_1)/d\phi + \nu\{\,d[\cos(\phi)\{dw/d\phi\}/r]/d\phi\,\}] \,, \qquad (3.4.3c)$$

$$M_\theta = (K/r_1)\,[\cos(\phi)\{dw/d\phi\}/r] + \nu\, d(\{dw/d\phi\}/r_1)/d\phi\,] \,, \qquad (3.4.3d)$$

where K is the flexural rigidity (i.e. bending stiffness), ν the Poisson ratio, t the shell thickness assumed to be a constant, and w and v the displacements due to deformation along the radial and angular directions. Equations (3.4.3a)-(3.4.3d) involve the displacements w and v that constitute two additional unknowns of the problem. Thus, the combined set of equations 3.4.2(a)-(c) and 3.4.3(a)-(d) yield a system of seven equations for the seven unknowns that can be solved.

In general, a numerical computation is required for obtaining a solution to the above problem. However, analytical expressions can be obtained under certain simplifying conditions. For example, consider the case: $M_\phi \sim M_\theta \sim Q_\phi \sim 0$ which corresponds to neglecting the bending forces and moments as has been proposed in the past [92, 94]. Assuming that the external stresses arise solely from the Maxwell stress tensor associated with the applied external field (i.e. ignoring internal cell pressure and polarization effects), the stresses p_ϕ and p_r take the following form:

$$p_r = 0.5\,\varepsilon_o\,[k_{r1} - k_{r2}\,]\,E^2\cos(2\phi) \equiv F\cos(2\phi) \,, \qquad (3.4.4a)$$

$$\text{and, } p_\phi = -0.5\,\varepsilon_o\,[k_{r1} - k_{r2}]\,E^2\,\sin(2\phi) \equiv -F\sin(2\phi) \quad , \qquad (3.4.4b)$$

where E is the externally applied electric field, k_{r1} and k_{r2} the dielectric constants of the membrane and external medium, ε_o the permittivity of free space (= 8.85 x 10^{-12} F/m), and $F \equiv 0.5\,\varepsilon_o\,[k_{r1} - k_{r2}]\,E^2$. Using (4) in the equation set (2)-(3) yields the following simplifying solutions:

$$N_\phi(\phi) = [F / \{r_2 \sin^2(\phi)\}] \{ {}_0I^\phi\, r_1\, r_2\, [\cos(2\phi^*)\cos(\phi^*)\sin(\phi^*) + \sin(2\phi^*)\sin^2(\phi^*)]\, d\phi^* \}, \qquad (3.4.5a)$$

$$N_\theta(\phi) = r_2 F \cos(2\phi) - [r_2 / r_1]\, N_\phi \quad , \qquad (3.4.5b)$$

$$v(\phi) = {}_0I^\phi\, [q(\phi^*) / \sin(\phi^*)]\, d\phi^* \quad , \qquad (3.4.5c)$$

$$\text{where } q(\phi) \equiv \{t^2/[12\,K\,(1-\nu^2)]\} \{ r_1\,[N_\phi(\phi) - \nu N_\theta(\phi)] - r_2\,[N_\theta(\phi) - \nu N_\phi(\phi)] \}, \qquad (3.4.5d)$$

$$\text{and, } w(\phi) = r_2 \{t^2/[12\,K\,(1-\nu^2)]\}\,[N_\theta(\phi) - \nu N_\phi(\phi)] - v(\phi)\cot(\phi) \; . \qquad (3.4.5e)$$

For an initial spherical shape, $r_1 = r_2$ = the radius "a", and the above simplifies to:

$$N_\phi(\phi) = 0.5\,a\,F \; ; \quad N_\theta(\phi) = a\,F\,[0.5 - 2\sin^2(\phi)] \quad , \qquad (3.4.6a)$$

$$v(\phi) = -\{F\,a^2\,t^2/[12\,K\,(1-\nu)]\}\,\sin(2\phi) \quad , \qquad (3.4.6b)$$

$$\text{and, } w(\phi) = \{F\,a^2\,t^2/[12\,K\,(1-\nu^2)]\}\,[0.5 - 2\sin^2(\phi) - \nu/2 + 2\,(1+\nu)\cos^2(\phi)] \quad . \qquad (3.4.6c)$$

For an ellipsoidal shape with "*a*" being the semi-major axis along the field direction, and "*b*" the semi-minor axes in the two transverse directions (as has often been used in the literature), r_1 and r_2 take on the following expressions:

$$r_1 = (a^2/b)\,[\{1 + \tan^2(\phi)\}/\{a^2/b^2 + \tan^2(\phi)\}]^{1.5} \quad , \qquad (3.4.7a)$$

$$\text{and, } r_2 = \{b / \cos(\phi)\}\,[a^2/b^2 + \tan^2(\phi)]^{-0.5} \quad . \qquad (3.4.7b)$$

Using 3.4.7(a)-3.4.7(b) into the equation set 3.4.5(a) - 3.4.5(e) then yields the complete solution for the ellipsoidal geometry. These equations have been used to predict cell deformations, and the results will be discussed in the next chapter.

3.4.2 Electrical Field Analysis

In the above formulae, polarization effects were not considered and so the field was taken to equal the external electric field E given in terms of the factor F of equation (3.4.4a). However, given the presence of the cell and its membrane, which are both polarizable materials, one needs to solve the Laplace equation to self-consistently determine the electric field value and its spatial characteristics for assessing the Maxwell stress tensor. Also, the trans-membrane voltages given in section 3.2.3 are only valid for a simple spherical geometry. Due to possible deformation, the cell shape could deviate from a pure spherical form, and the trans-membrane potential magnitudes would then be affected. Here, this aspect is discussed, and a mathematical treatment of the membrane potentials for non-spherical shapes derived.

We first start with a simple spherical cell geometry as given in the schematic of Fig. 5. Both the spherical and ellipsoidal geometries lend themselves to analytical solutions, and hence, are chosen here as typical examples. Other simple geometries can also be analyzed numerically. The inner region has radius "*a*" and permittivity ε_{in}. The applied electric field F_0 was taken to be along the z-axis. The cellular membrane of Fig.5 has a thickness "*b-a*" = "*t*" and permittivity ε_{mem}, while the outer suspension region a permittivity of ε_{out}. Due to azimuthal symmetry, the potentials in the three regions, which must satisfy the Laplace equation, can be expressed in terms of Legendre polynomials as:

$$U_{in}\ (r) = A_0 P_0 + A_1 r P_1 + A_2 r^2 P_2 + \ldots = \Sigma_{j=0,\infty} A_j r^j P_j \ , \qquad (3.4.8a)$$

$$U_{mem}\ (r) = \Sigma_{j=0,\infty} [\, B_j r^j P_j + C_j P_j / r^{j+1} \,] \ , \qquad (3.4.8b)$$

$$and\ \ U_{out}\ (r) = - F_0 r P_1 + \Sigma_{j=0,\infty} D_j P_j / r^{j+1} \ , \qquad (3.4.8c)$$

where $U_{in}(r)$, $U_{mem}(r)$, and $U_{out}(r)$ are the potentials at the inside, membrane and outer regions, P_j is the j^{th} order Legendre polynomial, and F_0 the externally applied electric field. Also, A_j , B_j , C_j , and D_j are the coefficients of the Legendre series expansions that can be determined by applying matching boundary conditions at the interfaces of the three regions. Invoking continuity in the potential and displacement vector, then leads to the following boundary conditions:

$$U_{in}\ (r = a) = U_{mem}\ (r = a) \ , \qquad (3.4.9a)$$

$$U_{mem}\ (r = b) = U_{out}\ (r = b) \ , \qquad (3.4.9b)$$

$$\varepsilon_{in} [\, MU_{in}\ (r)/Mr \,] \mid_{r=a} = \varepsilon_{mem} [\, MU_{mem}\ (r)/Mr \,] \mid_{r=a} \ , \qquad (3.4.9c)$$

$$\text{and}, \quad \varepsilon_{mem} [\, MU_{mem}\ (r)/Mr \,] \mid_{r=b} = \varepsilon_{out} [\, MU_{out}\ (r)/Mr \,] \mid_{r=b} \ . \qquad (3.4.9d)$$

Straightforward, but tedious manipulation of the (3.4.9) yields the following expressions for the potentials:

$$U_{in}\ (r) = C_1\ (r/a^3)\ cos(\phi)\ [1 + \{2\varepsilon_{mem} + \varepsilon_i\}/\{\varepsilon_{mem} - \varepsilon_{in}\}] \ , \qquad (3.4.10a)$$

$$U_{mem}\ (r) = C_1\ cos(\phi)\ [1/r^2 + (r/a^3)\ \{2\varepsilon_{mem} + \varepsilon_i\}/\{\varepsilon_{mem} - \varepsilon_{in}\}] \ , \qquad (3.4.10b)$$

$$U_{out}\ (r) = - F_0\ cos(\phi)\ [r\ ?^3/r^2] + \{C_1/r^2\} cos(\phi)\ [1 + (b/a)^3\ \{2\varepsilon_{mem} + \varepsilon_{in}\}/\{\varepsilon_{mem} - \varepsilon_{in}\}] \ , \qquad (3.4.10c)$$

$$\text{where,}\ \ C_1 = - 3F_0\ \varepsilon_{out} / [\{T\ \varepsilon_{mem}/a^3\} - 2\varepsilon_{mem}/b^3 + \{2\varepsilon_{out}/b^3\}[1 + (b/a)^3\ T] \ , \qquad (3.4.10d)$$

$$\text{and,}\ \ T = \{2\varepsilon_{mem} + \varepsilon_{in}\}/\{\varepsilon_{mem} - \varepsilon_{in}\} \ . \qquad (3.4.10e)$$

Consequently, the electric fields $F_r(r)$ and $F_\phi(r)$ just outside the membrane (i.e. at $r = b_+$) are given as:

$$F_r(r=b) = [3F_0 + 2(C_1/b^3)\{1 + (b/a)^3 T\}]\cos(\phi) \equiv \iota_r \cos(\phi), \quad (3.4.10f)$$

$$F_\phi(r=b) = \{C_1/b^3\}\sin(\phi)[1 + (b/a)^3 T] \equiv \iota_\phi \sin(\phi) . \quad (3.4.10g)$$

For $\varepsilon_{in} = \varepsilon_{mem} = \varepsilon_{out}$, the above equations reduce to: $U(r) = -F_0 r \cos(\phi)$, $F_r(r) = F_0 \cos(\phi)$, and $F_\phi(r) = -F_0 \sin(\phi)$.

While both $F_r(r=b)$ and $F_\phi(r=b)$ retain the $\cos(\phi)$ and $\sin(\phi)$ angular dependence, respectively, their magnitudes (i.e. ι_r and ι_ϕ) are altered by the presence of dielectric materials. The resultant field |F| is no longer along the z-axis (i.e. not at an angle ϕ with respect to the normal). Instead, $|F| = [\iota_r^2 \cos^2(\phi) + \iota_\phi^2 \sin^2(\phi)]^{0.5}$, while the angle α between the resultant field |F| and the normal becomes: $\alpha = \tan^{-1}[-\tan(\phi)\ \iota_\phi/\iota_r]$. Consequently, the expressions in equations (3.4.4) get modified to the form: $p_r = 0.5\ \varepsilon_o [k_{r1} - k_{r2}] |F|^2 \cos(2\alpha) \equiv F^* \cos(2\alpha)$, and $p_\phi = -0.5\ \varepsilon_o [k_{r1} - k_{r2}] |F|^2 \sin(2\alpha) \equiv -F^* \sin(2\alpha)$. Under these conditions, equations (3.4.5a-3.4.5b) correspondingly change to:

$$N_\phi(\phi) = [F^*/\{r_2 \sin^2(\phi)\}]\{ {}_0I^\phi r_1 r_2 [\cos(2\alpha^*)\cos(\phi^*)\sin(\phi^*) + \sin(2\alpha)\sin^2(\phi^*)]\, d\phi^* \} , \quad (3.4.11a)$$

$$N_\theta(\phi) = r_2 F^* \cos(2\alpha) - [r_2/r_1] N_\phi , \quad \text{where } \alpha^* = \tan^{-1}[-\tan(\phi^*)\ \iota_\phi/\iota_r] . \quad (3.4.11b)$$

For an ellipsoidal geometry, the Laplace equation is most easily solved by resorting to the ellipsoidal co-ordinate system. Many cells under deformation are known to approximate the ellipsoidal geometry. We assume a prolate spheroid without loss in generality, with semi-major axis "a", semi-minor axes "b" and center at the origin. The foci are taken to be along the z-direction (parallel to the applied E-field) at (0, 0, $\pm$L) with $L = [a^2 - b^2]^{0.5}$. The eccentricity "e" then is given by: $e = L/a$. The co-ordinates ς, η, ϕ

for this system are defined in the usual manner [95] with respect to the Cartesian co-ordinates as:

$$z = L\,\varsigma\,\eta\ ;\ y = L\,[\{\varsigma^2-1\}\{1-\eta^2\}]^{0.5}\sin(\theta)\ ;\ x = L\,[\{\varsigma^2-1\}\{1-\eta^2\}]^{0.5}\cos(\theta)\ , \qquad (3.4.12\text{ a})$$

$$\text{i.e. } \varsigma = [\{x^2+y^2+(z+L)^2\}^{0.5} + \{x^2+y^2+(z-L)^2\}^{0.5}]/(2L)\ ;\ \theta = \tan^{-1}(y/x)\ ;$$

$$\text{and } \eta = [\{x^2+y^2+(z+L)^2\}^{0.5} - \{x^2+y^2+(z-L)^2\}^{0.5}]/(2L)\ . \qquad (3.4.12\text{ b})$$

The ellipsoidal surface then corresponds to a constant ς value given by: $\varsigma \equiv \varsigma_o = a/L$.

Due to angular symmetry, the potentials in the three regions can be written as:

$$U_{out}(\varsigma,\eta) = -F_0 L\,\varsigma\,\eta + A\,\varsigma Q(\varsigma)\ ,\ U_{mem}(\varsigma,\eta) = -B F_0 L\,\varsigma\,\eta + C\,\varsigma Q(\varsigma)\ , \qquad (3.4.13\text{a})$$

$$U_{in}(\varsigma,\eta) = D F_0 L\,\varsigma\,\eta,\ \text{with}\ Q(\varsigma) = 0.5\,\varsigma Ln|(1+\varsigma)/(1-\varsigma)| - 1\ , \qquad (3.4.13\text{b})$$

where A, B and C are constants to be determined from the boundary conditions. Using the continuity of the potential and displacement vector across the inner and outer membrane (assumed to have constant thickness, "t"), results in the following solution:

$$U_{out}(\varsigma,\eta) = -F_0 L\,\varsigma\,\eta + A\,\varsigma Q(\varsigma)\ , \qquad (3.4.14\text{a})$$

$$U_{mem}(\varsigma,\eta) = A\eta\,[\varsigma\,Q(\varsigma_o)/\varsigma_o + (S_1/S_2)\{Q(\varsigma_o)/\varsigma_o - \{dQ(\varsigma_o)/d\varsigma\}(\varepsilon_{out}/\varepsilon_{mem})\}] +$$

$$+ F_0 L\,\eta\,[(S_1/S_2)(\varepsilon_{out}/\varepsilon_{mem}-1) - \varsigma]\ , \qquad (3.4.14\text{b})$$

$$\text{with, } S_1 = Q(\varsigma) - \varsigma\,Q(\varsigma_o)/\varsigma_o\ ,\ S_2 = Q(\varsigma_o)/\varsigma_o - dQ(\varsigma_o)/d\varsigma\ , \qquad (3.4.14\text{c})$$

$$U_{in}(\varsigma,\eta) = A\eta\varsigma\,[Q(\varsigma_o)/\varsigma_o + (S_3/S_2)\{Q(\varsigma_o)/\varsigma_o - \{dQ(\varsigma_o)/d\varsigma\}(\varepsilon_{out}/\varepsilon_{mem})\}] +$$

$$+ F_0 L\,\varsigma\,\eta\,[(S_3/S_2)(\varepsilon_{out}/\varepsilon_{mem}-1) - 1]\ , \qquad (3.4.14\text{d})$$

$$\text{with, } S_3 = Q(\varsigma_1)/\varsigma_1 - Q(\varsigma_o)/\varsigma_o\ ,\ \varsigma_1 \cong \varsigma_o\,[1 - t\,b/\{a(a+b)\}]\ . \qquad (3.4.14\text{e})$$

In the above, $\varsigma = \varsigma_1$ represents the surface of the inner membrane, while the constant "A" is as:

$$A = \frac{F_0 L[S_2(\varepsilon_{in} - \varepsilon_{mem}) + S_4(\varepsilon_{out} - \varepsilon_{mem}) - \varepsilon_{in} S_3(\varepsilon_{out}/\varepsilon_{mem} - 1)]}{S_2(\varepsilon_{in} - \varepsilon_{mem})Q(\varsigma_0)/\varsigma_0 + (\varepsilon_{in} S_3 - \varepsilon_{mem} S_4)\{Q(\varsigma_0)/\varsigma_0 - \varepsilon_{out}/\varepsilon_{mem} dQ(\varsigma_0)/\varsigma\}}$$

where, $S_4 = dQ(\varsigma_1)/d\varsigma - Q(\varsigma_o)/\varsigma_o$. (3.4.14f)

The electric field normal to the outer ellipsoidal surface is $F_\varsigma(\varsigma, \eta)$, while $F_\eta(\varsigma, \eta)$ is orthogonal to F_ς and lies in planes containing the z-axis. Expressions for these fields from equations (3.4.13) are:

$$F_\varsigma(\varsigma_o, \eta) = [(\varsigma_0^2 - 1)/(\varsigma_0^2 - \eta^2)]^{0.5} [F_0\eta - (A/L)(Q(\varsigma_o) + \varsigma_0 dQ(\varsigma_o)/d\varsigma)] , \quad (3.4.15a)$$

$$F_\eta(\varsigma_o, \eta) = [(1-\eta^2)/(\varsigma_0^2 - \eta^2)]^{0.5} [F_0 \varsigma_0 - A\, Q(\varsigma_o)/L] . \quad (3.4.15b)$$

For a spherical geometry, a → b, and so L → 0, ς_o → 4 yielding $F_\varsigma = F_0 \cos(\phi)$, and $F_\eta = -F_0 \sin(\phi)$.

3.5 Time Dependent Transmembrane Potential Calculation Model

3.5.1 Introduction

Analysis of the cellular response to electrical pulses requires, at the very least, an evaluation of the voltage and current distributions within the cell, and their time dependent evolution. This potential is the source for pore opening and cellular responses. A possible approach for modeling the overall spatial behavior might be to represent the electrical characteristics of cells by a distributed equivalent circuit. However, time-domain, circuit-solvers such as SPICE are not suited to the present problem for the following reasons: (i) In SPICE, values of circuit parameters (e.g. resistors R, capacitors C, etc.) cannot be made time dependent, (ii) The stochastic nature of pore formation cannot be included, (iii) the geometric dependence of R and C make it inconvenient to run simulations with varying shapes and sizes, (iv) soft-thresholds inherent in the pore formation process are difficult to implement, and (v) it is difficult to use circuit models to

simulate the gradual resealing of pores. The resealing process always takes long times (~ms), and the long-lived, diffusion-driven currents cannot be modeled by circuit simulators.

In this research, time dependent calculations of potentials and current flows throughout the cell have been carried out based on a distributed electrical model. An approach to such calculations is through a time-domain nodal analysis involving a distributed equivalent circuit representation of a cell and its membrane structures. Details of this distributed, time-dependent model, along with its implementation are discussed next.

3.5.2 Model Details

The entire cell was broken up into segments, and each segment represented by a parallel *RC* combination. Azimuthal symmetry was used to map the three-dimensional structure into the r and φ co-ordinates of a spherical system. This method is different from the Legendre polynomial model we used in the electrostatic case discussed in section 3.1. Time-dependent changes in the local conductivity can be implemented via this approach. The previous methods outlined in sections 3.2.3 and 3.4.2 are more suited for solutions of the static Laplace equation. Time dependent transmembrane potential can be obtained by using this new model. Coupling this model with Smoluchowski equation (SE) based electroporation model, dynamic simulation of the cell system can be achieved. Volume and shape changes of cells are ignored because the external applied pulse is too short (nanosecond time frame) for cells to deform during this short time interval.

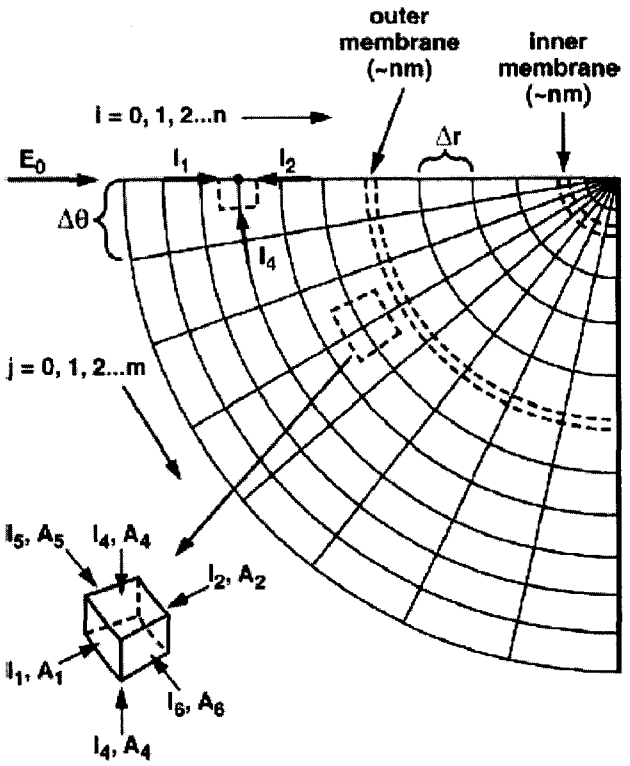

Fig. 7 Schematic of one quarter of the model used to represent a cell for the distributed electrical calculations. The dotted box shows a typical element with current flows.

In our simulation, the computation region is also sphere, which includes environment suspension medium, cell and its substructures. It is discretized in r and θ direction as shown in Fig.7. For simplicity, only a quarter of the computation region is considered. For simplicity, membranes are taken as an integrate unit, that is, it is not discretized. For each element, the following equation holds due to the current continuity.

$$\nabla \bullet (J + \frac{\partial D}{\partial t}) = 0 \qquad , \tag{3.5.1}$$

where J is the current density and D is the electric displacement. By using Stokes theorem, this can be transformed as:

$$\iiint \nabla \bullet (J + \frac{\partial D}{\partial t}) = \oiint J + \frac{\partial D}{\partial t} = \oiint \sigma E + \varepsilon \frac{\partial E}{\partial t} = 0 \quad . \tag{3.5.2}$$

Here E is the electric field, σ is the conductivity and ε the permittivity.

Eqn. (3.5.2) is applicable to all nodes with index in the range: 0<i<n and 0<j<m. In discretized form, Eqn. (3.5.2) then can be written as:

$$\sum_{k=1}^{6} (\sigma E + \varepsilon \frac{\partial E}{\partial t})_k \times A_k = \sum_{k=1}^{6} I_k = 0 \quad , \tag{3.5.3}$$

where I_5 and I_6 are along the ϕ direction, but along the ϕ-direction all nodes are an equi-potential due the geometric symmetry of the computational region. Hence, $I_5 = I_6 = 0$. Consequently, we obtain:

$$\begin{aligned} &\sigma_1 \frac{V^t_{i-1,j} - V^t_{i,j}}{\Delta r} A_1 + \sigma_2 \frac{V^t_{i+1,j} - V^t_{i,j}}{\Delta r} A_2 + \sigma_3 \frac{V^t_{i,j-1} - V^t_{i,j}}{r\Delta\theta} A_3 + \sigma_4 \frac{V^t_{i,j+1} - V^t_{i,j}}{r\Delta\theta} A_4 + \\ &\frac{\varepsilon_1}{\Delta t}[\frac{V^{t+1}_{i-1,j} - V^{t+1}_{i,j}}{\Delta r} - \frac{V^t_{i-1,j} - V^t_{i,j}}{\Delta r}]A_1 + \frac{\varepsilon_2}{\Delta t}[\frac{V^{t+1}_{i+1,j} - V^{t+1}_{i,j}}{\Delta r} - \frac{V^t_{i+1,j} - V^t_{i,j}}{\Delta r}]A_2 + \\ &\frac{\varepsilon_3}{\Delta t}[\frac{V^{t+1}_{i,j-1} - V^{t+1}_{i,j}}{r\Delta\theta} - \frac{V^t_{i,j-1} - V^t_{i,j}}{r\Delta\theta}]A_3 + \frac{\varepsilon_4}{\Delta t}[\frac{V^{t+1}_{i,j+1} - V^{t+1}_{i,j}}{r\Delta\theta} - \frac{V^t_{i,j+1} - V^t_{i,j}}{r\Delta\theta}]A_4 = 0 \end{aligned} \quad . \tag{3.5.4}$$

In the above, $V^t_{i,j}$ stands for the potential at node (i, j) at time t. r is radial distance between node (i, j) and node (n, m). A_1 to A_4 are the areas shown in Fig. 7. σ_1 to σ_4 are conductivities at location of face 1 to 4 respectively, and ε_1 to ε_4 are permittivities at corresponding location. For instance, if the studied node is in the environment medium area, which means the medium around it is the same; all σs will be the same. But if the studied node is on the membrane, σ_1 will be different from σ_2. The same situation occurs to permittivity. So the nodes on the membrane will be treated differently than those nodes in isotropic medium. Some more details are provided in the Appendix.

In order to reduce the computation load, special boundary conditions are applied so that only a quarter of the whole spherical computation region is under study due to the symmetry. For those nodes which has $j = 0$ and $j = m$ should be treated carefully. Only I_1, I_2 and I_4 are nonzero because the targeted element only has 5 faces due to that face 3 shrinks to a line. So when j = 0 and $0 < i < n$, Eqn. (3.5.4) would be changed to:

$$\begin{aligned}
&\sigma_1 \frac{V^t_{i-1,j} - V^t_{i,j}}{\Delta r}(r + \Delta r/2)^2(\cos\theta - \cos(\theta + \Delta\theta/2)) + \\
&\sigma_2 \frac{V^t_{i+1,j} - V^t_{i,j}}{\Delta r}(r - \Delta r/2)^2(\cos\theta - \cos(\theta + \Delta\theta/2)) + \\
&\sigma_4 \frac{V^t_{i,j+1} - V^t_{i,j}}{r\Delta\theta} r\Delta r \sin(\theta + d\theta/2) + \\
&\frac{\varepsilon_1}{\Delta t}\left[\frac{V^{t+1}_{i-1,j} - V^{t+1}_{i,j}}{\Delta r} - \frac{V^t_{i-1,j} - V^t_{i,j}}{\Delta r}\right](r + \Delta r/2)^2(-1 - \cos(\theta + \Delta\theta/2)) + \\
&\frac{\varepsilon_2}{\Delta t}\left[\frac{V^{t+1}_{i+1,j} - V^{t+1}_{i,j}}{\Delta r} - \frac{V^t_{i+1,j} - V^t_{i,j}}{\Delta r}\right](r - \Delta r/2)^2(-1 - \cos(\theta + \Delta\theta/2)) + \\
&\frac{\varepsilon_4}{\Delta t}\left[\frac{V^{t+1}_{i,j+1} - V^{t+1}_{i,j}}{r\Delta\theta} - \frac{V^t_{i,j+1} - V^t_{i,j}}{r\Delta\theta}\right] r\Delta r \sin(\theta + \Delta\theta/2) = 0
\end{aligned} \quad . \tag{3.5.5}$$

Here $\theta = \pi + j \times \Delta\theta = \pi$ and $\Delta\theta$ is $\frac{\pi}{2}/m$.

We assume without loss in generality that the electrical field is applied along the z direction as shown in Fig.7 and potential at node with $i = n$ is zero, i.e.,

$$V_{n,j} = 0 \ . \tag{3.5.6}$$

Potential of the nodes with index $j = 0$ are equipotentials. Hence,

$$V_{i,m} = V_{n,j} = 0 \tag{3.5.7}$$

Another boundary condition should be considered is for those nodes with index $i = 0$. Then the potentials of those nodes with index $i = 0$ are calculated by :

$$V_{0,j} = -E_0 R\cos\theta \ , \quad \text{j} = 0...\text{m}. \tag{3.5.8}$$

In the above E_0 is applied electrical field, and R is the radius of the computation region. Thus, combining with the boundary conditions discussed above, one can get N equations from N nodes for N unknowns. These N equations can be solved easily by turning it into an $Ax = B$ problem. Here A is a sparse coefficient matrix, x is the potential vector of next time step, and B is a vector obtained from known parameters. Potential on each node is easily to be updated as time goes by. Boundary conditions are applied on those nodes with index i = 0. Detailed equations are shown in Appendix.

As discussed in section 3.1, if the dynamic pore area is considered, the effective conductivity of membrane $\sigma_{eff\_mem}(t)$ can be calculated by:

$$\sigma_{eff\_mem}(t) = \frac{A_P(r,t)}{A_0}\sigma_{out} + (1 - \frac{A_P(r,t)}{A_0})\sigma_{mem} \tag{3.5.9}$$

Here σ_{out} is the conductivity of the medium outside the membrane and σ_{mem} is the conductivity of membrane before electroporation. Thus, the SE yields the pore distribution and dynamic pore area, which in turn affects the electrical parameters. This is coupled to the distributed electrical analysis for self-consistency through dynamic variations of resistance R and capacitance C.

3.6 The Simplified Ball-Spring, Many-Body Approach

3.6.1 Introduction

All of the models discussed above have been based on either lumped or distributed representation of the cells at a fairly macroscopic level. Thus, the role of individual molecules and the inherent microscopic interactions were ignored. In stead, macroscopic parameters (such as the surface tension) were assumed to adequately model

the cellular details. In reality, however, much of the dynamics and cell response can be expected to depend on the details of the molecular interactions. A more bio-chemical approach, rather than a coarser electrical model is perhaps necessary.

Here in this research, we have attempted to go beyond a simple macroscopic model, and to include the molecular aspects for a more accurate picture. For example, one of the most basic features of the bio-membrane is the lipid bilayer consisting of a hydrophobic (viewed as being "oily") hydrocarbon tail attached to a larger hydrophilic head group. These amphiphilic molecules arrange themselves to shield their "oily" tails from the aqueous environment. The bilayer membrane is relatively flexible, allowing for in-plane diffusion and possible shape change. Such structural details cannot be incorporated into macroscopic models.

In the literature, phenomenological models for describing the mesoscopic behavior of membranes have been developed [96, 98]. However, these do not allow for the inclusion of molecular details. At the other extreme of computational complexity, there are full atomistic models capable of including all of the microscopic details [99, 102]. A reasonable trade-off is to keep the atomic perspective, while course-graining each lipid molecule into a smaller effective chain with far fewer constituent atoms. Obviously, during such a process, physical properties such the hydrophobic tails and the hydrophilic interactions of the lipid head need to be preserved. Such an approach has recently been used [103, 106], and the lipid reduced to about 10 atoms or less. Here, we use a course-grained approach to implement a molecular dynamics simulation of membrane response to an external electric field in the presence of an ionized aqueous medium.

3.6.2 Model Details

This section presents the details of our microscopic model and its implementation. Specifically, the focus here is on cell membranes since most of the biophysical phenomena are expected to occur at the region because the electric field is the largest. At the molecular level, the membrane consists of a bilayer of lipid proteins.

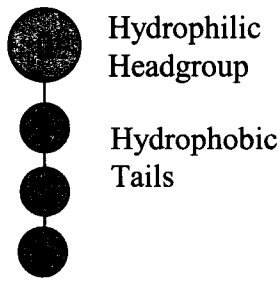

Fig. 8 Sketch of the ball-spring model. Ball "0" represents the hydrophilic head-group, and balls 1,2 and 3 the hydrocarbon tail.

The lipids in our model consist of four spherical atoms interconnected by a non-linear spring as shown in Fig. 8. Particle "0" is the hydrophilic head, while particles "1", "2" and "3" represent the oily, hydrophobic tail. The dipole at the lipid head (e.g. as in phosphatidylcholine lipid molecule), has been ignored because of a very low dipole moment, and also since electrostatic interaction with closely spaced dipoles is minimal. The two types of particles (water-like and oil-like) are taken into account, with interactions based on a truncated and shifted Lennard-Jones (L-J) potential $\phi_{ij}(r)$ given as:

$$\phi_{ij}(r) = 4\varepsilon_{ij}[(\frac{\sigma_{ij}}{r})^{12} - (\frac{\sigma_{ij}}{r})^{6} - (\frac{\sigma_{ij}}{R_{ij}^{c}})^{12} + (\frac{\sigma_{ij}}{R_{ij}^{c}})^{6}] \quad , \tag{3.6.1}$$

where i,j stand for the i^{th} and j^{th} particles, ε_{ij} is the energy parameter, σ_{ij} represents the distance parameter, and R^{c}_{ij} the cut-off radius. Here a constant distance parameter $\sigma_{ij} = \sigma$ was chosen, with a cut-off radius $R^{c}_{ij} = 2.5\sigma$ used for like particles, and $R^{c}_{ij} = 2^{1/6}\sigma$ for

Table 2 Parameters used in LJ force calculations.

	σ_{ij} (nm)	ε_{ij} (kJ/mol)
Head(pc)-head(pc)	0.70	2.6
Head(pc)-head(ps)	0.65	2.6
Head-tail1	0.55	2.0
Head-tail2	0.70	2.0
Head-tail3	0.90	2.0
Tail-tail	0.40	2.0
Water-water	0.32	0.65 [108]
Water-head(pc)	0.50	2.0
Water-head(ps)	0.45	2.0
Water-tail	0.40	2.0
Ion-ion	0.39	2.13 [108]
Ion-water	0.35	2.0
Ion-head(pc)	0.50	2.0
Ion-head(ps)	0.45	2.0
Ion-tail	0.40	2.0

two unlike particles. The complete set of L-J parameters for this ball-spring model is given in Tables 2 and 3. The L-J potentials between head and tails for this parameter set are plotted in Fig. 9 as a function of the normalized distance. Other pair potentials for the tail-tail interactions can similarly be calculated. The parameters were chosen to make lipid chains flexible enough to display a "kink", yet not so soft that the lipid chains might form a U-shaped structure. The head and tail balls are connected by a non-linear spring, with an anharmonic energy given by [107]:

$$U(r_{ij}) = -0.5kR_{ij}\ln[1-(\frac{r_{ij}}{R_{ij}})^2]) \quad . \qquad (3.6.2)$$

In the above, $R_{ij} = 1.5\sigma$, and k is the spring constant taken to be 3×10^{-9} N, and r_{ij} the distance between the two balls connected by the spring. Defined in this way, the spring is finite-extendable, which well describes the property of a chemical bond. The parameters

given in Tables 2 and 3 were carefully chosen through trial and error to avoid the crossing of molecular chains in our model.

Table 3 Parameters used in the ball-spring model.

Radius of headgroups of lipid r_H	0.35nm
Radius of oil like tail of lipid r_T	0.2nm
Radius of water molecules r_W	0.15nm
Distance between any neighbor two balls in a lipid chain (resting state)	$r_1 + r_2 + 0.2$nm
Anharmonic spring constant	3×10^{-9} N
Simulation time step	1×10^{-15} s

Water molecules were treated in terms of the rigid SPC/E model, which consists of three partial charges located on the oxygen and hydrogen sites [109]. Ions are also treated in terms of the rigid SPC/E model. The LJ parameters for the water-water, lipid-water, ion-water and ion-ion interactions are also given in Table 2. Force on the water dipoles was taken to arise from the Coulomb interactions of the simulation ions present in the aqueous medium. Consequently, only the water molecules in close proximity to ions were subject to a non-negligible force. In actuality, the presence of charged lipids (such as phosphotidyl-serine on the inner membrane leaflet) can be expected to contribute to the spatial non-uniformity, and hence, to an additional force on the water dipoles. Here for simplicity, the external electric field was assumed to be spatially uniform, and inhomogeneities associated with electrode geometry and curvature, or due to non-uniform distribution of charged lipid molecules were all ignored.

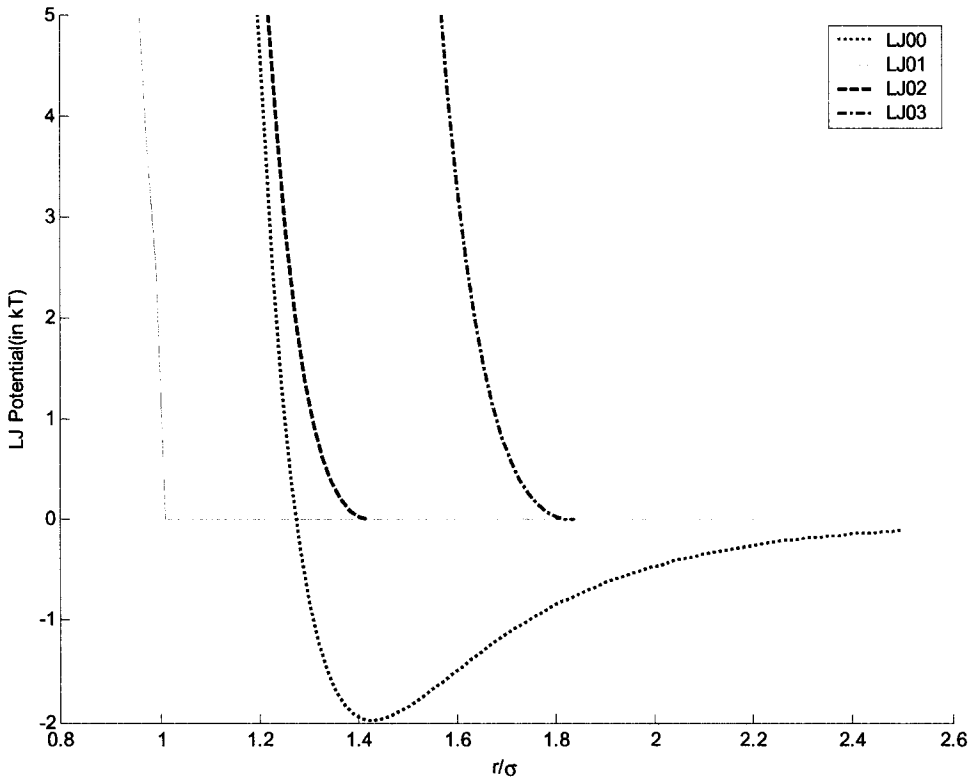

Fig. 9 L-J potentials versus normalized distance between the head and tail spheres comprising the lipid chain. Here "0" stands for the head, and "1", "2" and "3" are the tail balls.

For the membrane simulations, our simulation system basically contained 40 lipid chains and 400 movable water molecules. Thus, only a small segment of the lipid membrane was studied. The ratio of water-to-lipid molecules was taken to be about 10, which is large enough to describe the system combined within the water boundary. Each lipid chain had one head ball and three tail spheres. The simulation time step was 1fs, which was found to be the maximum time step that could yield stable results. In order to reduce finite segment effects, periodic boundary conditions (PBC) were applied to the lipid chains and the water molecules. This helps maintain the system pressure and the overall lipid density. Due to the PBC being applied to the water molecules, the top and

bottom boundaries of the simulation box were not rigid, though the total volume was maintained on average. For simulations in the presence of an external electric field, the velocity of lipid chains and water molecules was scaled down every 20-simulation step to maintain a constant temperature. This mimics an implementation of the Berendsen thermal bath [110].

These types of simulations were carried out on a PC workstation with Pentium IV 2.88MHz CPU. One nanosecond of real time simulation took about 6.8 hours. The simulation region was 18nm×8.7nm. The average membrane thickness was 5nm.

3.6.3 Simple Model Validation

A requirement of this simple atomic course-grained model for the lipid molecules is to preserve the important property of hydrophobic and hydrophilic behaviors. As a simple test of this, individual head and tail particles were placed into a simulation region to mimic an "oil droplets in water" scenario, as shown in Fig. 10 with no external electrical field. Initially the particles are randomly located, and every movable particle assigned a random velocity, chosen statistically from a thermal Boltzmann distribution at room temperature. The "Water-like" hydrophilic particles at the boundaries on each side were held fixed to provide hard-wall conditions and maintain a fixed volume. However, L-J potentials between the boundary molecules and the moveable particles were taken into account. After 1×10^6 simulation steps, a dynamic, steady state was observed, as shown in Fig. 11. The hydrophobic particles are seen to cluster together eventually, and repel any hydrophilic particle whose trajectory might take it through the cluster. A number of different starting configurations (not shown) were also tried, but the same

general trends were always observed. The results thus qualitatively validate our simple atomistic implementation of the hydrophobic and hydrophilic interactions.

Another important feature of ion transport in an aqueous medium is the formation of a cluster of water molecules around an ion due to dipole orientation effects. Normally a charged ion is symmetrically surrounded by water dipoles. The application of an extremely high external field might cause the water dipoles to align. The interaction with dipoles located in front of the moving ion, would tend to draw the water molecules closer, forming a cloud around the ion. For extremely high electric fields, the water molecules behind a moving ion would tend to be repelled, forming a localized "Hole". However, for the electric fields considered here, such a spatial hole did not result. The primary effect was an assembly of water molecules. This water cloud is expected to be dragged along by the drifting ions as they travel and arrive at membrane surfaces. For validation of the above, simulation were carried out based on our L-J, ball-spring implementation with inclusion of the Coulomb interactions. A generic radius of 0.4 nm typical of many ions was chosen, and all particles were randomly assigned velocities based on a thermalized Maxwellian. The distribution in Fig. 12(a) shows the initial starting configuration in the presence of a 100 kV/cm external electric field. The spatial distribution at a later time is shown in Fig. 12(b). The water-clustering feature discussed above is clearly seen, and demonstrates the successful incorporation of basic physical mechanisms into the model. Fig. 12(c) shows that the ion with water cloud moves in the direction of external electrical field.

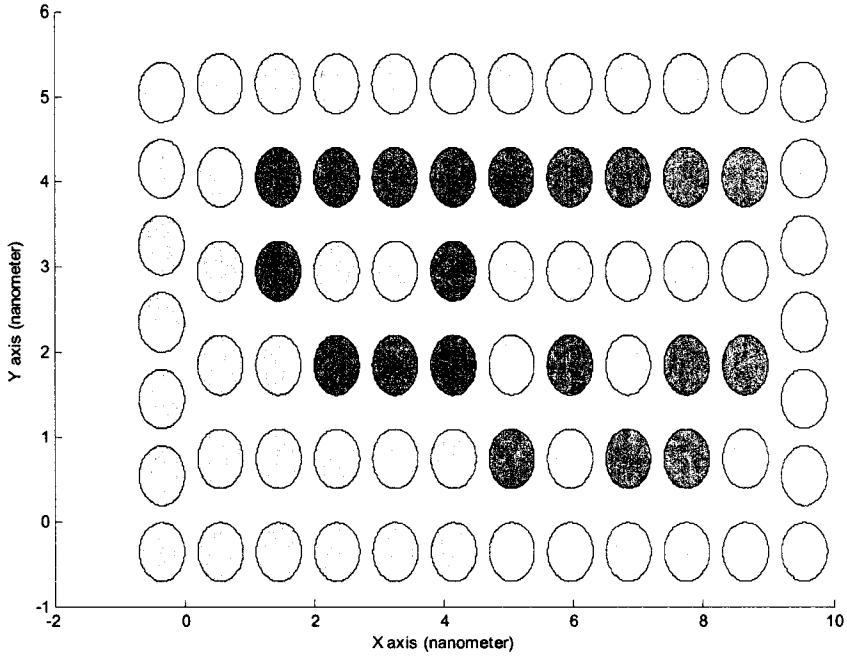

Fig. 10 Initial random distribution of hydrophobic (red) and hydrophilic (blue) particles in a finite simulation box with hard-walls.

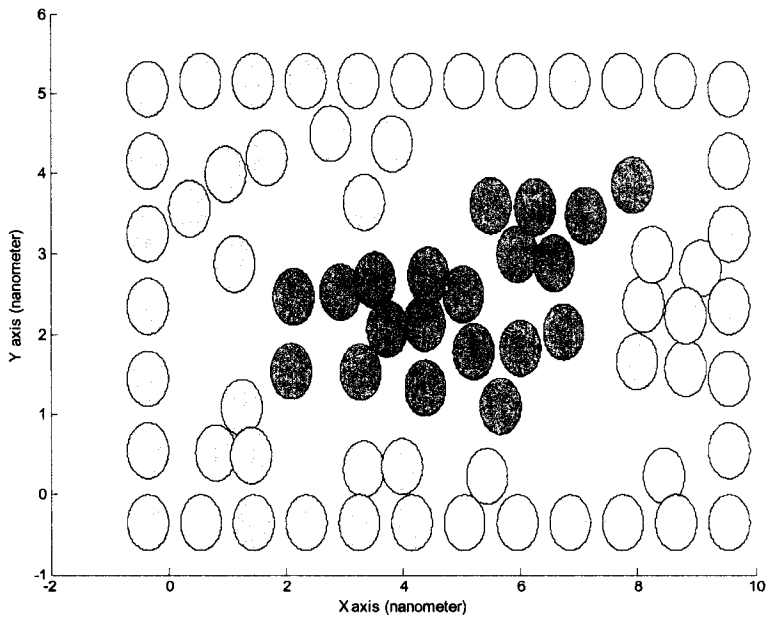

Fig. 11 Distribution of the particles in the dynamic steady state showing the hydrophobic spheres clustering together away from the hydrophilic particles.

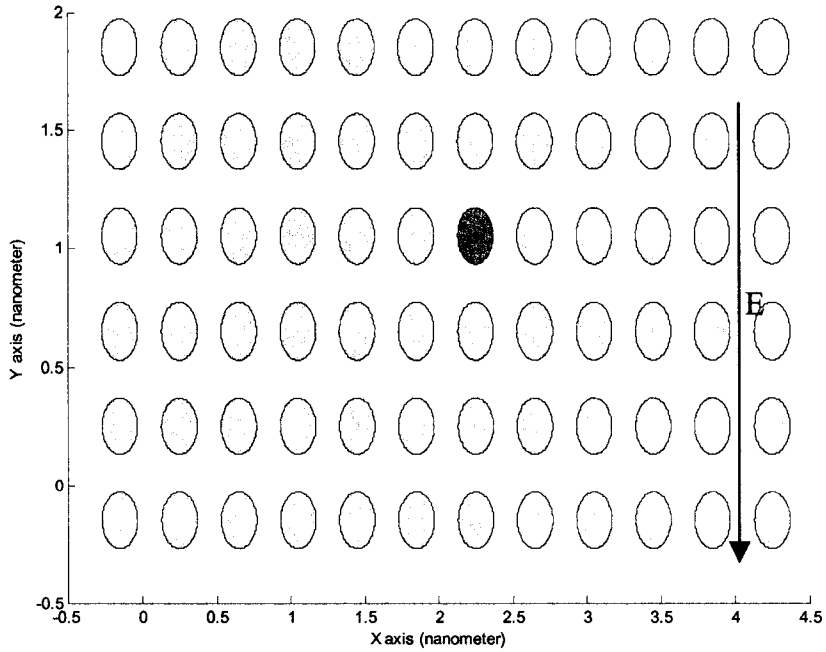

Fig. 12 (a) Initial state of system with central ion surrounded by water molecules. The orientation of water dipoles are not in the direction of external E field initially.

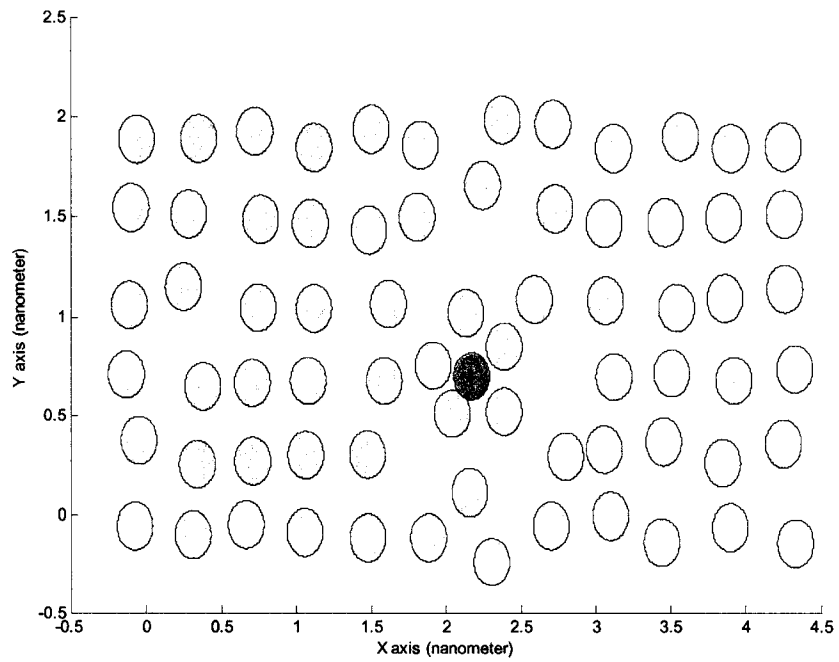

(b) Water dipoles start to change their orientation to form a cloud around the ion due to the presence of a positive ion and E field.

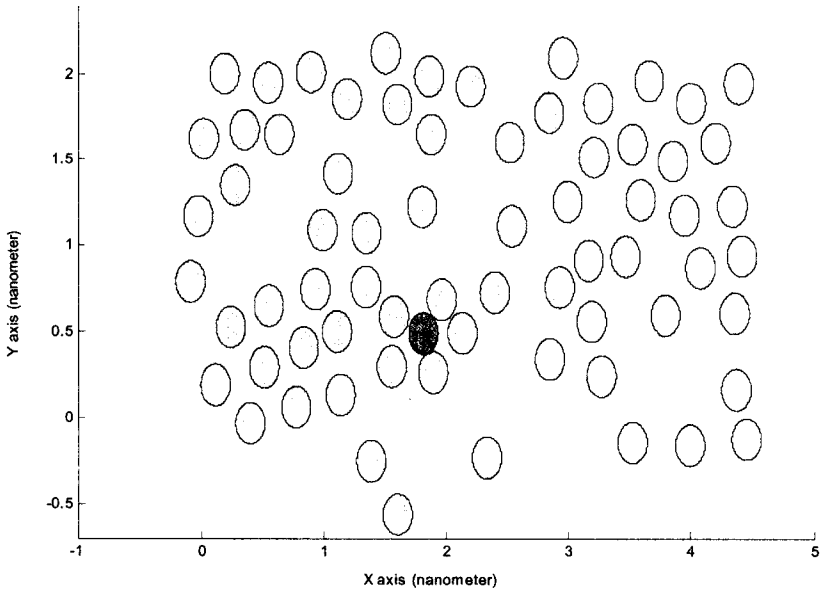

(c) Water molecules moves with the ion.

CHAPTER IV

SIMULATION RESULTS AND DISCUSSION

4.1 Introduction

In this chapter, selected simulation results are presented. Static transmembrane voltage and current are calculated with the improved energy model that is described in chapter 3. The corresponding results are shown in section 2. The pore dependent energy model is much better than the model used in the literature, and is discussed in section 3. Section 4 is on long pulse induced cell deformation. Cellular manipulations are discussed in section 5. Different cellular responses of tonsillar B normal and malignant cells are compared, and voltages across the cellular membranes and energy distributions over the whole single cell are calculated. Section 6 provides a molecular level view of pore formation induced by external ultra short, high-energy pulses.

4.2 Static Transmembrane Voltage and Current Calculations

4.2.1 Pore Formation Energy Function With Fixed Surface Tension

The pore formation energy function for hydrophilic pores is shown in Fig. 4.1 based on Eq. (3.1.1b) for various values of the r_∞ parameter. Its characteristics are important since the pore dynamics are governed by this energy function. Essentially energy is required to create a "circular" edge for pore formation. However, a deduction has to be considered to account for the elimination of the membrane surface area. For a monotonically decreasing value of the surface tension with pore radius, as implied by a finite r_∞ parameter, contributions to an energy decrease are reduced leading to increases

in the formation energy. This is evident from the three curves of Fig. 13 corresponding to three different r_∞ values. A fixed, high value of Γ corresponding to the $r_\infty = \infty$ limit yields the lowest energy. Physically though, $r_\infty = \infty$ is an incorrect representation for two reasons. First, it implies that the pores are able to expand without bound and never stabilize. This would lead to nonphysical density enhancements in the nonporous regions of the membrane, or thickness increases. Second, $r_\infty = \infty$ incorrectly implies that the tension is unaffected by changes in the membrane area. Though direct experimental verification of surface tension is unavailable, molecular dynamics simulations of lipid bilayers do demonstrate the following [111]: (a) Finite tension is required to maintain a given cellular shape and size, and (b) the tension must change with the system area. Also, indirect experimental evidence indicative of variations in membrane tension is available. For example, activation of the 3-ns mechanosensitive channel large cloned from *E. coli* [112] has been linked to the tension of lipid membranes. Similarly, the activity of lytic peptides is affected by the tension of vesicles under stress [113], and the catalytic activity of a β isoform of phospholipase *C* shown to change with surface pressure [114]. These experimental results suggest that the tension must naturally be variable, and that its variation facilitates biological activities that are observed. Third, since tension is proportional to the membrane area, at least to first order, it follows that changes due to pore formation will lead to variations in G that are proportional to the square of the pore radius.

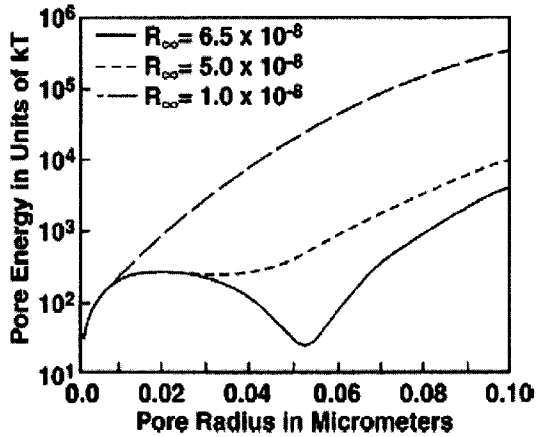

Fig. 13 The pore formation energy function for hydrophilic pores for various r_∞ values.

For a finite value of r_∞, the formation energy not only increases, but also exhibits a local minimum. This implies that the pores can expand upon the application of external electric fields, but will eventually stabilize to some large average value as dictated by the minima. This leads to the following consequences. (i) First, for pore creation and cellular manipulation, a somewhat larger external energy will be necessary to create large pores due to the variable surface tension. (ii) Second, for cellular destruction, a sufficiently large voltage must be applied for a sufficiently long time to transcend the energy barrier and ensure that pores move into the energy minima. (iii) Pore resealing, in the presence of a local minimum (e.g., as in the r_∞ = 65 nm curve of Fig. 13), becomes a two-step process. An initial rapid decrease is expected to occur due to the diffusion of pore with radii smaller than the local minima toward small r space. However, those lying beyond the local minima will remain "trapped" and will diffuse to lower r values very slowly. Hence, conceivably, a small fraction of the pore will remain open for long times, provided the initial voltage and time duration were sufficient to carry them over the barrier. (iv) Finally, the two-step process implies that there is an optimal time-window for

cellular destruction. If, for example, a second voltage pulse can be applied before the fast first-step has not fully completed, the potential for damage will be rather high. On the other hand, applying a second voltage pulse after the end of the fast resealing process,

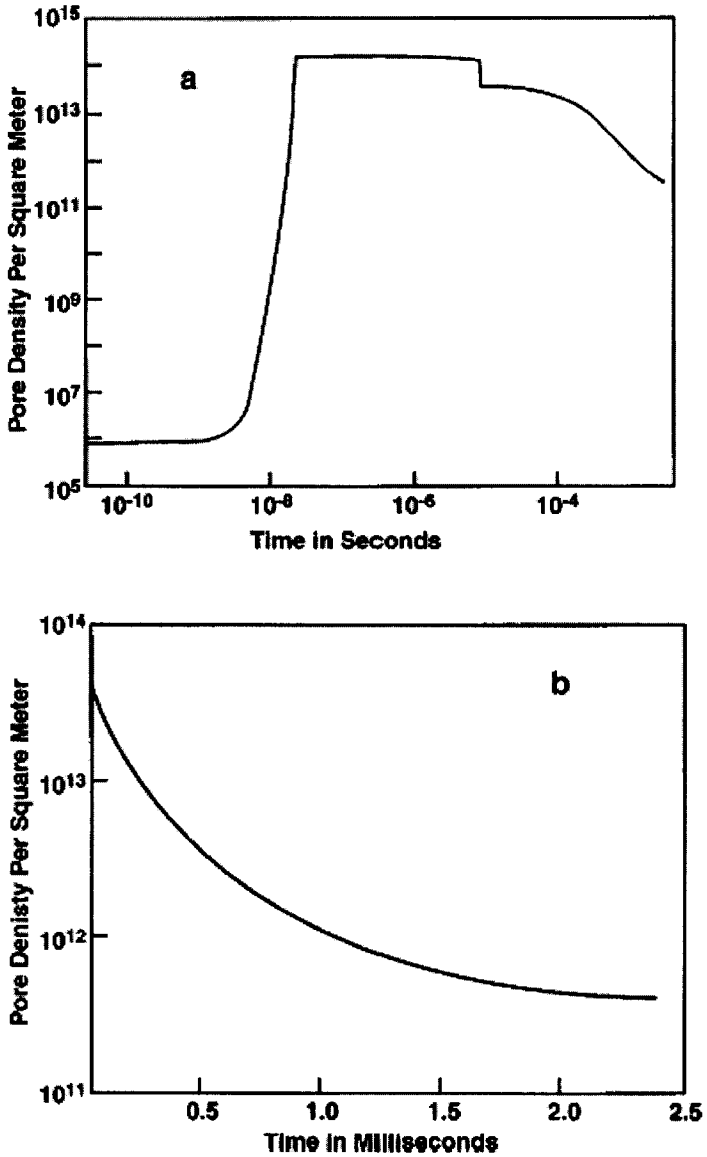

Fig. 14 Simulation result for the pore density evolution with time in response to 4 ms, 10 kV/cm rectangular electric pulse. (a) Logarithmic scale, and (b) semilogarithmic graph.

only a few pores will be open, and a high membrane potential will not be developed due to their high conductivity. This suggests that for maximal damage, a series of short pulses with delays less than that of the fast process time constant will be most desirable.

4.2.2 Self-consistent Transmembrane Voltage Calculation

Self-consistent simulations based on the coupled Laplace-Nernst-Planck-Smoluchowski equations were carried out next to evaluate the temporal response to ultrashort, external electric pulses. A 10 kV/cm rectangular external electric field pulse with a 4 μs duration was assumed. These parameters were chosen in keeping with actual pulsed field experiments conducted on *E. coli* in our laboratory to facilitate comparisons between theory and experiment. The cell radius was chosen to be 1.0 μm and a membrane thickness of 5 nm that is roughly characteristic of *E. coli*. Fig. 14 shows the

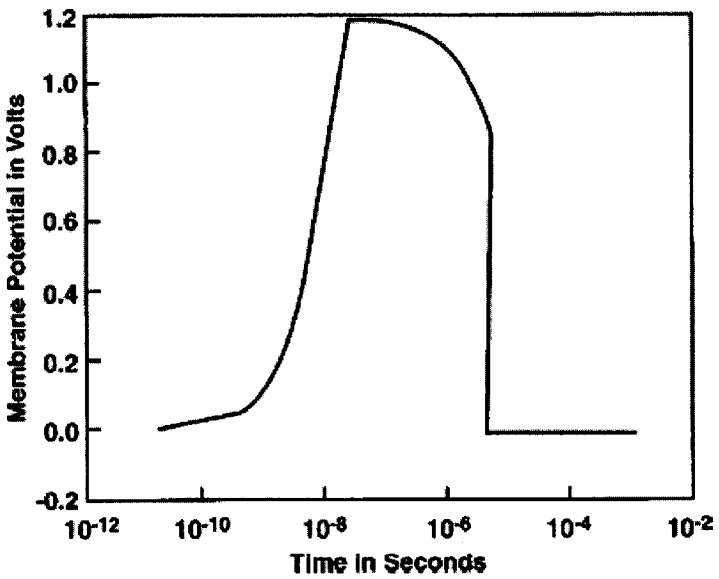

Fig. 15 Calculated temporal variations of the transmembrane potential in response to a 4 μs, 10-kV/cm rectangular electric pulses.

dynamic evolution of the pore density. An initial delay of about 5 ns seen in Fig. 14(a) is due to membrane charging and for V_{mem} to build up to levels at which the pore creation rate becomes substantial. A peak value of about 2×10^{14} m^{-2} is reached after about 20 ns. Subsequently, the pore density shows a slight monotonic decrease over the remaining duration of the 4 μs external pulse. This occurs due to a substantial increase in the membrane conductance and a consequent decay in V_{mem} that controls the pore generation. Details of the time-dependent membrane voltage are shown in Fig. 15. The voltage exceeds 1.0 V at about 15 ns, and reaches a peak value of roughly 1.2 V. At this point the pore conductance increases to such a degree that the voltage across the membrane capacitance begins to fall. The overall result is a ''voltage overshoot'' behavior. It agrees well with a previous report on the time-dependent behavior of the membrane voltage by Meier *et al.* [115]. As the external electric field is turned off beyond 4 μs, the transmembrane potential falls dramatically with a time constant in the sub-microsecond range. The fast drop off is the result of a large conductance, and hence, a low internal ''RC'' time constant. A final steady-state value of about 280 mV, equal to the rest potential is finally reached. The corresponding influence on the pore density, as seen from Fig. 14(a), is a sharp decrease by about fifty percent following the turn-off. Beyond this, the density continues to decrease, but at a relatively low rate until about 0.1 ms. This implies that many of the pores tend to remain open, well after the 4 μs pulse is switched off. Hence, a second electric pulse applied within this duration is likely to have a substantial damaging effect. This is borne out in our experimental measurements on *E. coli*, as discussed later. Also, this 0.1 ms time delay corresponds well with an experimental report by Meier *et al.* [115]. Beyond 0.1ms, the rate of pore reduction

increases. The long time behavior can best be gauged from the semilogarithmic curve of Fig. 14(b). It shows a gradual slowing in the resealing rate. At the 2.4 ms instant, and "effective decay time constant'' of 4.5×10^{-3} s is computed from the results. Based on this time constant, a lower bound on the duration for near-complete pore resealing can be estimated. It works out to 0.12 s. In actuality, though, the duration would be even longer since the decay curve of Fig. 14(b) exhibits a continuous slowing down. It is, therefore, natural to expect that the pore decay will weaken even further at longer times, and resealing durations spanning several seconds or even minutes, will result. In any case, the projected resealing values are in the 10^{-1}–10^{2} s range, in keeping with experimental reports [116, 117].

The dynamical behavior can easily be understood in terms of the formation energy characteristic of Fig. 13. Initially, the pores that are not near the local minima, and have values in r space that is below the barrier. These pores tend to drift and diffuse toward $r\rightarrow0$, giving rise to a fast decay. However, this leaves behind an ever-increasing higher fraction of larger pores that are near the local minima. Those near the minima move in r space primarily through diffusion, and hence, the system takes a long time to completely recover to the original steady state.

4.3 Pore Dependent Energy Model

4.3.1 Energy Function With Variable Pore Area

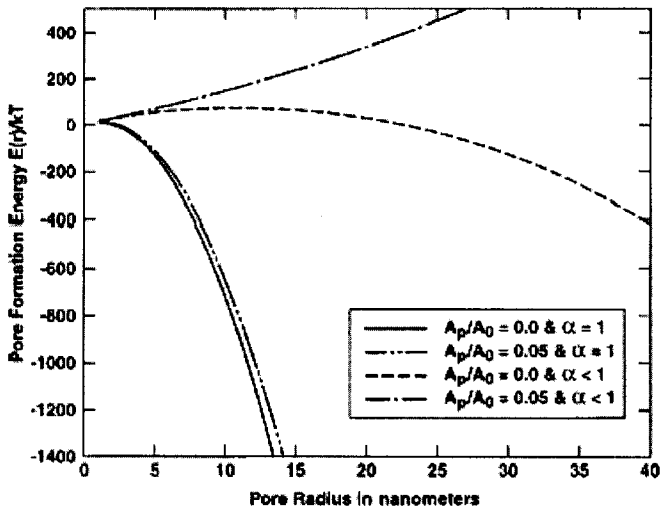

Fig. 16 Pore formation energy function for a 0.4 V transmembrane bias under various conditions of surface tension and pore population.

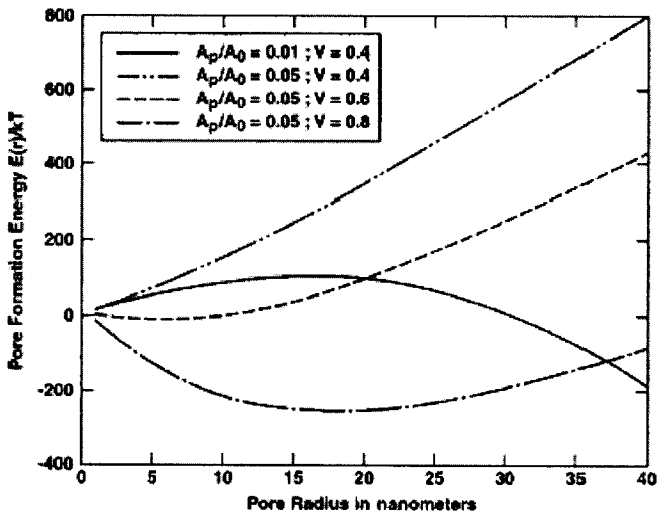

Fig. 17 Dependence of $E(r)$ on membrane voltage and relative pore population.

While a self-consistent solution of the coupled equations (3.2.3), (3.3.5d), and (3.3.6) is necessary, we first present some simple results based on Eq. (3.3.6) alone for fixed A_P values. The motivation for these calculations was simply to demonstrate the changes in $E(r)$ produced by the modified model, and to facilitate relevant comparisons with the results of Fig. 4. Though strictly a constant A_P assignment is inaccurate because of the dynamic nature of the system, its use nonetheless helps us to provide physical insights of pore diffusion in r space and afford qualitative trends of the $n(r,t)$ evolution at a specific time instant. Figure 16 shows $E(r)$ vs r with and without the improved electrostatic correction term (i.e., a, 1 and α=1, respectively). The calculations included two cases: one with no pores (A_P/A_0=0) and the other with a specific pore area given by A_P/A_0=0.05. The membrane voltage for Fig. 16 was set at 0.4 V. With α=1, the voltage dependent contribution to the pore formation energy is quite dominant, and leads to large negative $E(r)$ values with a monotonically increasing slope for larger radii. Also, there is no potential barrier, and this trend is predicted both with and without pores. Due to the pore-dependent correction in surface tension [via Eq. (3.3.5c)], the curve with $A_p / A_0 = 0.05$ is slightly higher. Upon including the role of finite ionic conductivity in the pores through an $\alpha(r) < 1$ term [as given in Eq. (3.3.1)], the pore formation energy is seen to increase dramatically. A local maxima corresponding to a slight potential barrier is evident in Fig. 16 at a radius of about 13 nm for the a<1 and A_P/A_0=0.05 case. Including the surface tension correction as well for a<1 completely changes the energy function. Instead of a convex curve, $E(r)$ becomes slightly concave with positive values throughout the entire 0–40 nm radial ranges. Physically, this implies that the system would naturally drive the pores towards lower radii (and hence, smaller A_P/A_0) under these conditions.

Alternatively, a pore population of such large radii (effectively leading to A_P/A_0=0.05) would not be created or supported in the first place, at this 0.4 V bias. It also becomes apparent that the effect of having a finite pore population (i.e., A_P>0) is stronger when the ionic conduction term (i.e., a<1) is also taken into account.

4.3.2 Pore Density

Similarly, the behavior of $E(r)$ on membrane voltage and relative pore population, but without the dynamic, self-consistent calculations involving $n(r, t)$, is shown in Fig. 17 At the lowest membrane bias of 0.4 V and a relatively high A_P/A_0 ratio of 0.05, the $E(r)$ curve is positive and exhibits a monotonic increase with radius. For a slightly lower value of A_P/A_0=0.01 at 0.4 V (correspondingly also to a lower surface tension), the curve is dramatically altered and exhibits a local maxima at r~16.5 nm, with negative $E(r)$ values beyond 31 nm. Thus, there is a shift from an unconditionally stable situation for $A_P / A_0 = 0.05$, to potential instability with a change in the pore population. The curve for a 0.6 V membrane potential and A_P/A_0=0.05 exhibits a concave structure with a clear energy minima at around 7 nm. Thus, under these conditions, the cell is predicted to remain perforated in a stable manner without irreversible rupture. Finally, at a still higher bias of 0.8 V, the trend remains unaltered, though the location of the stable minima is predicted to shift to the higher radial value of 18 nm. The central point that becomes transparent from the curves of Figs. 16 and 17 are that the stability of the porated cell is delicately controlled by a combination of parameters that include surface tension, the ion conductance, and pore population. Furthermore, the modified energy model predicts that changes in the magnitude and slope of $E(r)$ can easily occur to profoundly impact the

diffusion of pores in r space. Finally, a self-adjustment in $E(r)$ arising from changes in $n(r,t)$ [and hence, A_P / A_0] would make it possible to curb uncontrolled pore growth and expansion.

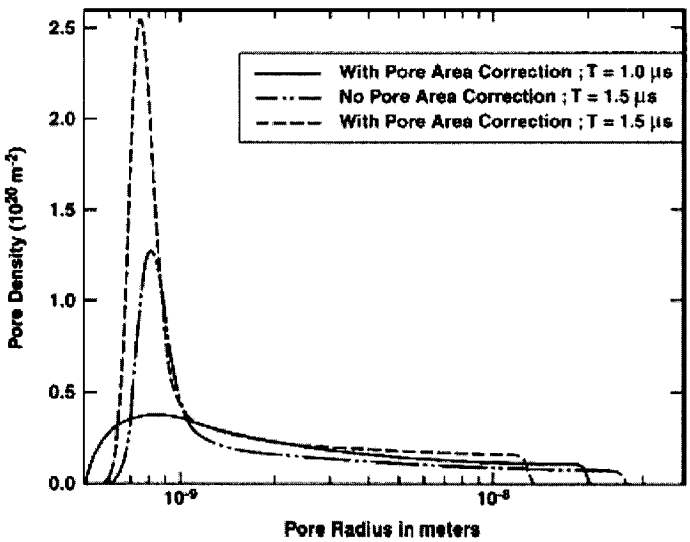

Fig. 18 Calculated pore distribution $n(r)$ at time instants of 1.0 and 1.5 ms in response to a 1.0 V, 1 ms electrical pulse. Curves with and without the pore area dependence in the energy model are shown.

4.3.2 Summery

Self-consistent calculations were performed next by coupling the Smoluchowski equation with Eq.(3.3.6) for the pore formation energy. A 1.5 V, 1 μs external pulse was assumed for the analysis. For purposes of quantifying the role of a pore area on the dynamic evolution, two sets of simulations were carried out. In one, a constant surface tension was used [i.e., $\Gamma_{eff}(A_P=0)$], while for the other simulation set, a pore area-dependent formation energy as given by Eqs. (3.3.5c) and (3.3.6) were utilized. Results of the pore density distributions $n(r)$ for both simulation conditions are shown in Fig. 18

at the specific time instants of 1.0 and 1.5 μs. Comparison of the two 1.5- μs curves (with and without the area correction, i.e., $A_P \neq 0$ and $A_P = 0$, respectively) of Fig. 18, brings out the following features.

(i) A stronger peak with inclusion of the pore area term that roughly lies at a radius of 0.77 nm. Without the pore area term, on the other hand, the most probable radius is predicted to be somewhat larger at 0.82 nm.

(ii) Without the pore area term, the $n(r)$ distribution is predicted to have a much larger spread with pore radii as large as 27 nm. With $A_P \neq 0$, the maximum pore radius after 1.5 ms is predicted from Fig. 18 to be only about 13 nm. These results can easily be understood in terms of a higher pore formation energy (as shown qualitatively in the curves of Fig. 16) for $A_P \neq 0$, and the positive slope that leads to diffusion in r space towards smaller radii. Thus, the overall result is a faster recovery upon the inclusion of the pore dependent (and hence, variable surface tension) factor. The 1.0- μs curve for $A_P \neq 0$ is flatter than the corresponding 1.5- μs curve with a larger variance and higher peak pore radius, as might be expected. With the voltage pulse just at the point of being turned off, the pore distribution is out of equilibrium, but begins its shift towards a low profile, equilibrium profile.

The effects of including the pore-dependent formation energy $E(r)$ are also made evident through the time dependence of the average pore radius $\langle R(t) \rangle$. Plots of $\langle R(t) \rangle$ up to a 1.5 μs time, with and without the pore area factor, are shown in Fig. 19. Both curves increase monotonically as long as the 1- μs voltage pulse remains effective. However, the growth of pores is not quite as rapid for $A_P \neq 0$, and hence, the average radius does not increase quite as much. Beyond 1μs, both curves begin to decrease as the

pores begin to shrink. However, for $A_P \neq 0$, there is a driving force towards smaller radii for pores of all sizes as governed by a positive slope for the $E(r)$ function.

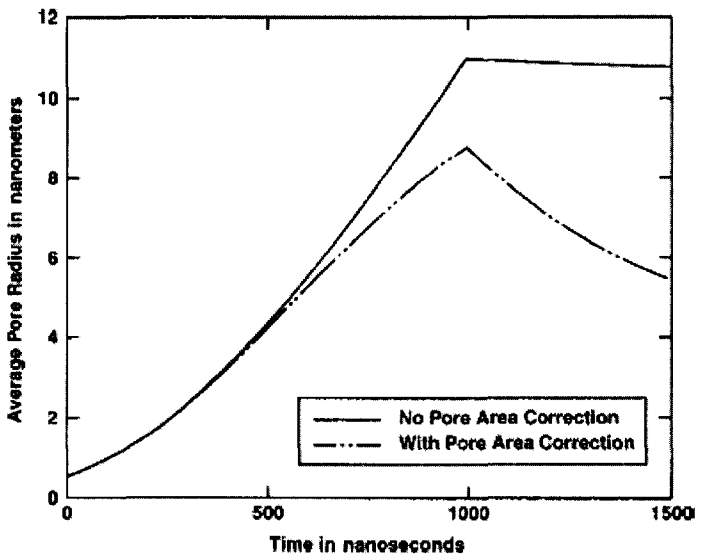

Fig. 19 Results of the average pore radius $<R(t)>$ to demonstrate the effect of including a pore dependent energy model.

Consequently, the average size decreases at a fairly rapid rate. However, in the absence of a pore area term, the $E(r)$ function has a local maximum at about 18 nm as given by the V=0 curve of Fig. 4. Consequently, pores with radii below 18-nm shrink, while those above 18 nm continue to grow. The two almost offset each other, and only a small net decrease in $<R(t)>$ is predicted in Fig. 19. The time evolution of the pore formation energy $E(r,t)$ that dictates the dynamics and movement in r space, is shown in Fig. 20. With no pore corrections, $E(r)$ at 1.5 μs exhibits a slight maximum, and has both positive and negative slopes. With A_P taken into account, a concave curve with a positive slope is seen for both the 1.0 and 1.5 μs time instants. The 1.0- μs curve is slightly higher because of the higher pore area at this earlier time. As the system tends towards

equilibrium and pores shrink, the pore area decreases and leads to a lowering of the $E(r)$ curve. The dynamic feature of $E(r,t)$ is thus made obvious.

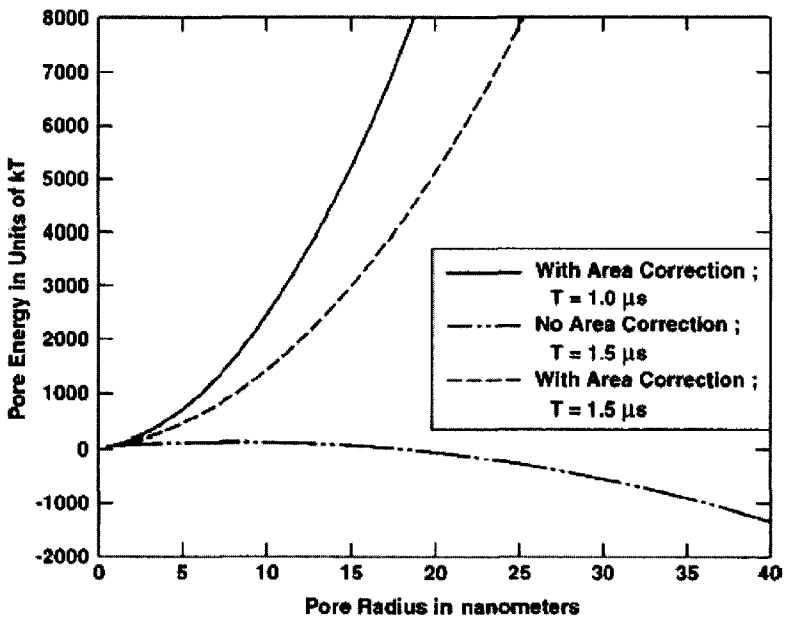

Fig. 20 Pore formation energy $E(r,t)$ under three conditions showing its dynamic nature.

4.4 Cellular Deformation Calculations

4.4.1 Electro-induced Cellular Shape Changes

Numerical calculations based on the equations of the previous section were performed to determine the effect of external electric fields on cellular shape changes. A list of parameters used in the computations is given in Table 4. For accuracy the full stress theory [i.e., Eqs. (3.4.2) and (3.4.3)] was used without neglecting the bending forces and moments. A fourth-order Runge-Kutta method was used to numerically solve the resulting coupled differential equations. For self-consistency, the electric fields at the surface for each geometrical shape had to be computed. This, in theory, can be accomplished by applying boundary conditions [Eq. (3.4.9)], and solving for all the

Legendre-polynomial coefficients. However, such a procedure presents two practical difficulties. First, for successful numerical solution, a finite set of difference equations is

Table 4 Parameters used in the deformation model.

Parameter	Value	Source
k_{r1} (Fm^{-1})	$80\times8.85\times10^{-12}$	[86]
k_{r2} (Fm^{-1})	$2\times8.85\times10^{-12}$	[86]
a (m)	1×10^{-6}	[8]
t (m)	$(3\text{-}5)\times10^{-9}$	[8]
K(J)	5×10^{-20}	[92]

needed. This implies having to invoke additional (perhaps arbitrary) conditions on the infinite Legendre series for closure. Second, evaluation of the normal derivatives [as in Eqs. 3.4.9(c)– 3.4.9(d), for example] and radius of curvature [e.g., $r1$ in Eqs. (3.4.2) and (3.4.3)] is ''noisy'' and leads to inaccuracies in numerical implementations. In order to circumvent the above difficulties, a slightly different approach was used here for the self-consistent analysis. A coupled iterative procedure was followed. First, Esq. (3.4.2) and (3.4.3) were solved for the applied electric-field value (i.e., without self consistent polarization corrections) to yield the deformed cell shape. Next, this shape was parameterized into an ''ellipsoidal'' form by a curve-fitting procedure that yielded the best fit values of the semi major and semi minor axes, a and b, respectively. The equations for the electric-field distribution for the ellipsoidal geometry [as given in Esq. (3.4.14) and (3.4.15)], were then applied. This updated electric-field distribution was used once again to yield a more realistic shape based on Eqs. (3.4.2) and (3.4.3), and the process iterated until convergence. Obviously, since the deformed cell shape can, in principle, deviate appreciable from an ellipsoidal geometry at high electric fields (E) or

large membrane thickness (t) values, the simulations were carried out for relatively small E and t magnitudes.

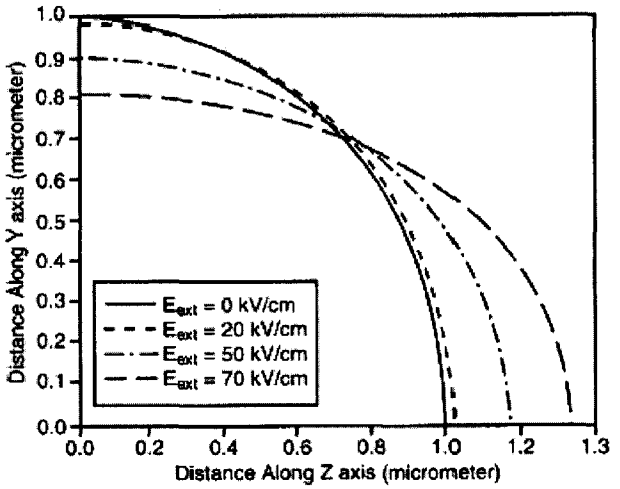

Fig. 21 Calculated equilibrium cell shapes along the y-z plane in response to applied electric fields of 0, 20, 50, and 70 kV/cm. Polarization effects were ignored.

Results for an initial spherical cell of thickness 2 nm having a 1 mm radius (typical of *E. coli* cells, for example) In response to various electric field values are given in Fig. 21. Field magnitudes ranging from 0–70 kV/cm were used. The Poisson's ratio n was taken to be 0.2. The steady-state deformed cell shapes for positive z and y variables in the x=0 plane, are shown in Fig. 21. Due to the inherent symmetry of the problem, only the first quadrant is specified for simplicity. The shape changes from a perfect circle for E=0 V/cm, to ellipsoidal with increasing eccentricity at higher fields. The corresponding forces per length $N_\phi(\phi)$ and $N_\theta(\phi)$ are shown in Fig. 22 for fields of 20, 50, and 70 kV/cm. The magnitudes range from 0 to about 25 mN/m. The values of N_ϕ are positive, independent of the angle, and increase with field. This implies that $N_\phi(\phi)$ produces a

constant tension across the membrane. Plots of $N_\theta(\phi)$ show positive magnitudes for angles below 30°, and become progressively negative reaching a maximum along the

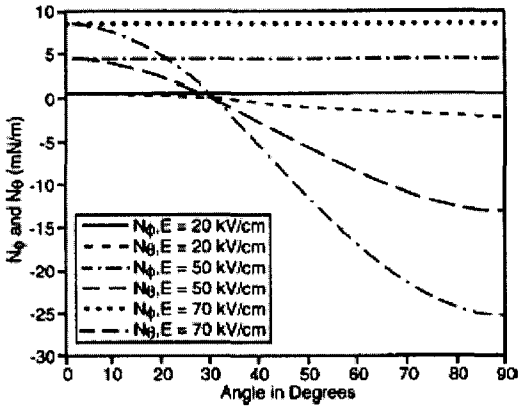

Fig. 22 Corresponding forces per length $N_\phi(\phi)$ and $N_\theta(\theta)$ for applied fields of 0, 20, 50, and 70 kV/cm.

equatorial plane. The signs are simply the result of the chosen ϕ direction as depicted in Fig. 6. At low angles (i.e., close to the semi-major axis), positive $N_\theta(\phi)$ denotes a state of tension with component roughly transverse to the *z-axis*. The negative values near $\phi \sim 90°$, for example, signifies a transverse (i.e., *x-z* plane) compression in response to the tension in the *y-z* plane. As reported in the literature [118], the typical tension for membrane rupture is in the range 1–10 mN/m. Our results are thus in very good agreement, and show that for applied electric fields of 50 kV/cm and higher, one can expect membrane rupture simply based on electromechanical considerations. The exact value will obviously depend on the rigidity parameter K and the Poisson's ratio ν, but the magnitudes as predicted by this simply analysis should roughly remain valid.

The deformed cell shape strongly depends on the cell characteristics. Changes in the rigidity parameter or the membrane thickness alter the force distributions, and hence,

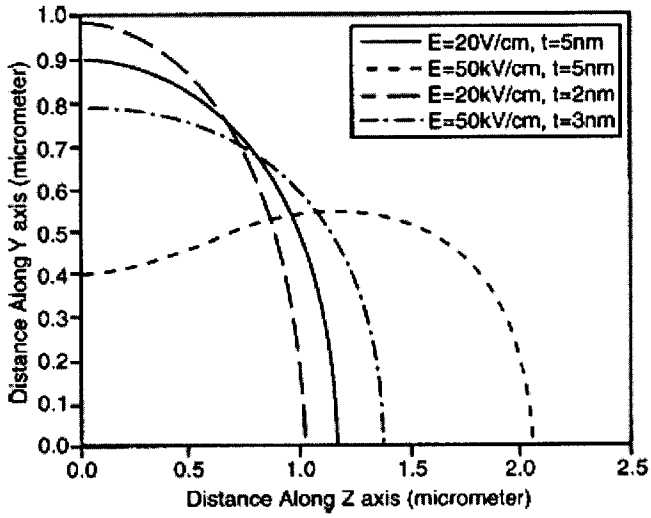

Fig. 23 Deformed cell shape results for various membrane thicknesses and applied fields of 20 kV/cm and 50 kV/cm.

affect the overall shape. Calculated results of the deformed geometry for a 1 mm radius starting from an unstressed spherical cell are given in Fig. 23. The membrane thickness ranged from 2–5 nm and various electric fields were used. The curves of Fig. 23 show very clearly that besides applied electric fields, the deformation is controlled by the membrane thickness, and increases with "*t*." As the thickness changes from 2 to 5 nm, the geometry is modified from spherical to ellipsoidal and then begins to assume a "peanut" shape (or discocyte transformation [119]). Based on the trend evident in Fig. 23, one could qualitatively predict an eventual shift towards "dumbbell" geometry at higher fields, or thicker membranes, or under conditions of a smaller rigidity parameter, or with a larger Poisson's ratio. Such calculations for strongly deformed shapes, however, have not been shown here since the perturbative theory used in this analysis could be called into question for large deformations. In any case, it becomes evident that deviations from a simple geometry are indeed possible, and that the ellipsoidal form often used in previous work may not be the most accurate representation. It may also be

mentioned that in actual practice, a slight change in the membrane thickness is likely during cellular deformation process. For example, a net expansion of the surface area would give rise to a marginal decrease in the membrane thickness "*t*." Based on the results of Fig. 23, such a "second-order" effect on "*t*" would work to slightly diminish the overall deformation.

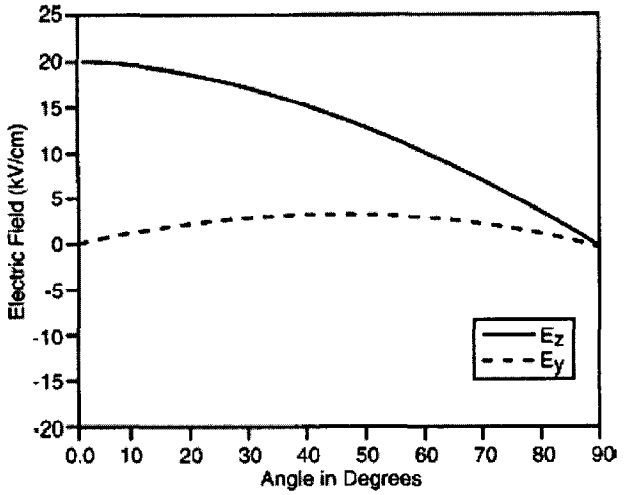

Fig. 24 Electric-field profiles just outside a 1 mm radius spherical cell in response to an external 20-kV/cm field. The relative permittivities for the membrane and surrounding media were set at 81 and 2, respectively.

Deviations in the electric-field distribution due to the presence of the dielectric media are discussed next. The field profile for the components *Ey* and *Ez* are shown in Fig. 24 for a 1 mm radius spherical cell subjected to an external 20 kV/cm field was used, with relative permittivities of 81 and 2, respectively, for the membrane and surrounding media. Due to induced charges on the dielectric spherical membrane, the electric-field lines *Ez* deviate from their parallel orientation and tend to cluster at the cell. Consequently, the radial field increases with the largest change from the 20kV/cm value at the pole which corresponds to $\phi = 0$. As expected, the radial component falls to zero at the equatorial plane which corresponds to $\phi = 90°$. Due to the field distortion, the resultant field is no

longer solely along the *z* direction, but instead has a small *Ey* component (largest at ϕ = 45°) and a deviation about the 20 kV/cm level in *Ez*. More significantly, the transverse component with polarization is smaller (i.e., less negative) which will lead to a decrease in the equatorial "flattening."

4.4.2 Cellular Volume and Surface Area

Finally, self-consistent numerical simulations were carried out to evaluate the field-dependent changes in the cell volume and surface area. The rationale for this calculation was the following: From an experimental standpoint, observations of absorbance dichroism and changes in optical scattering can be made, and these effects are associated with variability in cell surface area. It is, therefore possible to quantitatively observe and monitor areal changes and gauge the dependence on applied electric field through optical measurements. Analysis of such field-dependent variations is thus a meaningful first step towards comparisons with experiments, and for data interpretation.

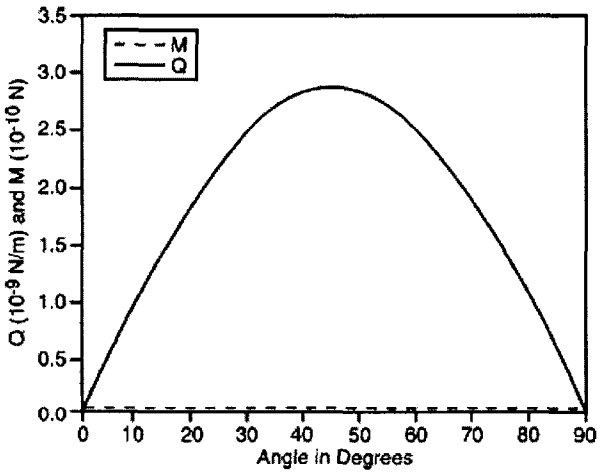

Fig. 25 The bending moment $M_\phi(\phi)$ and associated transverse force $Q_\phi(\phi)$ for applied field of 20 kV/cm for an initial 5 nm spheroid.

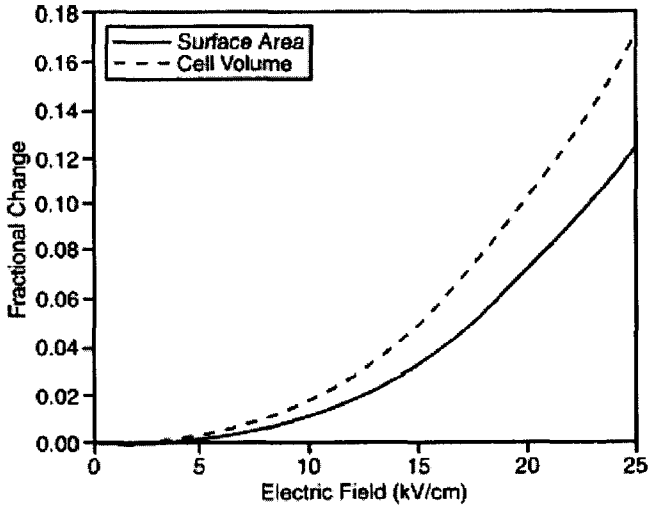

Fig. 26 Calculated variations in the cellular surface area and volume with applied electric field for an initial 1 mm cell radius and 5 nm membrane thickness.

Figure 25 shows the bending moment $M_\phi(\phi)$ and associated transverse force $Q_\phi(\phi)$ for an applied field of 20 kV/cm for an initial 5 nm sphere. As seen from the curve, the magnitude of $M_\phi(\phi)$ is negligibly small and has a nearly constant value of about 3×10^{-12} Newtons. The curve for $M_\theta(\phi)$ was nearly identical to that of $M_\phi(\phi)$, and so has not been shown separately in the figure. This $M_\theta(\phi)$; $M_\phi(\phi)$ condition obtained here is in keeping with a previous result reported by Pamplona and Calladine [120]. The angular dependence of $Q_\phi(\phi)$ from Fig. 25 is seen to be symmetric about $\phi = 45°$, and also has a relatively small value. Thus, compared to both $N_\phi(\phi)$ and $N_\theta(\phi)$, the variables $Q_\phi(\phi)$, $M_\theta(\phi)$, and $M_\phi(\phi)$ can all be neglected as has been done in the past. Finally, Fig. 26 shows the fractional change in the cellular surface area and volume as a function of the applied electric field. Two points are evident from the results. First, both curves exhibit a rough quadratic behavior.

This is in keeping with some recent optical scattering experimental data [121]. The exact magnitudes, however, are subject to the inaccuracies and uncertainty of the material parameters such as the rigidity K and Poisson's ratio n. Hence, the data of Fig. 26 does not lend itself to a direct comparison with experimental data. However, the general electric-field dependent trend predicted here has been shown to be accurate. A second point about Fig. 26 is that the change in cell volume is larger than the corresponding areal variation. This is to be expected as the volume scales more rapidly than the surface area, at least for the simple ellipsoidal shapes. At higher electric fields beyond the 25kV/cm value shown in Fig. 26, it is conceivable that the areal variations become larger as the cell changes from an ellipsoidal to a ''peanut-discocyte geometry'' as shown in Fig. 23 for the 50 kV/cm field.

4.5 Cellular Manipulations

Cell properties, such as conductivity, permittivity, and membrane thickness play an important role in electroporation. It is well known that normal and malignant cells have different dielectric and geometric properties [122]. If should, therefore, be possible to take advantage of this difference, and possibly use ultra-short pulses for selective destruction.

4.5.1 Transmembrane Voltage of Tonsillar B-cells

Here, as an example, we chose normal and malignant (Farage) tonsillar B-cells to look at differences in response. Parameters used in our simulation are shown in Table 5. Simulation results of the time dependent transmembrane potential for a normal B-cell subjected to a trapezoidal pulse are shown in Fig. 27. The pulse was 45kv/cm in

magnitude, with rise and fall times of 10ns, and 50ns, respectively. During the initial 500 ns of the simulation, there was no external pulse. However, this time was used to allow the system to reach an initial steady state. In Fig. 27, the outer membrane is predicted to

Table 5 Simulation parameters of normal and malignant tonsillar B-cells [122].

	Normal B-Cell	Cancer (Farage) B-Cell
Conductivities (S/m):		
Environment	0.6	0.6
Cell membrane	5.6×10^{-5}	9.1×10^{-6}
Cytoplasm	1.31	0.48
Nuclear envelope	1.11×10^{-2}	4.4×10^{-3}
Nucleoplasm	2.04	1.07
Relative Permittivity:		
Environment	80.0	80.0
Cell membrane	12.8	9.8
Cytoplasm	60.0	60.0
Nuclear envelope	106	60.3
Nucleoplasm	120.0	120.0
Geometry parameters (μm):		
Radius of the simulation region	10.0	10.0
Radius of cell	3.3	5.2
Thickness of cell membrane	0.007	0.007
Radius of nucleus	2.8	4.4
Thickness of nuclear envelope	0.04	0.04

porate after about 25 ns. The nuclear membrane, however, holds off the voltage with the transmembrane potential reaching a maximum of about 4 Volts. Effective conductivities of membranes versus time are shown in Fig. 28. It shows the initial conductivity of the outer membrane is much lower than that of the nuclear membrane. However, upon the E-field pulse, the outer membrane porates, and its conductivity increases dramatically, surpassing that of the nuclear membrane. The pores form very quickly after the termination of the pulse. Fig. 29 shows the temporal development of the average pore radius at the outer and nuclear membranes for a normal B-cell. During the first 500 ns, pores form and reach a near steady-state radius of about 0.75 nm. Application of the

external pulse at $t = 500$ ns, causes a sudden surge in pore formation. Since these newly formed pores are of relatively small radius, the overall average exhibits a near-instantaneous drop. However, as the newly formed pore grow in size, the average pore

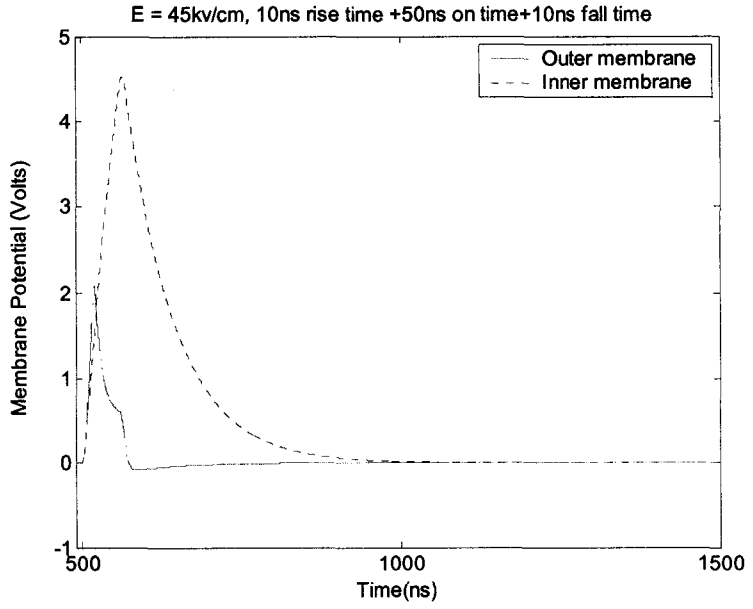

Fig. 27 Time dependent membrane potentials.

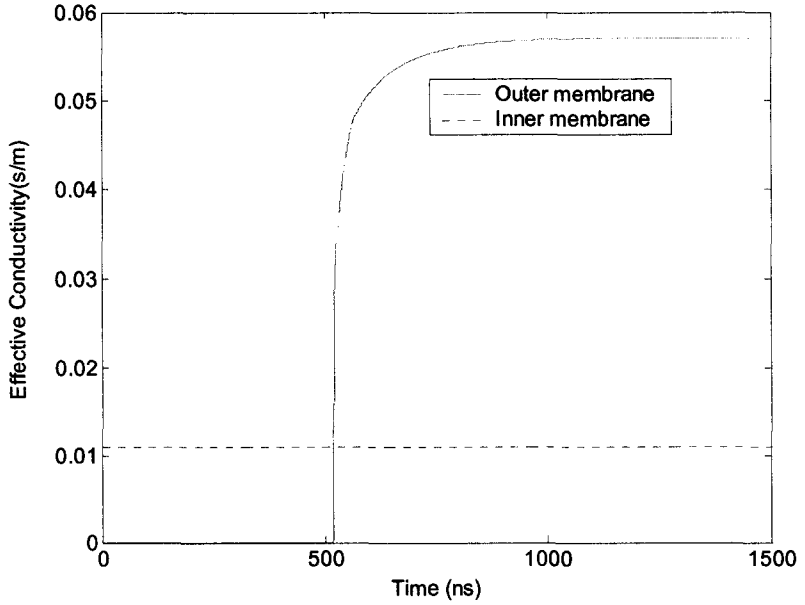

Fig. 28 Conductivities of outer and nuclear membranes.

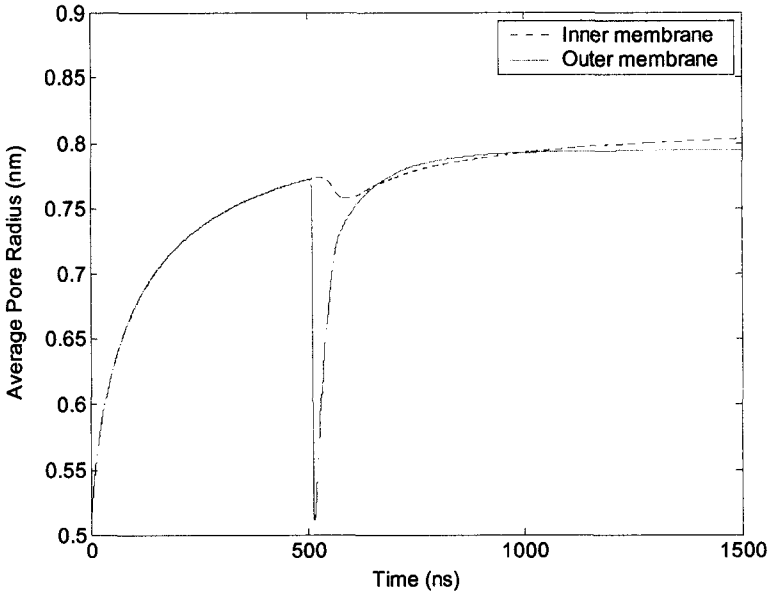

Fig. 29 pore radius versus time for normal cell.

radius begins to increase, and eventually and eventually surpasses the ~0.75 nm equilibrium value. If the electric field intensity is increased from 45kv/cm to 100kv/cm, the nuclear membrane of normal B-cell was found (not shown here) to remain intact while the outer cell membrane porated.

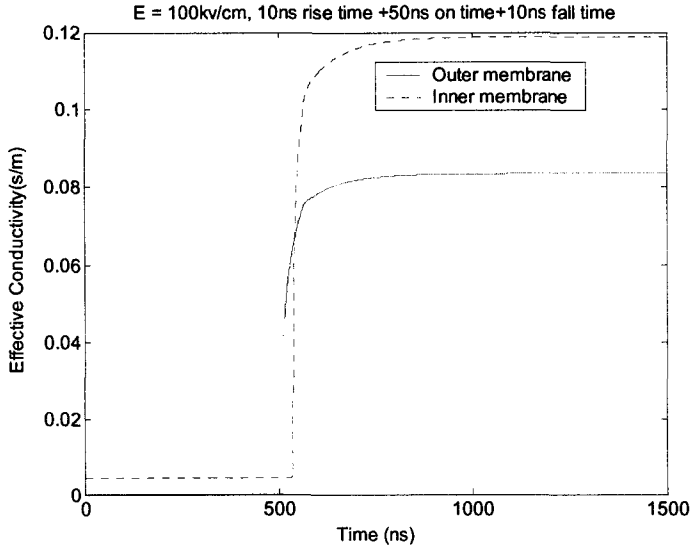

Fig. 30 Membrane conductivities vs. time for cancer cell.

On the other hand, for cancer cells, the simulation predicted both membranes would be porated. Fig. 30 shows the effective conductivities of both the outer and nuclear membranes changing with time. Thus, our calculations clearly show that normal B-cell and cancer B-cell have different responses to nanosecond pulses. A summary of the results under various E-pulse stimuli is given in Table 5. It becomes obvious that for normal cell, no matter what the electric pulse intensity, the nuclear membrane would not porate. However, for the Farage cells, nuclear membrane poration is predicted for pulse intensities of ~100kv/cm, or higher.

4.5.2 Temperature increase of tonsillar B-cells

Through the present simulations, it becomes possible to obtain the spatial profiles of the temperature rise. Neglecting heat outflow over the ultra-short, time scales, the maximum temperature rise, ΔT, can be calculated for each spatial segment as:

$$\Delta T = [\int_0^T \sigma(t)(E_\theta^2(t) + E_r^2(t))dt]/mc\ ], \tag{4.5.1}$$

where m is the mass of each cellular element, and c the specific heat. Fig. 31 shows the temperature distribution of a normal B-cell. The direction of external E-field is shown in this plot. A very high 225kv/cm intensity was chosen, with 1.5 ns rise and 10 ns fall times. Since the nuclear membrane is not porated, only displacement currents can flow through it. Consequently, the inner nucleus has the lowest temperature. Due to outer membrane poration, some conduction current does flow within the cytoplasm, giving rise to a slight temperature increase. However, the strongest change is predicted in the outer

suspension, with a hot spot of T~ 2 C. For the lower 100-kV/cm pulse, the peak temperature rise would be less than 0.4 C, signifying a virtual non-

Table 6 Result summary for Normal and Cancer cells.

Normal B-cell	**Outer membrane electroporated?**	**Inner Membrane electroporated?**
E: 15kv/cm, 5ns+10ns+5ns	No	No
E: 45kv/cm, 10ns+50ns+10ns	Yes	No
E: 100kv/cm, 10ns+50ns+10ns	Yes	No
Cancer B-cell (Farage)		
E: 15kv/cm, 5ns+10ns+5ns	No	No
E: 45kv/cm, 10ns+50ns+10ns	Yes	No
E: 100kv/cm, 10ns+50ns+10ns	Yes	Yes
E: 225kv/cm, 1.5ns+10ns+1.5ns	Yes	Yes

thermal condition. Fig. 32 shows that the temperature distribution in a cancer B-cell. It, however, is quite different. Due to poration, the hot spot occurs within the cytoplasm. This would be detrimental to cell viability. Thus, once again, we predict E-field induced damage to cancer cells.

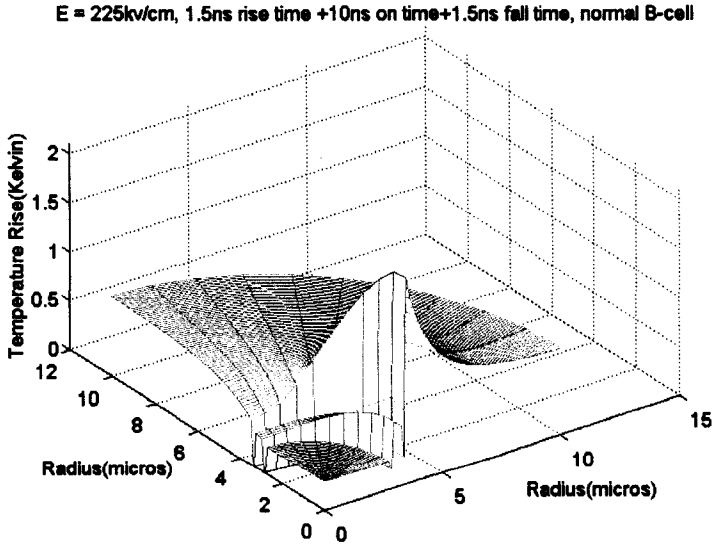

Fig. 31 Results of temperature change for normal cell.

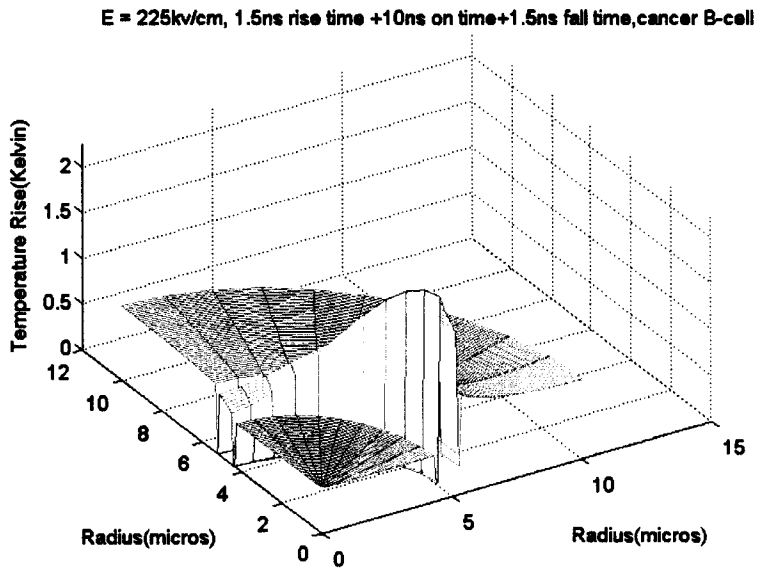

Fig. 32 Results of temperature change for cancer cell.

4.6 Molecular Dynamics

Simulations were carried out to probe the dynamics of molecular movement and possible pore formation at the membrane in response to an external electric field pulse. The L-J, ball-spring model described above was used for the phosphatidylcholine segments. Water molecules as well as a pair of positive and negative ions were included in the simulation. In order to avoid possible "recombination" effects, the ions were placed on opposite sides of the membrane. The membrane was taken to be "free-standing" and periodic boundary conditions were applied along the transverse direction. Results for a 100-kV/cm pulse of 0.6 ns duration are shown in Fig. 33. Though the actual pulse durations in on going experimental work is typically between 7 ns – 10 ns [123, 124], much shorter times were used here to alleviate the computational burden. The central goal was to gauge the qualitative trends, and to ascertain whether the model predictions were in keeping with actual observations.

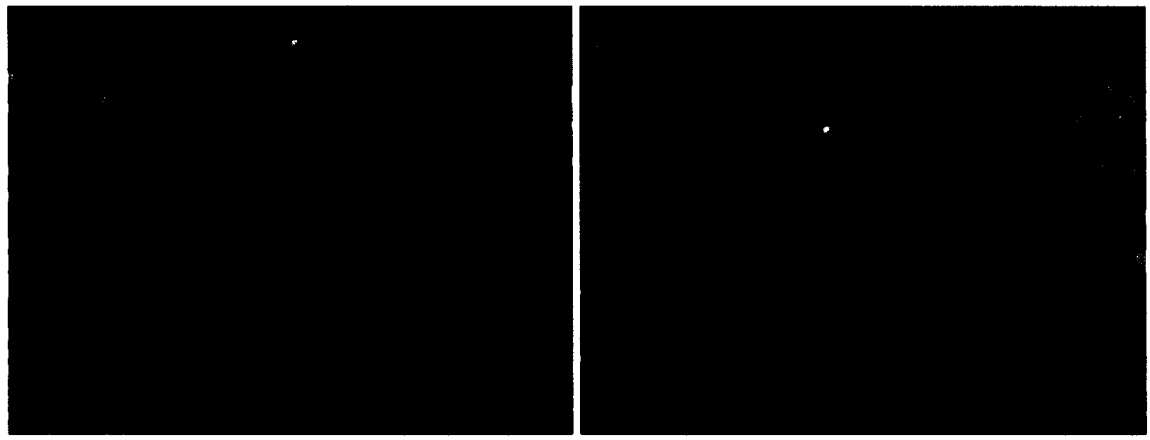

(a) Initial state (0.01ns) **(b) (~0.046ns)**

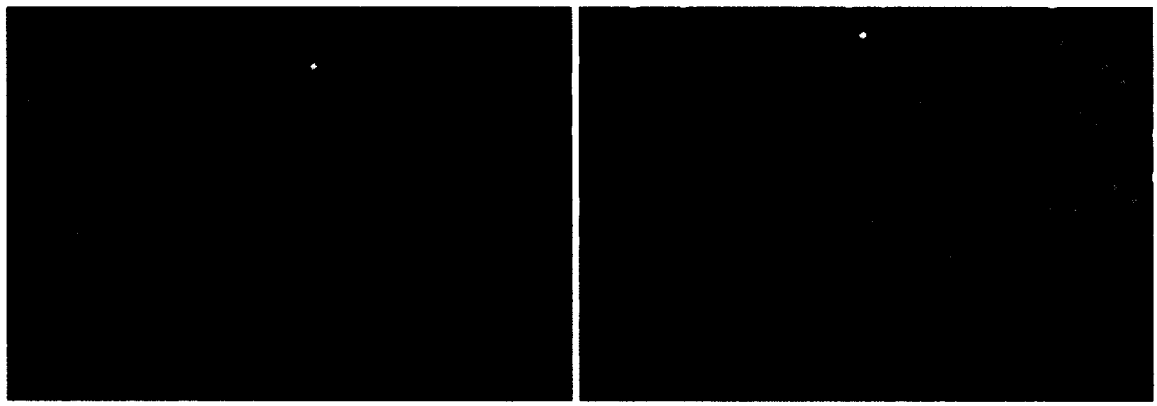

(c) (~0.075ns) (d) (~0.23ns)

(e) 0.6ns

Fig. 33 Snapshot of molecular arrangement. External E field is 0.01V/nm, and the pulse duration is 0.6ns. Lipids are red, water is blue, negative ion is yellow and positive ion is green.

Fig. 33(a) shows a snapshot of the molecular arrangement soon after the commencement of the external 0.6 ns pulse. The time instant is 0.01 ns, and lipid bilayer

exhibits a nearly uniform thickness of 5 nm, but with some flexibility due to the motion of the individual constituent atoms. The water molecules are almost entirely on the outside (upper and lower) regions. The positive ion (yellow) is at the top, while the negative green ion is shown to be below the membrane. The snapshot at time 0.046 ns shown in Fig. 33(b) reveals a slight distortion in the membrane structure, with a slight intrusion of the negative ion along with a few water molecules on the lower side. The ion is driven by the external electric field. The picture at a slightly longer 0.075 ns instant, shown in Fig. 33 (c), clearly demonstrates the inability of the ions to penetrate the lipid bilayer membrane. Despite the slight intrusion of the negative particle (as in Fig. 33 (b)), the ion was unable to pass through the membrane. The many-body L-J repulsion effectively served as a time-dependent energy barrier. At about 0.23 ns, a small nano-sized pore was seen to form as shown in Fig. 33 (d). This pore was permeable to water molecules. However, in this simulation (along with other simulations at lower fields, but not shown here), the ions were not able to either squeeze through the membrane or pass through the pore. Finally, Fig. 33 (e) at the last simulated time of 0.6 ns clearly shows a well-defined aqueous pore in the middle of the membrane. The lipid heads at the periphery of the pore are seen to have undergone a structural re-organization. The repulsive hydrophobic interaction between the water molecules and the lipid tails forces the heads to turn, forming a semi-circle at the two boundaries of the pore-lipid interface. Such rearrangement is in keeping with predictions made several years ago based on surface tension and energy minimization arguments [125, 126].

Unlike the previous treatments, however, the present approach affords a full dynamical treatment. It clearly shows that nano-pores in biological membranes can form

in response to a high external electric field within 1.0 ns. The results also demonstrate that despite the pore formation at the high electric field of 100 kV/cm, a large ion throughput is not necessary. This is due in part to the relatively low density of ions within the aqueous media. Furthermore, the relatively small size of the pore (nanoscale dimensions) and the dipole drag of water molecules prevent easy ionic pass-through. It might be pointed out, however, that our simulations were carried out only for a relatively short 0.6 ns time frame, and does not discount the possibility of ion transport at later times. This result suggests an upper bound of about 0.26 nA [$=(1.6 \times 10^{-19})/(0.6 \times 10^{-9})$] on the current throughput during the initial pore-formation stage. For the actual times of 7-10 ns, it is quite likely that some ions would be able to pass through the membrane. However, it appears that their flux is likely to be relatively low. Finally, our results predict that larger molecules would be unlikely to pass through the membrane in response to the nanosecond electric pulses. This is in keeping with the actual observations of negligible Propidium Iodide (PI) throughput in various cells under such pulsed conditions [127, 128]. The relatively large radius of PI (roughly 0.6 nm), coupled with its relatively low concentration, would make it difficult to allow for a rapid influx. We predict that since the nano-pores remain open for a relatively long time, a slow diffusion inflow would be possible over extended time scales. Such slow and gradual uptake of PI has been observed.

Simulations at zero electric were also carried out as a validity test of the present numerical approach. One expects almost no pore formation or any throughput of water. This was bourn out in the results of Fig. 34. The location of the membrane atoms and the

water molecules after 0.01 ns from the start of the simulations is shown in Fig. 34(a). The fluctuation of the freestanding membrane arising from the random thermal

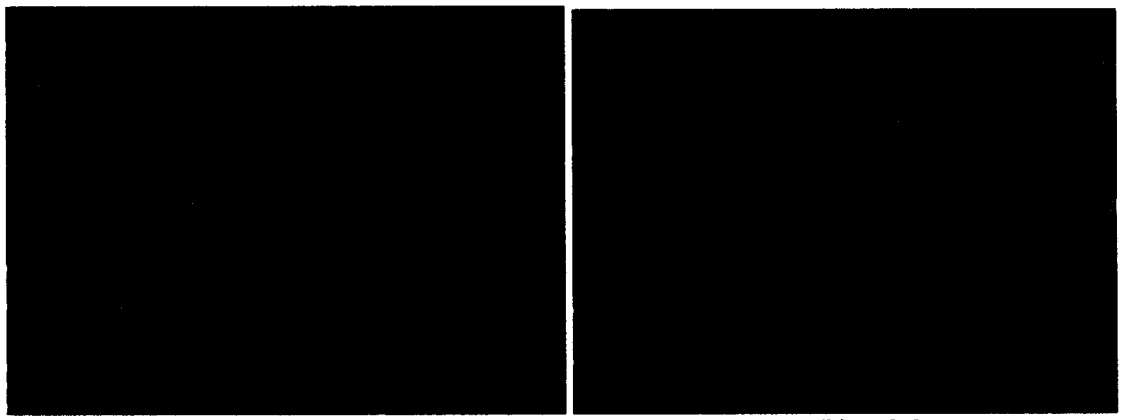

(a) ~0.01ns (b) ~ 0.2ns

Fig. 34 Snapshots: no pore forms and no water molecules go through the membrane. No external E field. Water molecules are blue and PCs are red.

velocities and collective L-J interactions is obvious. The picture at a later 0.2 ns instant shows a slight change in membrane shape without the formation of an internal water channel.

Results at the higher electric field intensity of 500 kV/cm are given in Fig. 35. The general trend towards a single pore formation is similar to that obtained in Fig. 33. However, the pore forms a little faster due to the larger electric field. For example, a near final steady state is predicted after only about 0.3 ns (Fig. 35d), unlike the much longer 0.6 ns needed for 100 kV/cm as in Fig. 33 (e). This is indicative of the role of ions in the aqueous medium and their associated cloud of water molecules. Since the membrane was assumed to be charge neutral, there should not have been any difference in the pore formation otherwise. Also, at this large electric field, the ions were clearly seen to pass through the membrane. For example, the negative ion (green sphere) is seen to move up through the membrane starting before 0.026 ns (Fig. 35b) and emerges at the opposite end at about 0.029 ns (Fig. 35c). However, it may be pointed out that in practical

experiments, such large average electric fields of 500 kV/cm have not been applied. Also, the entry of water molecules upon membrane pore formation would work to restrict the local electric fields due to the increased relative permittivity of the aqueous medium. In any case, one charge was seen to pass through the membrane during the first 0.03 ns. This corresponds to an average current throughput of about 5 nano-Amperes or lower. This value is roughly in agreement with reported measurements [129, 130].

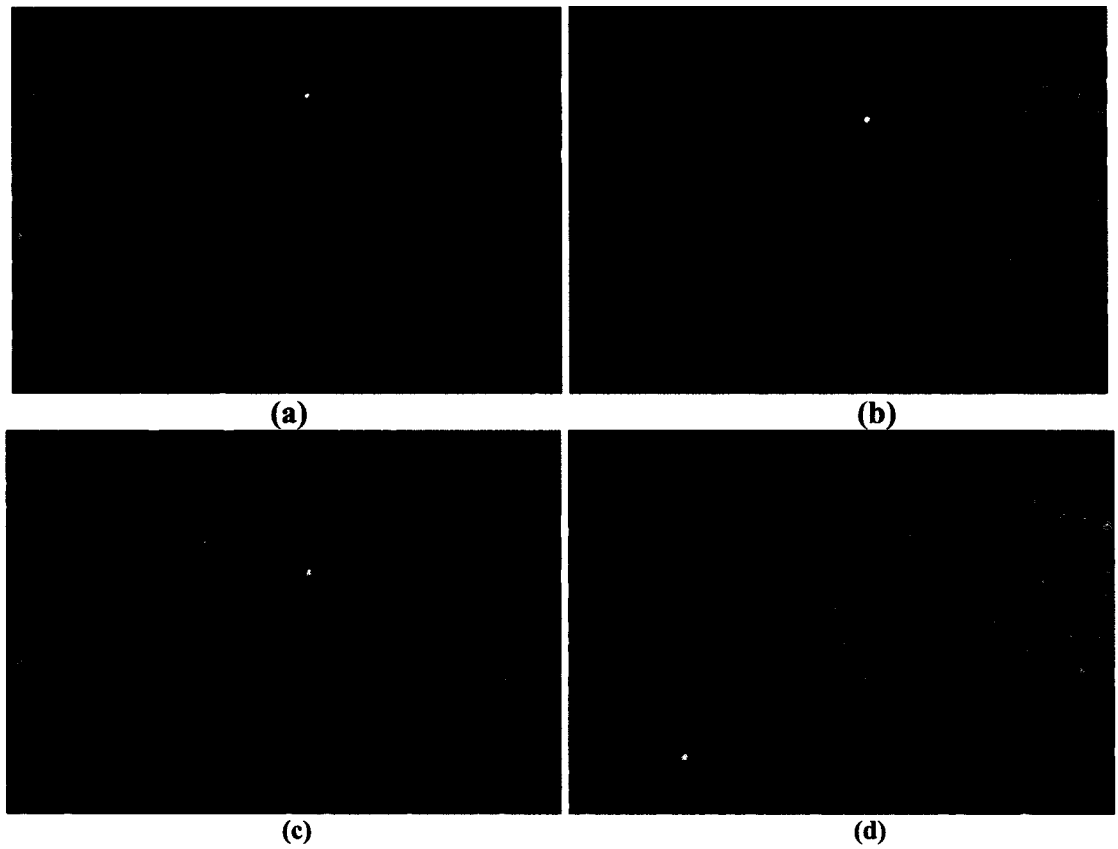

Fig. 35 Snapshots: Small pore forms and water molecules go through it. The E field is 0.05V/nm, and pulse duration is 0.3ns. (a) Initial state (0.01ns); (b) Negative ion starts go in the membrane (0.026ns); (c) 0.029ns; (d) ~0.3ns

A final issue addressed here based on the simple ball-spring, L-J model pertains to PS externalization. Experiments involving Jurkat cells [128]-[131] exposed to nanosecond electric pulses (~7ns-10ns) have revealed a field-induced externalization of

phosphatidylserine from the inner to the outer leaflet of the cells. Electric fields of about 100 kV/cm were seen to be sufficient for the PS externalization. Since PS is a charged phospholipid, the electric field is expected to provide a strong driving force for this translocation. However, the exact mechanism is not entirely clear, and following two possible scenarios exist. (i) Either the PS is pushed outwards by the electrostatic force, and emerges on the outer leaflet by overcoming the repulsive interactions of the neighboring lipids. This would correspond to field-assisted PS "drive-through", and require overcoming the internal activation energy barrier. (ii) A second possibility involves a pore-mediated event, with the PS molecule diffusing out through pores that might first be formed at the cell membrane by the external field. As already shown here (Fig. 33), a membrane nano-pore can form at the 100-kV/cm field. Hence, diffusion through the pore is a certainly a possibility. Also, simple arguments can be put forth against the P drive-through scenario. For example, the maximum energy gain for a singly charged PS molecule would take place under totally non-dissipative conditions. This energy gain during the course of a ~5 nm transmembrane movement at a 100 kV/cm field would roughly be 0.05 eV. However, the activation barrier for translocation is known to be about 100 kJ/mol or 1.0 eV [131], and hence, discounts the drive-through scenario. Also physically, a translocation of PS in the absence of pore formation would lead to strong membrane distortion, as the neighboring molecules would not have much space to maneuver and relax the internal perturbation. Here, we use our numerical model to demonstrate that a simple "drive-through" of the PS molecule that overcomes the internal energy barrier, is not possible at fields of 100 kV/cm or even 200 kV/cm. Instead, the

pore formation followed by PS diffusion at much later times, appears to be the natural process.

Simulation results at a 200-kV/cm field for a cell membrane containing one PS segment (green chain) on the inner leaflet embedded between phosphatidylcholine lipids are shown in Fig. 36. A higher field of 200 kV/cm (rather than 100 kV/cm) was deliberately used to emphasize that a PS drive-through movement could not possibly be achieved. The configuration at a relatively early time of 0.02 ns is given in Fig. 36(a). Some general fluctuations associated with molecular motion are evident. The snapshot at 0.081 ns reveals the beginning of a pore on the right side. The PS is seen to have moved

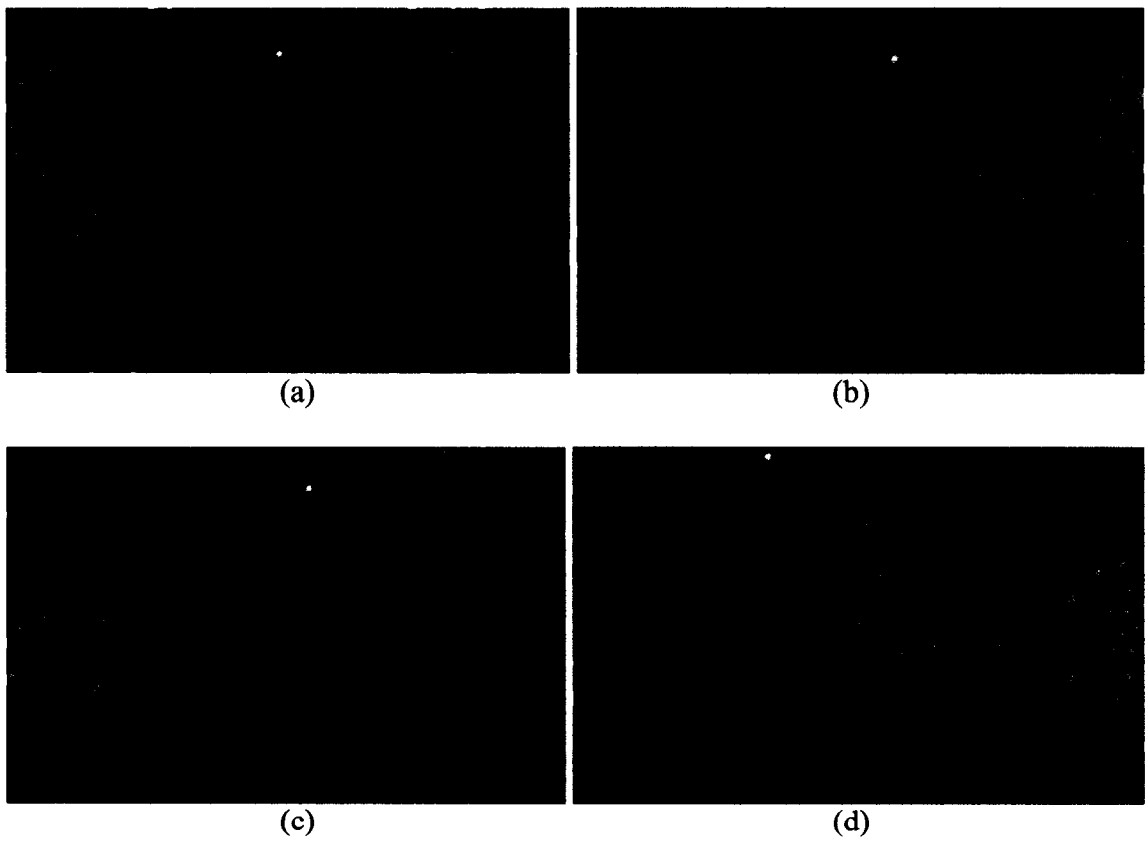

Fig. 36 Snapshots: ps is on the inner leaflet and cannot be externalized under high external field. The E field is 200kV/cm, and the pulse duration is 0.3ns. (a) ~0.02ns, (b) ~0.081ns), (c) ~0.161ns, (d) ~ 0.20ns.

up slightly due to the electrostatic force from the external field. In Fig. 36(c) after 0.16 ns, the pore on the right has nearly formed. The head groups of adjacent PC segments begin to rotate and form a boundary on either side of the pore. The PS is seen to remain at the bottom half, and besides causing a slight membrane distortion, does not move much. Finally, after 0.2 ns in Fig. 36(d), a near steady state is reached. The PS has not translocated, and merely produces a slight upward shift of the membrane due to the electrostatic force on its charged lipid head. While not shown, it is expected that after much longer times, the PS could well diffuse and externalize by passing through the pore to its right.

CHAPTER V

CONCLUSIONS AND FUTURE RESEARCH

5.1 Research Summary of High-Intensity Nano-pulsed Electroporation

In this study, an improved model that includes a dependence of pore population and density on the pore formation energy was presented. The model also allowed for variable surface tension, and incorporated the effects of finite conductivity on the electrostatic correction term. Finally, the model developed and implemented was dynamic in nature, through its dependence on both the cell voltage and pore density. It has been shown that this will lead to temporal variations in the magnitude and profile of $E(r)$. Such a mechanism makes $E(r)$ self-adjusting in response to pore formation, without causing uncontrolled growth and expansion. Self-consistent calculations based on a coupled scheme involving the Smoluchowski equation and the improved energy model has been carried out. The results demonstrate the effects of external electrical voltages on the pore dynamics. In principle, this theory can be augmented to include pore-pore interactions to move beyond the independent pore picture. It must also be mentioned that the actual membrane potential is more likely to be the sum of exponentials. This would inherently arise from the ''charging'' and ''discharging'' phenomena associated with the inductive and capacitive elements inherent to the cell suspension and the external circuitry. Such circuit and distributed effects were ignored in the present study, as the intent was simply to present an improved fundamental model for the energy function $E(r)$.

This study was aimed at providing a simple, but physical model for cell irreversibility and apoptosis in response to an ultrashort (nanosecond), high-intensity

electric pulse. In view of the collective evidence on cell death and its link to an electrical stimulation, apoptotic behavior may be the result of irreversible conformational changes at the inner mitochondrial membrane. Such changes are likely to be driven by the high electric fields that arise from strong transient increases in transmembrane potentials. This was shown more quantitatively in the Smoluchowski and distributed circuit-based models developed in this study.

The study also focused on the possible mechanism and qualitative predictions of the observed pulse-width dependence on cell irreversibility. A comprehensive and accurate treatment of this problem is extremely difficult and challenging given that apoptosis can have several pathways, the sequential details of the bio-physics are not well known, and neither are the magnitudes of the internal energies and configurations. Given the various difficulties, the present model merely attempted to provide a possible physical picture that was dependent only on the electrical trigger, and captured the essence of the experimentally observed pulse-width dependence.

The time dependent current model developed here was probabilistic through the use of the Smoluchowski equation and coupled a distributed electrical model for current flow to provide the trans-membrane voltages. The results agreed with the observed experimental data very well. Based on the present model, it becomes possible to predict a number of interesting features. (i) First, cell irreversibility at a fixed input energy will depend on the pulse width, and is likely to have an optimal range. Pulses that are very short would not have a significant effect due to insufficient durations for electric field driven conformational changes. On the other hand, much slower and longer pulses would also be rendered ineffective due to their inability to penetrate the membranes of the inner

organelles and develop a significant trans-membrane voltage. (ii) The electrical effects are likely to be cumulative and to exhibit a memory effect, provided successive pulses were to be applied with delay times less than that required for complete recovery. Such a memory effect has indeed been noted in the context of the ultrashort, high-intensity pulsing. (iii) The inherent probabilistic basis of this model implies that complete and total killing of cell populations can never be achieved by a single shot exposure. There will always be a finite probability distribution below the threshold because of the diffusive motion in energy space. Only at very low temperatures might one expect cohesive and "ballistic" motion. This prediction of incomplete killing is in keeping with experimental observations. (iv) Further more, the present model predicts that the use of very high electric field intensities may not necessarily have a significantly larger impact. This naturally follows since not only is the pulse duration an important factor, but also because the transmembrane potential would not scale with the applied field. Electroporation and dynamic changes in conductivity would work to offset the impact of larger external fields. (v) Next, the irreversibility mechanism is taken to arise from fixed charge and dipole movements brought about within the membrane by the electrostatic driving force produced by the large transient transmembrane potentials. Consequently, excitation processes that cannot generate large electric fields at membranes, or if their time durations are small, might not be very effective in electrically triggering apoptotic behavior in cells. For example, under "contactless" conditions, or for microwave and radio frequency excitation, cellular apoptosis may be expected to be fairly negligible.

5.2 Future Trends and Possible Follow-On Work

Some qualitative trends were obtained for the pulse-width dependence based on a simple energy landscape picture. In theory, more refined estimates and quantitative predictions might be possible by incorporating a better energy description of the membrane system. A first step might be the use of randomly correlated energy models, as first proposed by Derrida [131]. Refinements to include correlation effects, is an interesting possibility as has been shown recently in the context of hetero-polymers [133].

Some of the other areas of future research include the following aspects:

(i) The development and analysis of bio-electric effects at the cellular level based on atomic level simulations of the membrane system. The advantages and need for such microscopic modeling over that of a continuum approach arises for the following reasons: (a) Breakdown of equilibrium theories over the ultrafast time scales. (b) The use of static potential barriers to ion transport and the use of the "free-energy" concept that is only restrictive. Also, mean-field approach can be expected to be inadequate for treating such a nanoscale system. (c) The assumption of circular, well-behaved static pores. In general, due to the random fluctuation of the membrane molecules, the pore formation will be dynamic and could have arbitrary geometric shapes. (d) The need to allow for fluctuations and noise. Experimental observations of membrane currents have shown "burst-like" behavior, rather than a continuous movement. (e) The need to include microscopic structure and spatial defects such as embedded proteins.

(ii) Treatment of ion and molecular transport across both cell and artificial bio-membranes based on microscopic, Molecular Dynamics simulations. Such analysis would be very useful for direct comparisons with the experimental data on the throughput of fluorescent dye molecules such as Propidium Iodide (PI). For example, experimental data suggests that PI uptake is not very significant in response to the nanosecond pulses. On the other hand, it would seem that simpler mono-valent and divalent ions such as Na^{+} and Ca^{+2} can pass through the cell membrane much more rapidly. The reasons for such disparity and quantitative comparisons would be interesting future endeavors.

(iii) Similarly, field-assisted transport of bio-molecules and genetic material through cells would also be useful from the standpoint of drug delivery.

(iv) Also, Phosphotidyl-serine (PS) externalization is believed to be tightly related to cellular apoptosis. It would, therefore, be useful to model this process for a better understanding of apoptosis.

Reference

[1] M. Ismail. Hafez and Pieter R. Cullis, Advanced Drug Delivery Reviews, **47**, 14839 (2001).

[2] S. Banerjee, P.Nandy, Physica A, **297**, 26 (2001).

[3] G. A Hofmann, S. B. Dev, S. Dimmer, G. S. Nanda, IEEE Transactions on Bio-Medical Engineering, **46**, 752 (1999).

[4] W. R. Panje, N. Sadeghi, American Journal of Rhinology, **14,** 187 (2000).

[5] S. B. Dev, F. J. Giordano, D. L. Brown, Proceedings of The 3rd US.-Japan Symposium on Drug Delivery Systems Abstract #**38**, 43 (1995).

[6] N. Vazquez-Laslop, H. Lee, R. Hu, A. A. Neyfakh, J. Bacteriology, **183**, 2399 (2001).

[7] B. K. Pai and H. D. Wymann, J. Biomechanics, **13**, 105 (1980).

[8] R. P. Joshi and K. H. Schoenbach, Phys, Rev. E, **6**, 1033 (2000).

[9] G. Saulis, Biophys, J. **73**, 1299, (1997).

[10] R. W. Glaser et al., S. L. Leikin, L. V. Chernomordik, V. F. Pastushenko, and A. I. Sokirko, Biochim. Biophys. Acta **940**, 275, (1988).

[11] T. Y. Tsongi, Biophys. J., **60**, 297 (1991).

[12] M. J. Jaroszeski, R. A. Gilbert, R. Heller, Advance Drug Delivery Reviews **26,** 185 (1997).

[13] A. Barnett, and J. C. Weaver, Bioelectrochem, Bioenerg. **25**, 163 (1991).

[14] J. W. Ashe, D. K. Bogen, and S. Takashima, Ferroelectrics, **86**, 311 (1988).

[15] Edited by M.Blank and I. Vodyanoy, Biomembrane Electrochemistry, American Chemical Society, Washington, DC, (1994).

[16] M. Golzio, M. P. Mora, C. Raynaud, C. Delteil, J. Teissie, and M. P. Rols, Biophys, Journ., **74**, 3015 (1998).

[17] Allen, T. W., S. Kuyucak, and S. H. Chung., Biophys, J. **77**, 2502 (1999).

[18] W. Im, S. Seefeld, and B. Roux, Biophys, J. **79**, 788 (2000).

[19] K. H. Schoenbach, S. J. Beebe, and E. S. Buescher, Bioelectromagnetics, **22**, 440 (2001).

[20] R. P. Joshi, Q. Hu, R. Aly, K. H. Schoenbach, and H. P. Hjalmarson, Phys. Review E, **64**, 11913-01 (2001).

[21] K. H. Schoenbach, F. E. Peterkin, R. W. Alden, and S. J. Beebe, IEEE Trans. Plasma Science, **25**, 284 (1997).

[22] H. Huelsheger, J. Potel, and E. G. Niemann, Radiat. Environ. Biophys., **20**, 53 (1981).

[23] U. Zimmermann and G. A. Neil, Electromanipulation of Cells. (Boca Raton, FL:CRC, 1996).

[24] U. Zimmermann, G. Pilwat, and F. Riemann, *Z.* Naturforsch, **29c**, 304 (1974).

[25] J. C. Weaver, IEEE Trans. Plasma Science, **28**, 24 (2000).

[26] M. M. Lo, T. Y. Tsong, M. K. Conrad, S. M. Strittmatter, L. D. Hester, and S. H. Snyder, Nature, **310**, 792 (1984).

[27] U. Karsten, P. Stolley, I. Walther, G. Papsdorf, S. Weber, K. Conrad, L. Pasternak, and J. Kopp, Hybridoma, 7, 627 (1988).

[28] A. K. Banga, and M. R. Prausnitz, Trends In Biotechnology, **16**, 408 (1998).

[29] E. Eksioglu-Demiralp, S. Kitada, D. Carson, J. Garland, A. Andreef, and J. C. Reed, Journal of Immunological Method, **275**, 41 (2003).

[30] M. F. Kalady, M. W. Onaitis, K. M. Padilla, S. Emani, D. S. Tyler, and S. K. Pruitt, Surgical Forum, **52**, 225 (2001).

[31] G. Mellitzer, M. Hallonet, L. Chen, and S. L. Ang, Mechanisms of Development, **118**, 57 (2002).

[32] L. Zhang, L. Li, G. Hoffmann, and R. Hoffman, Biochemical and Biophysical Research Communications, **220**, 633 (1996).

[33] R. L. Harrison, B. J. Byrne, and L. Tung, FEBS Lett., **435**, 1 (1998).

[34] R. Langer, *Nature*, **392**, S5 (1998).

[35] H. Mekid, and L. M. Mir, Biochem Biophys. Acta, **1524**, 118 (2001).

[36] C. Ramos and J. Teissie, Biochimie, **82**, 511 (2000).

[37] K. H. Schoenbach, R. P. Joshi, R. H. Stark, F. C. Dobbs, and S. J. Beebe, IEEE Trans. Dielectrics & Electrical Insulation, **7**, 637 (2000).

[38] A. J. H. Sale and W. A. Hamilton, Biochem Biophys. Acta, **148**, 781 (1967).

[39] A. J. H. Sale and W. A. Hamilton, Biochem Biophys. Acta, **163**, 37 (1968).

[40] S. Sixou and J. Teissie, Biochem Biophys. Acta, **1028**, 154 (1990).

[41] K. Hughes and N. Crawford, Biochim. Biophy. Acta, **981**, 277 (1989).

[42] U. Broggemann, E. C. Roux, J. Hanning, and C. Nicolau, Transfusion, **35**, 478 (1995).

[43] M. Zeira, P. Tosi, Y. Mouneimne, J. Lazarte, L. Sneed, D. J. Volsky, and C. Nicolau, Proc. Natl. Acad. Sci., **88**, 4409 (1991).

[44] L. M. Mir, S. Orlowski, J. Belehradek, and C. Paoletti, European Journal Of Cancer, **27**, 68 (1991).

[45] M. Okino and H. Mohri, European Journal Of Cancer, **27**, 68 (1991).

[46] S. J. Beebe, P. M. Fox, L. J. Rec, L. K. Willis, and K. H. Schoenbach, FASEB Journal, 17, 1493 (2003).

[47] J. Deng, K. H. Schoenbach, E. S. Buescher, P. S. Hair, P. M. Fox, and S. J. Beebe, Biophysical Journal, **84**, 2709 (2003).

[48] S. J. Beebe, P. M. Fox, L. J. Rec, K. Somers, R. H. Stark, and K. H. Schoenbach, IEEE Transactions on Plasma Science, **30**, 286 (2002).

[49] S. A. Susin, N. Zamzami, and G. Kroemer, Biochem Biophys. Acta, **1366**, 151 (1998).

[50] A. P. Halestrap and C. Brenner, Current Medical Chemistry, **10**, 1507 (2003).

[51] A. P. Halestrap, G. P. McStay, and S. J. Clarke, Biochimie, **84**, 153 (2002).

[52] M. Crompton, Biochem. J., **341**, 233 (1999).

[53] G. Kroemer and J. C. Reed, Nat. Med., **6**, 513 (2000).

[54] V. P. Skulatchev, *Membrane Bioenergetics*, (Berlin: Springer-Verlag, 1988).

[55] V. Petronilli, D. Penzo, L. Scorrano, P. Bernardi, and F. Di Lisa, The Journal of Biological Chemistry. **276**, 12030 (2001).

[56] D. Tyler, *The Mitochondrion In Health And Disease*, (New York: VCH Publishers, 1992).

[57] F. Ichas and J. P. Mazat, Biochim. Biophys. Acta. **1366**, 33 (1998).

[58] L. Scorrano, V. Petronilli, and P. Bernardi, The Journal of Biological Chemistry. **272**, 12295 (1997).

[59] J. C. Weaver and Yu. A. Chizmadzhev, Bioelectrochem. Bioenerg. **41**, 135 (1996).

[60] I. G. Abidor, V. B. Arakelyan, L. V. Chernomordik, Y. A. Chizmadzhev, V. F. Pastushenko, and M. R. Tarasevich, Bioelectrochem. Bioenerg. **6**, 37 (1979).

[61] C. Taupin, M. Dvolaitzky, and C. Sauterey, Biochim **14A**, 4771 (1975).

[62] J. C. Weaver and R. A. Mintzer, Phys. Lett. **86A**, 57 (1981).

[63] M. Hoyles, S. Kuyucak, and S. H. Chung, Biophys. J. **70**, 1628(1996).

[64] A. Parsegian, Nature (London) **221**, 844 (1969).

[65] J. C. Weaver, Ann. Acad. Sci. **720**, 141 (1994).

[66] J. C. Neu and W. Krassowska, Phys. Rev. E **59**, 3471 (1999).

[67] H. Isambert, Phys. Rev. Lett. **80**, 3404 (1998).

[68] M. Winterhalter and W. Helfrich, Phys. Rev. A **36**, 5874 (1987).

[69] I. P. Sugar, Biochim. Biophys. Acta **556**, 72 (1979).

[70] W. Sung and P. J. Park, Biophys. J. **73**, 1797 (1997).

[71] C. Grosse and H. P. Schwan, Biophys. J. **63**, 1632 (1992).

[72] K. A. DeBruin and W. Krassowska, Biophys. J. **77**, 1213 (1999).

[73] D. Gross, L. M. Loew, and W. W. Webb, Biophys. J. **50**, 339 (1986).

[74] Z. Lojewska, D. L. Farkas, B. Ehrenberg, and L. M. Loew, Biophys. J. **56**, 121 (1989).

[75] For example, J. D. Jackson, *Classical Electrodynamics* (Wiley, New York, 1962).

[76] E. Neumann, S. Kakorin, and K. Toensing, Faraday Discuss. **111**, 111 (1998).

[77] I. P. Sugar, in *Electroporation And Electrofusion In Cell Biology*, pp. 97–110.

[78] G. Saulis, Biophys. J. **73**, 1299 (1997).

[79] D. V. Zhelev and D. Needham, Biomembranes **1147**, 89 (1993).

[80] O. Sandre, L. Mareaux, and F. Brochard-Wyart, Proc. Natl. Acad. Sci. U.S.A. **96**, 10 591 (1999).

[81] D. C. Chang and T. S. Reese, Biophys. J. **58**, 1 (1990).

[82] H. Isambert, Phys. Rev. Lett. **80**, 3404 (1998).

[83] F. Brochard-Wyart, P. G. de Gennes, and O. Sandre, Physica A **278**, 32 (2000).

[84] V. F. Pastushenko and Yu. A. Chhizmadzhev, Biofizika **28**, 1036 (1983); V. F. Pastushenko and Yu A. Chhizmadzhev, Biofizika **27**, 475 (1982).

[85] A. Barnett and J. C. Weaver, Bioelectrochem. Bioenerg. **25**, 163 (1991).

[86] S. A. Freeman, M. A. Wang, and J. C. Weaver, Biophys. J. **67**, 42 (1994).

[87] V. A. Parsegian, Nature (London) **221**, 844 (1969).

[88] E. M. Renkin, J. Gen. Physiol. **38**, 225 (1954).

[89] J. Israelachvili, *Intermolecular And Surface Forces*, 2nd ed. (Academic, London, 1992).

[90] W. Flugge, *Stresses In Shells*, 2nd ed. (Springer, Berlin, 1962.

[91] N. Eynard, F. Rodriguez, J. Trotard, and J. Teissie, Biophys. J. **75**, 2587 (1998).

[92] E. A. Evans and R. Skalak, *Mechanics And Thermodynamics of Biomembranes* CRC, Boca Raton, 1980.

[93] J. C. Hansen, R. Skalak, S. Chien, and A. Hoger, Biophys. J. **72**, 2369 (1997).

[94] S. K. Boey, D. H. Boal, and D. E. Discher, Biophys. J. **75**, 1573 (1998).

[95] For example, J. Van Bladel, *Electromagnetic Fields* (McGraw-Hill, New York, 1964).

[96] For example, *Structure And Dynamics of Membranes*, edited by R. Lipowsky and E. Sackmann (Elsevier, Amsterdam, 1995).

[97] E. Chacon, A. M. Somoza, and P. Tarazona, J. Chem. Phys. **109**, 2371 (1998).

[98] M. Wortis, M. Jaric, and U. Seifert, J. Mol. Liq. **71**, 195 (1997).

[99] H. Grubmuller, B. Heymann, and P. Tavan, Science **271**, 997 (1996).

[100] P. S. Crozier, R. L. Rowley, N. B. Holladay, D. Henderson, and D. Busath, Phys. Rev. Lett. **86**, 2467 (2001).

[101] T. W. Allen, A. Bliznyuk, A. P. Rendell, S. Kuyucak, and S. H. Chung, J. Chem. Phys. **112**, 8191 (2000).

[102] W. Im and B. Roux, J. Mol. Biol. **319**, 1177 (2002).

[103] E. Lindahl and O. Edholn, Biophys. J. **79**, 426 (2000) ; E. Lindahl and O. Edholn, J. Chem. Phys. **113**, 3882 (2000).

[104] J. C. Shelley, M. Y. Shelley, R. C. Reeder, S. Bandyopadhyay, and M. L. Klein, J. Phys. Chem. B **105**, 4464 (2001).

[105] R. Goetz, G. Gompper, and R. Lipowsky, Phys. Rev. Lett. **82**, 221 (1999).

[106] O. Farago, J. Chem. Phys. **119**, 596 (2003).

[107] G. K. Bourov and A. Bhattacharya, J. Chem. Phys. **119**, 9219 (2003).

[108] E.Spohr, J. Electroanalytical Chem. 450, 327 (1998).

[109] H. J. C. Berendsen, J. R. Grigera, and T. P. Straatsma, J. Phys. Chem. **91**, 6269 (1987).

[110] H. J. C. Berendsen, J. P. M. Postma, W. F. van Gunsteren, A. DiNola, and J. R. Haak, J. Phys. Chem. **81**, 3684 (1984).

[111] S. E. Feller and R. W. Pastor, Biophys. J. **71**, 1350 (1996).

[112] S. I. Sukharev, P. Blount, B. Martinac, F. R. Blattner, and C. Kung, Nature (London) **368**, 265 (1994).

[113] T. Benachir and M. Lafleur, Biophys. J. **70**, 831 (1996).

[114] S. R. James, R. A. Demel, and C. P. Downes, Biophys. J. **298**, 499 (1994).

[115] W. Meier, A. Graff, A. Diederich, and M. Winterhalter, Phys. Chem. Chem. Phys. **2**, 4559 (2000).

[116] D. C. Chang and T. S. Reese, Biophys. J. **58**, 1 (1990).

[117] I. Tsoneva, T. Tomov, L. Panova, and D. Strahilov, Bioelectrochem. Bioenerg. **24**, 41 (1990).

[118] H. Isambert, Phys. Rev. Lett. **80**, 3404 (1998).

[119] H. J. Deuling and W. Helfrich, J. Phys. (France) **37**, 1335 (1976).

[120] D. C. Pamplona and C. R. Calladine, J. Biomed. Eng. **115**, 149 (1993).

[121] E. Neumann, S. Kakorin, and K. Toensing, Faraday Discuss. **111**, 111 (1998).

[122] I. Ermolina, Y. Polevaya, Y. Feldman, and M. Schlesinger, IEEE Trans. On Dielectrics and Electrical Insulation, Vol. 8, 253 (2001).

[123] J. Deng, K. H. Schoenbach, E. S. Buescher, P. S. Hair, P. M. Fox, and S. J. Beebe, Biophysical Journal **84**, 2709 (2003).

[124] P. T. Vernier, Y. Sun, L. Marcu, S. Salemi, C. M. Craft, and M. A. Gundersen, Biochemical and Biophysical Research Communications **310**, 286 (2003).

[125] J. C. Weaver and R. A. Mintzer, Phys. Lett. A **86**, 57 (1981).

[126] I. G. Abidor, V. B. Arakelyan, L. V. Chernomordik,Y. A. Chizmadzhev, V. F. Pastushenko, and M. R. Tarasevich, Bioelectrochem. Bioenerg. **6**, 37 (1979).

[127] K. H. Schoenbach, R. P. Joshi, R. H. Stark, F. C. Dobbs, and S. J. Beebe, IEEE Trans. Dielectrics & Electrical Insulation **7**, 637 (2000).

[128] S. J. Beebe, P. M. Fox, L. J. Rec, K. Somers, R. H. Stark, and K. H. Schoenbach, IEEE Transactions on Plasma Science **30**, 286 (2002).

[129] V. F. Pastushenko and Y. A. Chizmadzhev, Gen. Physiol. Biophys. **1**, 43 (1982).

[130] A. Barnett and J. C. Weaver, Bioelectrochem. Bioenerg. **25**, 163 (1991).

[131] P. T. Vernier, Y. Sun, L. Marcu, C. M. Craft, and M. A. Gundersen, accepted for publication, Biophysical Journal, to appear 2004.

[132] B. Derrida, *Phys. Rev. B.*, Vol. 24, pp. 2613 (1981).

[133] S. S. Plotkin, J. Wang, and P. G. Wolynes, *Phys. Rev. E.*, Vol. 53, pp. 6271 (1996).

Appendix

If we put the area of each face in Eqn. (3.5.4), it becomes:

$$\sigma_1 \frac{V^t_{i-1,j} - V^t_{i,j}}{\Delta r} * (r + \Delta r/2)^2 (\cos(\theta - \Delta\theta/2) - \cos(\theta + \Delta\theta/2)) +$$
$$\sigma_2 \frac{V^t_{i+1,j} - V^t_{i,j}}{\Delta r} * (r - \Delta r/2)^2 (\cos(\theta - \Delta\theta/2) - \cos(\theta + \Delta\theta/2)) +$$
$$\sigma_3 \frac{V^t_{i,j-1} - V^t_{i,j}}{\Delta\theta} \Delta r \sin(\theta - \Delta\theta/2) + \sigma_4 \frac{V^t_{i,j+1} - V^t_{i,j}}{\Delta\theta} \Delta r \sin(\theta + \Delta\theta/2) +$$
$$\frac{\varepsilon_1}{\Delta t}\left[\frac{V^{t+1}_{i-1,j} - V^{t+1}_{i,j}}{\Delta r} - \frac{V^t_{i-1,j} - V^t_{i,j}}{\Delta r}\right](r + \Delta r/2)^2 (\cos(\theta - \Delta\theta/2) - \cos(\theta + \Delta\theta/2)) + \qquad \text{(A.1)}$$
$$\frac{\varepsilon_2}{\Delta t}\left[\frac{V^{t+1}_{i+1,j} - V^{t+1}_{i,j}}{\Delta r} - \frac{V^t_{i+1,j} - V^t_{i,j}}{\Delta r}\right](r - \Delta r/2)^2 (\cos(\theta - \Delta\theta/2) - \cos(\theta + \Delta\theta/2)) +$$
$$\frac{\varepsilon_3}{\Delta t}\left[\frac{V^{t+1}_{i,j-1} - V^{t+1}_{i,j}}{\Delta\theta} - \frac{V^t_{i,j-1} - V^t_{i,j}}{\Delta\theta}\right]\Delta r \sin(\theta - \Delta\theta/2) +$$
$$\frac{\varepsilon_4}{\Delta t}\left[\frac{V^{t+1}_{i,j+1} - V^{t+1}_{i,j}}{\Delta\theta} - \frac{V^t_{i,j+1} - V^t_{i,j}}{\Delta\theta}\right]\Delta r \sin(\theta + \Delta\theta/2) = 0$$

For nodes on the outer side and the inner side of each membrane, equation (A.1) will be slightly different. On the outer side of each membrane, (A.1) is changed into:

$$\sigma_o \frac{V^t_{i-1,j} - V^t_{i,j}}{\Delta r} * (r + \Delta r/2)^2 (\cos(\theta - \Delta\theta/2) - \cos(\theta + \Delta\theta/2)) +$$
$$\sigma_m \frac{V^t_{i+1,j} - V^t_{i,j}}{\Delta r} * (r - \Delta r/2)^2 (\cos(\theta - \Delta\theta/2) - \cos(\theta + \Delta\theta/2)) +$$
$$\sigma_{avg} \frac{V^t_{i,j-1} - V^t_{i,j}}{\Delta\theta} \Delta r \sin(\theta - \Delta\theta/2) + \sigma_{avg} \frac{V^t_{i,j+1} - V^t_{i,j}}{\Delta\theta} \Delta r \sin(\theta + \Delta\theta/2) +$$
$$\frac{\varepsilon_o}{\Delta t}\left[\frac{V^{t+1}_{i-1,j} - V^{t+1}_{i,j}}{\Delta r} - \frac{V^t_{i-1,j} - V^t_{i,j}}{\Delta r}\right](r + \Delta r/2)^2 (\cos(\theta - \Delta\theta/2) - \cos(\theta + \Delta\theta/2)) + \qquad \text{(A.2a)}$$
$$\frac{\varepsilon_m}{\Delta t}\left[\frac{V^{t+1}_{i+1,j} - V^{t+1}_{i,j}}{\Delta r} - \frac{V^t_{i+1,j} - V^t_{i,j}}{\Delta r}\right](r - \Delta r/2)^2 (\cos(\theta - \Delta\theta/2) - \cos(\theta + \Delta\theta/2)) +$$
$$\frac{\varepsilon_{avg}}{\Delta t}\left[\frac{V^{t+1}_{i,j-1} - V^{t+1}_{i,j}}{\Delta\theta} - \frac{V^t_{i,j-1} - V^t_{i,j}}{\Delta\theta}\right]\Delta r \sin(\theta - \Delta\theta/2) +$$
$$\frac{\varepsilon_{avg}}{\Delta t}\left[\frac{V^{t+1}_{i,j+1} - V^{t+1}_{i,j}}{\Delta\theta} - \frac{V^t_{i,j+1} - V^t_{i,j}}{\Delta\theta}\right]\Delta r \sin(\theta + \Delta\theta/2) = 0$$

$$\varepsilon_{avg} = \varepsilon_o \times (r + dr(i-1)/4.0) \times dr(i-1)/2.0 + \varepsilon_m \times (r + dr(i)/4.0) \times dr(i)/2.0 \qquad \text{(A.2b)}$$

$$\sigma_{avg} = \sigma_o \times (r + dr(i-1)/4.0) \times dr(i-1)/2.0 + \sigma_m \times (r + dr(i)/4.0) \times dr(i)/2.0 \qquad \text{(A.2c)}$$

Here the subscript "o" stands for medium outside the membrane, "m" stands for membrane, and "avg" stands for half medium outside the membrane and half membrane. And for those nodes on j = 0 (on axis) and on the inner side of each membrane, (A.2a) changes to:

$$\begin{aligned}
&\sigma_o \frac{V^t_{i-1,j} - V^t_{i,j}}{dr} * (r + dr/2)^2 (-1 - \cos(\theta + d\theta/2)) + \\
&\sigma_m \frac{V^t_{i+1,j} - V^t_{i,j}}{dr} * (r - dr/2)^2 (-1 - \cos(\theta + d\theta/2)) + \\
&\sigma_{avg} \frac{V^t_{i,j+1} - V^t_{i,j}}{d\theta} dr \sin(\theta + d\theta/2) + \\
&\frac{\varepsilon_o}{\Delta t}\left[\frac{V^{t+1}_{i-1,j} - V^{t+1}_{i,j}}{\Delta r} - \frac{V^t_{i-1,j} - V^t_{i,j}}{\Delta r}\right](r + \Delta r/2)^2 (-1 - \cos(\theta + d\theta/2)) + \\
&\frac{\varepsilon_m}{\Delta t}\left[\frac{V^{t+1}_{i+1,j} - V^{t+1}_{i,j}}{\Delta r} - \frac{V^t_{i+1,j} - V^t_{i,j}}{\Delta r}\right](r - \Delta r/2)^2 (-1 - \cos(\theta + d\theta/2)) + \\
&\frac{\varepsilon_{avg}}{\Delta t}\left[\frac{V^{t+1}_{i,j+1} - V^{t+1}_{i,j}}{\Delta\theta} - \frac{V^t_{i,j+1} - V^t_{i,j}}{\Delta\theta}\right]\Delta r \sin(\theta + \Delta\theta/2) = 0
\end{aligned} \qquad \text{(A.3)}$$

On the inner side of each membrane, (A.1) becomes:

$$\sigma_m \frac{V^t_{i-1,j} - V^t_{i,j}}{dr} * (r + dr/2)^2 (\cos(\theta - d\theta/2) - \cos(\theta + d\theta/2)) +$$
$$\sigma_o \frac{V^t_{i+1,j} - V^t_{i,j}}{dr} * (r - dr/2)^2 (\cos(\theta - d\theta/2) - \cos(\theta + d\theta/2)) +$$
$$\sigma_{avg} \frac{V^t_{i,j-1} - V^t_{i,j}}{d\theta} dr \sin(\theta - d\theta/2) + \sigma_{avg} \frac{V^t_{i,j+1} - V^t_{i,j}}{d\theta} dr \sin(\theta + d\theta/2) +$$
$$\frac{\varepsilon_m}{\Delta t}[\frac{V^{t+1}_{i-1,j} - V^{t+1}_{i,j}}{\Delta r} - \frac{V^t_{i-1,j} - V^t_{i,j}}{\Delta r}](r + \Delta r/2)^2 (\cos(\theta - d\theta/2) - \cos(\theta + d\theta/2)) + \quad \text{(A.4a)}$$
$$\frac{\varepsilon_o}{\Delta t}[\frac{V^{t+1}_{i+1,j} - V^{t+1}_{i,j}}{\Delta r} - \frac{V^t_{i+1,j} - V^t_{i,j}}{\Delta r}](r - \Delta r/2)^2 (\cos(\theta - d\theta/2) - \cos(\theta + d\theta/2)) +$$
$$\frac{\varepsilon_{avg}}{\Delta t}[\frac{V^{t+1}_{i,j-1} - V^{t+1}_{i,j}}{\Delta\theta} - \frac{V^t_{i,j-1} - V^t_{i,j}}{\Delta\theta}]\Delta r \sin(\theta - \Delta\theta/2) +$$
$$\frac{\varepsilon_{avg}}{\Delta t}[\frac{V^{t+1}_{i,j+1} - V^{t+1}_{i,j}}{\Delta\theta} - \frac{V^t_{i,j+1} - V^t_{i,j}}{\Delta\theta}]\Delta r \sin(\theta + \Delta\theta/2) = 0$$

$$\varepsilon_{avg} = \varepsilon_m \times (r + dr(i-1)/4.0) \times dr(i-1)/2.0 + \varepsilon_o \times (r + dr(i)/4.0) \times dr(i)/2.0 \quad \text{(A.4b)}$$

$$\sigma_{avg} = \sigma_m \times (r + dr(i-1)/4.0) \times dr(i-1)/2.0 + \sigma_o \times (r + dr(i)/4.0) \times dr(i)/2.0 \quad \text{(A.4c)}$$

And for those nodes on j = 0 (on axis) and on the inner side of each membrane, (A.2) changes to:

$$\sigma_m \frac{V^t_{i-1,j} - V^t_{i,j}}{dr} * (r + dr/2)^2 (-1 - \cos(\theta + d\theta/2)) +$$
$$\sigma_o \frac{V^t_{i+1,j} - V^t_{i,j}}{dr} * (r - dr/2)^2 (-1 - \cos(\theta + d\theta/2)) +$$
$$\sigma_{avg} \frac{V^t_{i,j+1} - V^t_{i,j}}{d\theta} dr \sin(\theta + d\theta/2) +$$
$$\frac{\varepsilon_m}{\Delta t}[\frac{V^{t+1}_{i-1,j} - V^{t+1}_{i,j}}{\Delta r} - \frac{V^t_{i-1,j} - V^t_{i,j}}{\Delta r}](r + \Delta r/2)^2 (-1 - \cos(\theta + d\theta/2)) + \quad \text{(A.5)}$$
$$\frac{\varepsilon_o}{\Delta t}[\frac{V^{t+1}_{i+1,j} - V^{t+1}_{i,j}}{\Delta r} - \frac{V^t_{i+1,j} - V^t_{i,j}}{\Delta r}](r - \Delta r/2)^2 (-1 - \cos(\theta + d\theta/2)) +$$
$$\frac{\varepsilon_{avg}}{\Delta t}[\frac{V^{t+1}_{i,j+1} - V^{t+1}_{i,j}}{\Delta\theta} - \frac{V^t_{i,j+1} - V^t_{i,j}}{\Delta\theta}]\Delta r \sin(\theta + \Delta\theta/2) = 0$$

If keep the V^{t+1} term on the LHS of all equations and move the other terms to the RHS, the problem can be changed into a typical AX = B problem, where A is a coefficient matrix A = $[A_{PQ}]_{N\times N}$, X = $[V_p^{t+1}]_{n\times 1}$, and B = $[B_p]_{N\times 1}$, p = 1...N, q = 1...N, and p=i×m+j.

VITA

for

Qin Hu

EDUCATION

Ph. D. Electrical Engineering, Old Dominion University, Norfolk, VA
M. S. Electrical Engineering, University of Electronic Science & Technology of China, China
B. S. Electrical Engineering, University of Electronic Science & Technology of China, China

PAPERS PUBLISHED

R. P. Joshi, Q. Hu, and K. H. Schoenbach, "Modeling studies of cell response to ultrashort, high-intensity electric fields – implications for intracellular manipulation," accepted for publication, to appear *IEEE Transactions on Plasma Science*, Aug. 2004.

R. P. Joshi, Q. Hu, K. H. Schoenbach, and S. J. Beebe, "An Energy-Landscape Model Analysis for Irreversibility and It's Pulse Width Dependence in Cells Subjected to a High-Intensity, Ultrashort Electric Pulse", *Physical Review E,* Vol 69,051901,May 2004.

R.P.Joshi, Q. Hu and K.H. Schoenbach, " Dynamical Modeling of Cellular Response to Short-Duration, High-Intensit Electric Fields," *IEEE Transactions On Dielectrics and Electrical Insulation*, Vol. 10, No. 5, pp. 778-787, Oct 2003.

R.P.Joshi, Q. Hu, K.H. Schoenbach and S.J. Beebe, " Simulations of Electroporation Dynamics and Shape Deformations in Biological Cells Subjected to High Voltage Pulses," *IEEE Transactions on Plasma Science*, Vol. 30, No. 4, pp. 1536-1546, Aug 2002.

R. P. Joshi, Q. Hu, K. H. Schoenbach, and H. P. Hjalmarson, " Improved Energy Model for Membrane Electroporation in Biological Cells Subjected to Electrical Pulses," *Phys. Rev. E*, Vol. 65, pp. 041920:01-041920:07, 2002.

R. P. Joshi, Q. Hu, K. H. Schoenbach, and H. P. Hjalmarson, "Theoretical predictions of electromechanical deformation of cells subjected to high voltage for membrane electroporation", *Phys. Review E* , Vol. 65, pp. 021913-1–021913-13, 2002.

R. P. Joshi, Q. Hu, R. Aly, K. H. Schoenbach, and H. P. Hjalmarson, "Self-consistent simulations of electroporation dynamics in biological cells subjected to ultrafast electrical pulses", *Phys. Review E*, Vol. 64, pp. 11913-01–11913-13, 2001.

Q. Hu, "The application of genetic algorithms in Multi-chip Module (MCM) partitioning", *Journal of University of Electronic Science & Technology of China*, no.12, May 1998.

W. Chen, Q. Hu, Z. Zhou, J. Mu, "Optoelectric Multi-chip Module (MCM) and crucial techniques in its physical design", *Hybrid Microelectronics of China*, Vol.9, No.2, 1998.

Q. Hu, W. Chen, F. Meng, "Review of partitioning techniques of Multi-chip Module (MCM)", *Hybrid Microelectronics of China*, Vol.9, No.2, 1998.